# GEOCHEMICAL CHARACTERIZATION AND TECTONIC ENVIRONMENT OF URANIFEROUS BANGANAPALLE QUARTZITE OF KURNOOL GROUP, SARANGAPALLI AREA IN THE NORTHERN MARGIN OF PALNAD SUB-BASIN, GUNTUR DISTRICT, ANDHRA PRADESH

*by*

RACHANA PHULERA
ENGG1G201801008

**Bhabha Atomic Research Centre, Mumbai**

***A thesis submitted to the***
***Board of Studies in Engineering Sciences***

***In partial fulfillment of requirements***
***for the Degree of***
MASTER OF TECHNOLOGY
***of***
**HOMI BHABHA NATIONAL INSTITUTE**

**February, 2021**

# Homi Bhabha National Institute

## Recommendations of the Thesis Examining Committee

As members of the Thesis examining Committee, we recommend that the thesis prepared by **Rachana Phulera** entitled "Geochemical characterization and tectonic environment of uraniferous Banganapalle Quartzite of Kurnool Group, Sarangapalli area in the northern margin of Palnad sub-basin, Guntur district, Andhra Pradesh" be accepted as fulfilling the thesis requirement for the Degree of Master of Technology.

| | Name | Signature |
|---|---|---|
| Member-1 | Dr. D. K. Sinha | |
| Member-2 | Dr. T. S. Sunil Kumar | |
| Member-3 | Dr. Navin Goyal | |
| Member-4 | Dr. Pranesh Sengupta$ | P. Sengupta |
| Member-5 | Dr. A. Rama Raju | |
| Technical advisor | T. P. S. Rawat | |
| Examiner | Prof. M. Srinivas | |
| Guide & Convener | B. S. Bisht | |
| Chairman | Prof. Vivekanand Kain$ | |

**$ Participated through video conferencing**

Final approval and acceptance of this thesis is contingent upon the candidate's submission of the final copies of the thesis to HBNI.

I hereby certify that I have read this thesis prepared under my direction and recommend that it may be accepted as fulfilling the thesis requirement.

**(B. S. Bisht)**
**Guide**

**Date: 11-02-2021**

**Place: Hyderabad**

## DECLARATION

I, hereby declare that the investigation presented in the thesis has been carried out by me. The work is original and has not been submitted earlier as a whole or in part for a degree / diploma at this or any other Institution / University.

RACHANA PHULERA

# ACKNOWLEDGEMENTS

Firstly, I express my sincere gratitude to my Guide Dr. B. S. Bisht, Regional Director, Western Region, Atomic Minerals Directorate for Exploration and Research for his valuable guidance and advice throughout the course of this work. I would also like to extend my thankfulness to my technical adviser Shri T.P.S. Rawat for his continuous support during field work and suggestions pertaining to interpretation of field and laboratory data.

I would like to express my sincere thanks to the Chancellor, Vice-Chancellor and Dean, HBNI and all the competent authorities of HBNI for providing me with the opportunity to pursue the M. Tech. degree. I am also thankful to the Chairman, M. Tech. Monitoring Committee, all its members, external examiner for their suggestions and guidance in completing the thesis.

I am highly indebted to the Director, Atomic Minerals Directorate for Exploration and Research, for kindly providing me permission to pursue the M. Tech. course. I express my gratefulness towards the Additional Director (OP- II) and Regional Director, AMD South Central Region for their constant encouragement and valuable suggestions. I extend my sincere thanks to the Incharge, BARC Training School, AMD Campus, Hyderabad.

I express my gratitude towards Dr. Ramesh Babu, Dr. Neeru Rawal and Mr. Harsha Yalla for their support and inspiration for the M. Tech programme. Also, I would like to thanks all the officers, my colleagues and staff of AMD who have contributed in completion of the present work. I am also grateful to my parents for their continuous support and encouragement.

# CONTENTS

References

# SYNOPSIS

The Sarangapalli area lies in the northern part of Palnad sub-basin and exposes Meso-Neoproterozoic Kurnool group of sediments namely Banganapalle quartzite and Narji limestone non conformably overlain by Paleoproterozoic basement granite. The Banganapalle quartzite exposed as NE-SE trending hillock protruding towards the basin and Narji limestone occurs in low-lying area on the west and east of the quartzite hillock. Drilling in the area has resulted in identification of correlatable unconformity related uranium mineralization over considerable strike length. Geological mapping corroborated with Airborne geophysical data reveals the area is affected by two stage of faulting, 1st stage faulting (NE-SW) brought up Banganapalle quartzite above the Narji limestone which have provided the channel ways for mineralizing solution and 2nd stage faulting (NW-SE) displaces the earlier fault and ore body. Mineralization occurs in the vicinity of NE-SW fault and following its trend. Mineralization is along the unconformity contact and hosted by basement granite and basic dyke (intruded into basement prior to sedimentation) and lower part of Banganapalle quartzite represented by conglomerate, pebbly-gritty quartzite and subfeldspathic arenite. Geochemically, mineralized Banganapalle quartzite is mostly classified as arkose to subarkose while non mineralized quartzites as subarkose to quartz arenite. Provenance studies indicates, these sediments are derived from granite to alkali granite source and deposited in passive margin tectonic settings under semi-arid to semi-humid climatic conditions. The basement granite showing signature of S-type granite, is fertile in nature and had acted as source for uranium mineralization. Unconformity has provided physico-chemical gradient for mineralizing solution. Sericitization and chloritization are dominant alteration features present mainly near the unconformity surface and transgressing the lithological boundary signifies hydrothermal activity.

Uraninite and coffinite are the dominant uranium phases present and are closely associated with chlorite and pyrite. Chloritization took place at $245^0$C temperature. Chlorite along with some pyrite aided uranium precipitation by reducing it from solution. On the basis of textural relationship mineral paragenetic sequence has been established. Mineralization took place during syn- to post- chloritization.

# LIST OF FIGURES

# LIST OF TABLES

# CHAPTER 1

# INTRODUCTION

Uranium deposits are usually classified based on the characteristics of their host rocks and geological environments (Dahlkamp, 1993; OECD/NEA Red Book and IAEA, 2000; Cuney, 2009). The traditional unconformity-related uranium deposits are the most economical one in the world, with the highest grade amongst all deposit. The intra-cratonic, Paleo- to Neoproterozoic Cuddapah basin having a spread of over 44,500 sq. km, is the second largest Proterozoic basin in India, hosts several types of uranium deposits in its various stratigraphic levels. Uranium mineralization is recorded in the Gulcheru and Vempalle formations, in the lower part and along the unconformity between the basement granite and the overlying sediments of Srisailam and Banganapalle formations, in the upper part of the Cuddapah sequence. The Srisailam and Palnad sub-basins lying in the northern part of Cuddapah Basin hosts Proterozoic unconformity related uranium mineralization (Dwivedy, 1995; Jeyagopal et al., 1996; Sinha et al., 1996; Banerjee, 2005; Umamaheswar et al., 2009). Uranium mineralization in these sub-basins occurs close to the unconformity between the basement granitoids, and overlying arenaceous sediments of Meso-Neoproterozoic age. The basement rocks are mainly represented by grey, coarse grained biotite granites, which are highly epidotised and chloritised at places. These are profusely traversed by dolerite dykes exhibiting NNW-SSE, NW-SE, E-W and NNE-SSW trends they have possibly played vital role in increasing thermal gradient and release uranyl ions into the solutions with remobilisation along fractures (Bisht et. al 2001, Thomas et al., 2014). Concerted sub-surface exploration over more than two decades has established three uranium deposits at Lambapur, Peddagattu and Chitrial along the unconformity between the basement Mahbubnagar granite and overlying Srisailam Formation in Srisailam sub-basin; and one low tonnage deposit at Koppunuru close to the unconformity contact between basement granite and Banganapalle Formation of the Kurnool Group in the Palnad sub-basin (Ramesh Babu et al., 2012).

In all these deposits, uranium mineralization is concealed and lies below the cover rocks at a depth of < 5-150m. Uranium mineralization located in these sub-basins show dissimilarity with that of unconformity-type uranium deposits in Canada and Australia, especially in respect of basement and marked absence of paleosol. Due to proximity of mineralization near the unconformity, these deposits are named as unconformity related / proximal uranium mineralization. The northern part of Palnad sub-basin, is one of such targets in Eastern Dharwar Craton where lithostratigraphic and structural setup is highly favorable for unconformity-related uranium mineralization.

The study area i.e. Sarangapalli (toposheet no- 56 P/14, 56 P/10) lies in the northern part of Palnad sub-basin, Guntur district, Andhra Pradesh and is situated~ 63 km NE of Koppunuru uranium deposit. Here the basement granitoids are non-conformably overlain by Neoproterozoic Kurnool sediments comprising Banganapalle Quartzite and Narji Limestone. Banganapalle quartzite occurs as hillocks protruding towards the basin and Narji Limestone in the low-lying area. The NE-SW trending fault traversing the basement granitoid and overlying sediments brought up Banganapalle Quartzite to the surface. Sub-surface exploration for uranium is being carried out in this area since 2018 which has resulted in identification of correlatable unconformity related uranium mineralization over considerable plan area. The uranium mineralization is hosted by basement granite and Banganapalle Quartzite and extends a few meters above and below the unconformity.

The need has been felt to establish certain guides as a tool to understand behavior of uranium mineralization, through the study of mineralized and non-mineralized core samples available through ongoing sub-surface exploration so that these guides can be used in further exploration in the area.

## 1.1 PREVIOUS WORK

The Sarangapalli area was taken up for subsurface exploration during field season 2017-18 by the Atomic Minerals Directorate for Exploration and Research (AMD), after regional hydro-geochemical survey was carried out in the area during F.S. 1997-98 indicated presence of significant hydro-uranium anomaly (U = 7 to 45 ppb, n=5). Reconnaitory core drilling was taken up in Sarangapalli area to explore the unconformity proximal U-mineralization in the vicinity of two NE-SW trending major faults and close to hydro-uranium anomaly which has been resulted in identification of U-mineralization correlatable over considerable area. Presently, drilling is being carried out to establish dip and strike continuity of the U-mineralisation.

The U-mineralization in the Sarangapalli area is associated with Banganapalle Quartzite and basement granite proximal to the unconformity, transgressing partly to the sediments and partly in granite. Petro-mineralogical study of the radioactive granite reveals presence of uraninite, coffinite & coffinitised uraninite often as an association with pyrite.

## 1.2 PRESENT WORK

### 1.2.1 Principal Objective

- To map the litho-structures of the study area for understanding their control on uranium mineralization.
- To understand the geochemical controls of mineralization, study of alteration pattern and elemental behavior in mineralized and non-mineralized parts of Banganapalle Quartzite.
- Understanding of paragenetic sequence of radioactive and non-radioactive phases of Banganapalle Quartzite.
- To integrate these studies with available airborne geophysical data (VTEM).
- To develop genetic model for uranium mineralisation in Banganapalle Quartzite.

### 1.2.2 Research plan / Methodology

- Detailed litho-structural mapping (5 sq. km) on scale 1:5, 000.
- Systematic collection of samples of Banganapalle Quartzite from borehole cores and surface.
- Petro-mineralogical studies by optical microscope, XRD and EPMA.
- Geochemical analysis by XRF and chemistry lab.
- Study and interpretation of borehole data for generation of isograd and isopach map.

### 1.2.3 Deliverables

- Detailed litho-structural map of Sarangapalli-Madinapadu area over 10 sq. km at scale 1:5,000.
- Corroborate study with geophysical data.
- Interpretation of geochemical data by various geochemical plots.
- Generation of paragenetic sequence.

## 1.3 LOCATION AND ACCESSIBILITY

Sarangapalli area (16º 39’ 59.76” N, 79°46’54.12” E) is situated in Guntur district, Andhra Pradesh. The area falls in Survey of India Topographic Sheet No.56P/14 and 56P/10. An area lying in the west of Sarangapalli village is taken up for the present study. The study area is well connected by roads and is about 194 km SE of Hyderabad (Figure 1.1), can be approached by many routes among them. The Hyderabad-Nalgonda-Miryalaguda -Sarangapalli is the shortest route (Figure 1.1). Nearest railway station is Nadikudi junction, which is situated about 13 km SSW of the study area.

## 1.4 CLIMATE

The area has tropical climate. Inland areas warm up greatly during the afternoon and cool down quickly at night. January, February and March months are usually pleasant with moderate winds from South-East. In winter, there is much less rainfall than in summer. The average annual temperature is 28.5 °C | 83.3 °F in Guntur. Annual rainfall is 906 mm | 35.7 inches. The least amount of rainfall occurs in January with an average of 1 mm. Most precipitation falls in July, with an average of 171 mm | 6.7 inch. The average temperature is highest in May, at around 33.6 °C | 92.5 °F. In December, the average temperature is 24.1 °C | 75.4 °F which is the lowest average temperature recorded in a year (https: //en.climate-data.org, 2018).

Figureure 1.1 Location map of Sarangapalli area, Guntur district, Hyderabad

## 1.5 GEOMORPHOLOGY, DRAINAGE AND VEGETATION

Regionally, two distinct physiographic units, viz. limestone plains and a hill range (Banganapalle Quartzite) are recognized. The study area is partly soil covered with few linear outcrops and isolated hillock. Krishna is the only river draining through the northern part of the study area. The Krishna river' s source is at Mahabaleshwar near the Jor village in the extreme north of Wai Taluka, Satara district, Maharashtra. A part of study area is covered with sparse vegetation and cultivated lands.

# CHAPTER 2

# GEOLOGY OF THE AREA

## 2.1 REGIONAL GEOLOGY

The Crescent shaped Proterozoic Cuddapah basin, situated at the southeastern part of the East Dharwar craton, India, lies close to the western margin of the Eastern Ghats Mobile Belt (EGMB). This margin has been considered as a Proterozoic collisional boundary by several workers (Chetty and Murthy, 1994; Vijaya Kumar and Leelanandam, 2008). It has a concave eastern margin 440 km long, with a maximal basinal width of 145 km in the middle, covering an area of 44,500 km$^2$ and containing over 12 km of sediments and volcanics overlying the Archaean granite-greenstone terrain. The lithostratigraphy of Cuddapah basin is formalised in terms of Cuddapah Supergroup and Kurnool Group (Nagaraja Rao et al., 1987). The Cuddapah Supergroup is predominantly arenaceous to argillaceous with subordinate calcareous to dolomitic units, whereas the Kurnool Group mainly consists of carbonate facies sediments with subordinate fine clastics. Kurnool Group is developed in the Kurnool and Palnad Sub-basins. The Cuddapah Supergroup is developed in Papaghni, Chitravati and Srisailam Sub-basins and the Nallamalai belt in the east. Apart from the resources that it hosts, the CB carries a wealth of structural and tectonic information, which holds the key for understanding the physical processes that seem to have operated in the lower crust and upper mantle. The structures in the basement as well as the cover sediments manifest the different stages of evolution of the Cuddapah Basin through time. The western margin of CB, is marked by extensive and intrusive mafic volcanic rocks (1900Ma, 40Ar-Ar39, Anand et al., 2003) in the form of sills and flows, is free from the major folding history; while the Nallamalai Belt, in the eastern margin of Cuddapah basin is occupied by the development of low amplitude folds in the western parts, gradually transforming into tight isoclinal folds towards the east, which has resulted from easterly compression and thrusting related to the Eastern Ghat orogeny

(Nagaraja Rao et al., 1987). The Nallamalai fold belt (NFB), approximately N-S trending, 80-100 km wide, 400 km long arcuate, has thrusted contact with Nellore schist belt (NSB) in the east (Ramam and Murty, 1997; Saha, 2002; Saha, 2004). The western boundary of NFB with generally flat lying Kurnool Group of rocks, earlier referred to as "Rudravaram line" (Meijerink et al. 1984), has been reinterpreted as a major thrust known as Mydukur thrust (Chakraborti and Saha,2009).

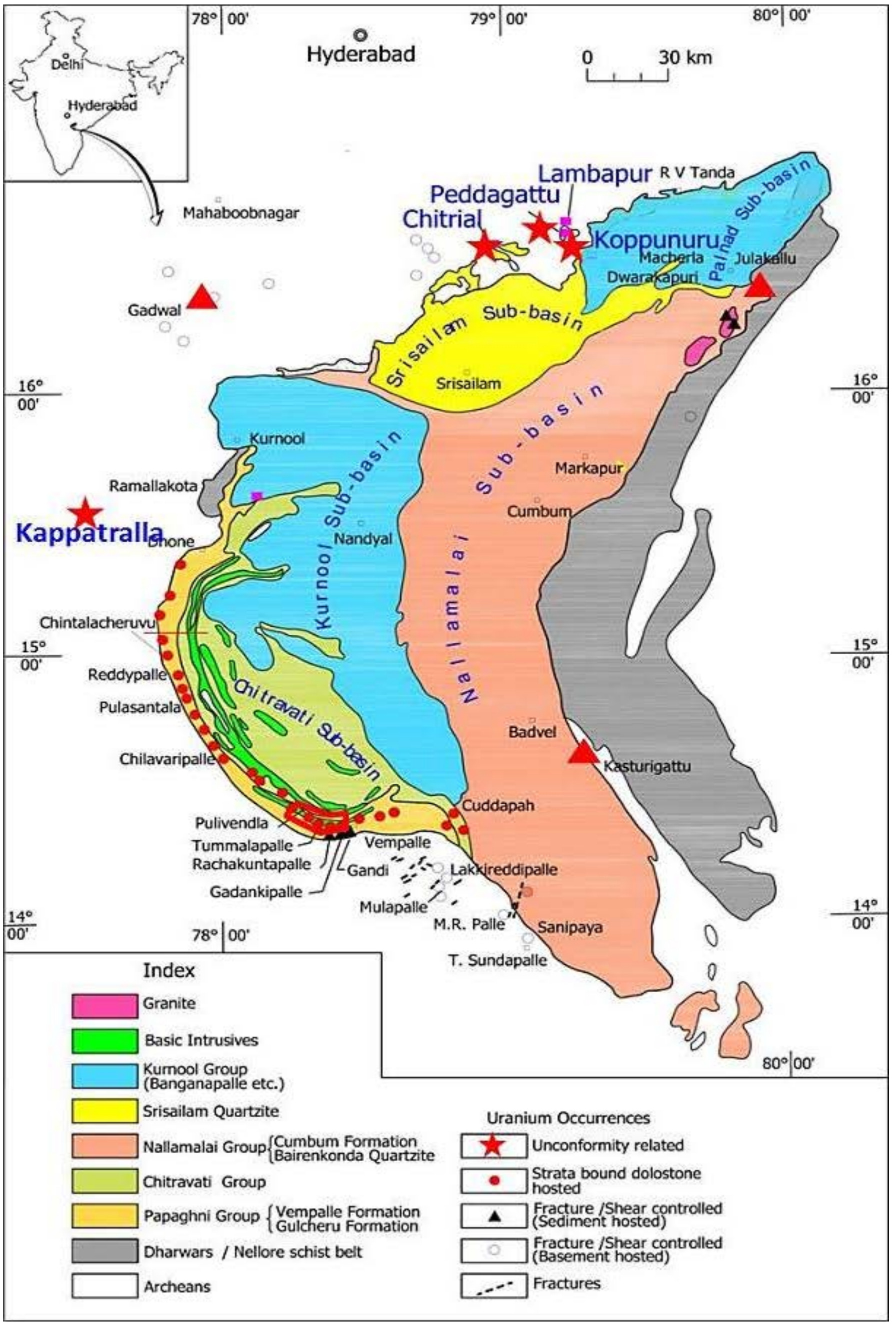

Figure: 2.1 Geological map of Cuddapah basin showing uranium deposits and occurrences (after Nagaraja Rao et al., 1987)

### 2.1.1 STRAITIGRAPHY OF CUDDAPAH BASIN

Table 2.1 Stratigraphy of Cuddapah Basin (Nagaraja Rao et al., 1987)

| Super Group/ Group /Sub Group | | Formation | Thickness in m |
|---|---|---|---|
| Kurnool Group | Kundair Sub-Group | Nandyal Shale | 50 - 100 |
| | | Koilkuntla Limestone | 15 - 50 |
| | | Paniam Quartzite | 10 - 35 |
| | ~~~~~Para conformity~~~~~~~~~~ | | |
| | Jammalamadgu Sub-Group | Owk Shale | 10 - 15 |
| | | Narji Limestone | 50 - 100 |
| | | Banganapalle quartzite | 10 - 50 |
| | ~~~~~~~~ Unconformity~~~~~~~~~~ | | |
| Cuddapah Supergroup | Srisaliam | Srisaliam Quartzite | 300 |
| | ~~~~~~~~ Unconformity~~~~~~~~~~~ | | |
| | Nallamalai Group | Cumbum Formation | 2000 |
| | | Bairenkonda Quartzite | 1500 - 4000 |
| | ~~~~~~Angular Unconformity~~~~~~~~ | | |
| | Chitravati Group | Gandikota Quartzite | 300 |
| | | Tadpatri Shale | 4600 |
| | | Pulivendla Quartzite | 1 – 75 |
| | ~~~~~~~~ Disconformity~~~~~~~~~~ | | |
| | Papaghni Group | Vempalle Limestone | 1900 |
| | | Gulcheru Quartzite | 28 - 210 |
| | ~~~~~~~~ Nonconformity~~~~~~~~~~~ | | |
| Archaean and Dharwars | Intrusive grey medium grained chloritized biotite granite, gneisses/ greenstones | | |

**Papaghani Group**

The Papaghni Group consists of two formation rank units: the siliciclastic-dominant Gulcheru Quartzite; and the mixed siliciclastic–carbonate-bearing Vempalle Formation. The latter has many mafic flows, sills and dykes in the upper part of the formation (Saha and Tripathy, 2012).

### (i) Gulcheru Quartzite

The Gulcheru Quartzite consists mainly of polymictic conglomerate/grit, arkose and quartzite with shale intercalations. In the northern half of the belt the lower sequence is represented by conglomerate and arkose but in the southern half it is represented only by quartzite alone.

### (ii) Vempalle Formation.

The facies of Gulcheru Formation grades upwards to a mixed siliciclastic–carbonate unit with silicified stromatolitic limestone–dolomite beds, calcareous cross-bedded to rippled sandstone and laminated grey-green–brown shale of Vempalle formation.

## Chitravati Group

The Chitravati Group consists of three formation rank units: Pulivendla Quartzite; Tadpatri Shale; and the Gandikota Quartzite. The transition from the Papaghni Group to the Chitravati Group is marked by the intermittent occurrence of mafic flows and associated shallow-crustal intrusives in the form of sills and dykes in the underlying Vempalle Formation (Saha and Tripathy, 2012).

### (i) Pulivendla Quartzite

Compared to the Gulcheru Quartzite, the Pulivendla Quartzite has more restricted strike continuity across the Papaghni sub-basin. The formation consists of medium- to thick bedded well-sorted quartz arenite with sparse pebble beds in the basal part. The lower part of the formation NW of Yagantipalli consists of large (1– 2 m across) trough cross-bedded, medium-grained well-sorted sandstone (quartzite) with rare lag pebbles.

### (ii) Tadpatri Shale

The Pulivendla Quartzite grades upwards into shale–fine calcareous sandstone unit with 30–40 cm-thick dolomitic limestone interbeds. Basic flows and sills are also present in the Tadpatri Formation. The sandy units contain symmetric to asymmetric ripples.

### (iii) Gandikota Quartzite

In the east-central part of the Papaghni sub-basin, the Tadpatri Formation is conformably overlain by another formation rank unit, the Gandikota Quartzite. The contact is gradational with thinly bedded sand–shale intercalations in the transitional zone giving way to amalgamated quartzite beds with sheet geometry. The bulk of the formation consists of well-rounded well-sorted medium- to coarse-grained quartz arenite with large (up to 0.7 m) planar tabular to large trough cross-stratification.

## Nallamalai Group

The Nallamalai Group is divided into Bairenkonda Formation and Cumbum Formation with a cumulative thickness of 1200 m (Saha and Tripathy, 2012) as estimated from an exposed section of the Vellikonda range east of Porumamilla whereas according to Nagaraja Rao et al., (1987) ~ 6000 m thickness of Nallamalai Group of sediments were estimated. The quartzite-dominant part with minor quartz phyllites (protoliths of micaceous sandstone and shale) in the lower part is regarded as the Bairenkonda Subgroup, and the upper phyllitic and quartzite intercalation is regarded as the Cumbum Subgroup (Meijerink et al.,1984).

### (i) Bairenkonda Formation

Bairenkonda Formation is dominantly an arenaceous unit and in most of the area it is represented by quartzite alone (Nagaraja Rao et al., 1987). Bairenkonda Quartzite shows coarse to pebbly trough cross-stratified and rippled sandstone overlain by a hummocky cross-stratified sandstone/siltstone. Straight crested ripples are common in coarse- to medium-grained sandstones with desiccation cracks. This grades into plane-laminated shale interstratified with glauconitic sandstone.

### (ii) Cumbum Formation

The Cumbum Formation is basically an argillaceous unit with intercalations of quartzite and dolomite at various levels. The argillaceous unit is identified as shale, slaty shale, slate and at places phyllite (Nagaraja Rao el al., 1987).

### Srisailam Quartzite

The Srisailam Quartzite unconformably overlies the granite gneiss basement along its western contact and is in thrust contact with the Nallamalai Group along its southern boundary. It is composed mostly of well sorted, medium-grained, purple subarkose to quartz arenite, ferruginous and glauconitic in places. Individual beds range in thickness from 5cm to 50cm, but often amalgamate to 4m-thick units. Successive beds are separated by siltstone and mudstone unit with beds ranging in thickness from 3 to 5cm (Patranabis-Deb et al., 2012).

### Kurnool Group

As mentioned earlier, the Kurnool Group of sediments are deposited over Kurnool and Palnad sub-basin. The Kurnool Group consists of >500 m (Patranabis-Deb et al., 2012) of undeformed mixed siliciclastics and carbonates that pass from the basal detrital diamond-bearing Banganapalle Formation (conglomerates and coarse arenites), through micritic carbonates of the Narji Limestone Formation, the Owk Shale Formation, the Panium Formation (quartz arenites), the Koilkuntala Formation (limestones) to the uppermost Nandyal Shale Formation.

### (i) Banganapalle Quartzite

Basal most unit of Banganapalle Quartzite is conglomerates which occur as laterally impersistent sheets and grades up to coarse-grained pebbly sandstone. The clasts are from 2cm to 25cm in size, subangular to subrounded and are mostly of red, green, or buff jasper, chert, dolomite, vein quartz, quartzite, phyllite and granite (Patranabis-Deb et al., 2012). Conglomerate beds are massive, normally or reverse graded or are internally crudely planar parallel stratified. Barytes is also noticed as pebbles in the conglomerate (Nagaraja Rao et al., 1987). It grades up to multistorey bodies of trough cross-stratified coarse-grained feldspathic sandstone with sheet-like geometry. The cross-strata in these sandstones exhibit very uniform unidirectional flow towards S-SW in the Kurnool sub-basin and S-SE in the Palnad sub-basin and several bedding surfaces are mantled by single grain-thick layers of small pebbles, or thin mud laminae. It passes up to medium-grained pebbly quartzose sandstone with pinch-and-swell geometry. The sandstone beds are 50 to 80cm thick, and wavy to planar laminated, or trough- and planar cross-stratified, often with asymptotic foresets. It passes up to fairly well sorted, medium-grained, subarkosic to quartzose sandstone forming small lenticular shoaling-up bodies with bimodal–bidirectional palaeocurrents (Patranabis-Deb et al., 2012).

### (ii) Narji Limestone

The Narji Limestone gradationally overlies the Banganapalle Quartzite. The limestones are mostly micritic, grey and black often with profuse chert nodules. Beds are 5 to 50cm thick, planar tabular to slightly wavy type. Bed sets are laterally very persistent, and could be traced about 50m laterally. The grey limestone dominates the lower part of the Narji succession and commonly contains intercalated sandstone as discrete beds or as mixed siliciclastic carbonate beds. The interval also contains small pockets or thin sheets of intraformational lime–clast conglomerates. The grey limestone passes up to black limestone forming laterally extensive sheet. Pyrite occurs profusely in this unit. The Narji limestone has a thickness ranging from 50 m to 100 m and accounts for one third of the total thickness of the Kurnool Group (Nagaraja Rao et al., 1987). The black limestone grades upward to the ochre yellow coloured Owk Shale which marks the end of the platform development.

### (iii) Owk shale

Owk shale in most of the cases is ocharous and characterised by the presence of yellow and white ochre. This is well laminated thin bedded unit consisting of silty claystone with thin beds of fine-grained quartzite (Richards et al, 1968). Thickness range from few meters to 35 m.

### (iv) Paniam Quartzite

Paniam Quartzite is essentially quartz arenite, but (Dutt,1962) recorded siliceous shale in the upper part and identified thin conglomerate and grit beds at the base. The upper horizon of the Paniam quartzite exhibits typical pinnacle nature, a feature which distinguish the Paniam Quartzite from the rest of the quartzite of the Kurnool Group.

### (v) Koilkuntla Limestone

This is basically a calcareous unit, but is more siliceous and argillaceous when compared with Narji Limestone of Kurnool Group. The limestone is light grey to dark grey in color and flaggy with occasional massive bands. The limestone in the lower horizon has flaggy quartzite intercalations.

### (vi) Nandyal Shale

This unit, though basically argillaceous, has calcareous intercalations and shows lower shaly and calcareous flaggy unit and an upper shaly limestone. The shaly flag is a purple calcareous shale which is soft and weathers into pencil like fragments. The shaly limestone is dark grey and greenish grey and breaks with sharp edges.

### 2.1.2 STRUCTURAL FRAMEWORK OF CUDDAPAH BASIN

Cuddapah basin has an undeformed western half, and a deformed eastern half called the Nallamalai fold belt. NFB is a north-south trending arcuate belt of intense folding, faulting and thrusting in the eastern half of the Proterozoic Cuddapah basin (Narayanaswami, 1966; Meijerink et al., 1984; Nagaraja Rao et al., 1987; Venkatakrishnan and Dotiwalla, 1987). Two major intracontinental thrusts, Velikonda and Rudravaram line limits the eastern and western boundary of NFB respectively (Saha, 1994; Saha et al., 2010). The Rudravaram line suggests westward tectonic transport of the Nallamalai rocks and presence of a major thrust (Maidukuru thrust) between the Paleo-Mesoproterozoic Nallamalai rocks and the Meso-Neoproterozoic Kurnool group of rocks. The eastern boundary thrust, the Vellikonda thrust front, separates the Nellore Schist Belt with supposed Archaean greenstone belt remnants and Palaeoproterozoic ophiolites (Narayanswami 1966; Meijerink et al. 1984; Nagaraja Rao et al., 1987; Ramam & Murty 1997; Saha 2002, 2004; Ravikant 2010; Saha et al., 2010). Within NFB rocks of the Nallamalai Group have been folded into a series of doubly plunging anticlines/synclines interspersed by oblique and cross faults (Nagaraja Rao et al., 1987). The intensity of folding increases from west to east in the Nallamalai fold belt with low amplitude open folds progressively becoming tight isoclinal folds (Nagaraja Rao et al., 1987). Within the Nallamalai sub-basin five distinct tectonic zones were identified and their mutual boundaries were interpreted to be defined by deep faults or thrusts (Meijerink et al., 1984) proceeding from west to east, an increasing complexity and intensity of folding observed, as well as increase of metamorphism. On the basis of the structural geometry of the rocks Matin and Guha (1996) identified two phases of deformation in the extreme southern part of the NFB. However, Mukherjee (2001) opined that mutual relationships of structural elements in a part of the southern NFB indicated a combination of bulk inhomogeneous shortening across the belt and top-to-west variable simple shear under a progressive contractional deformation. From the occurrence of small-scale refolded folds, deformed lineations and overprinting of foliation three phases of deformation were suggested in the northern part of the NFB (Saha, 2002). Venkatakrishnan and Dotiwalla (1987) put forward a kinematic model wherein the arcuate geometry of the NFB was interpreted as the result of differential buttressing of the advancing west-verging thrust sheets, its transpression and refolding. According to several researchers deformation in the NFB took place in several episodes with overall E-W shortening in association with westerly thrust transport (Meijerink et al., 1984; Saha, 2002, Saha et al., 2010). Harmonic folds to the east of the Rudravaram line gradually pass into disharmonic folds, isoclinal folds, thrusts and imbricate thrusts towards east (Meijerink et al., 1984; Nagaraja Rao et al., 1987). The axial trend of the folds varies from NW-the fault trending ENE-WSW and called KarkaI Dbadi fault marks the boundary of Cuddapah rocks in the southern part of the basin.

### 2.1.3 MAJOR STRUCTURES

**Ramallakota-Gani-Kalva Fault**

This fault trends ENE-WSW and crosses the limits of Cuddapah basin after affecting both the Cuddapah and Kurnool formations. This is a wrench fault having differential throws at different places and has caused a steep monocline called as 'Kalva wall'. Coulson (1933) who interpreted it as a basement-rooted fault, which was reactivated in post-Kurnoo1 times. A similar wrench southern part to N-S in the middle to NE-SW in the northern part of the NFB (Nagaraja Rao et al., 1987; Matin and Guha, 1996).

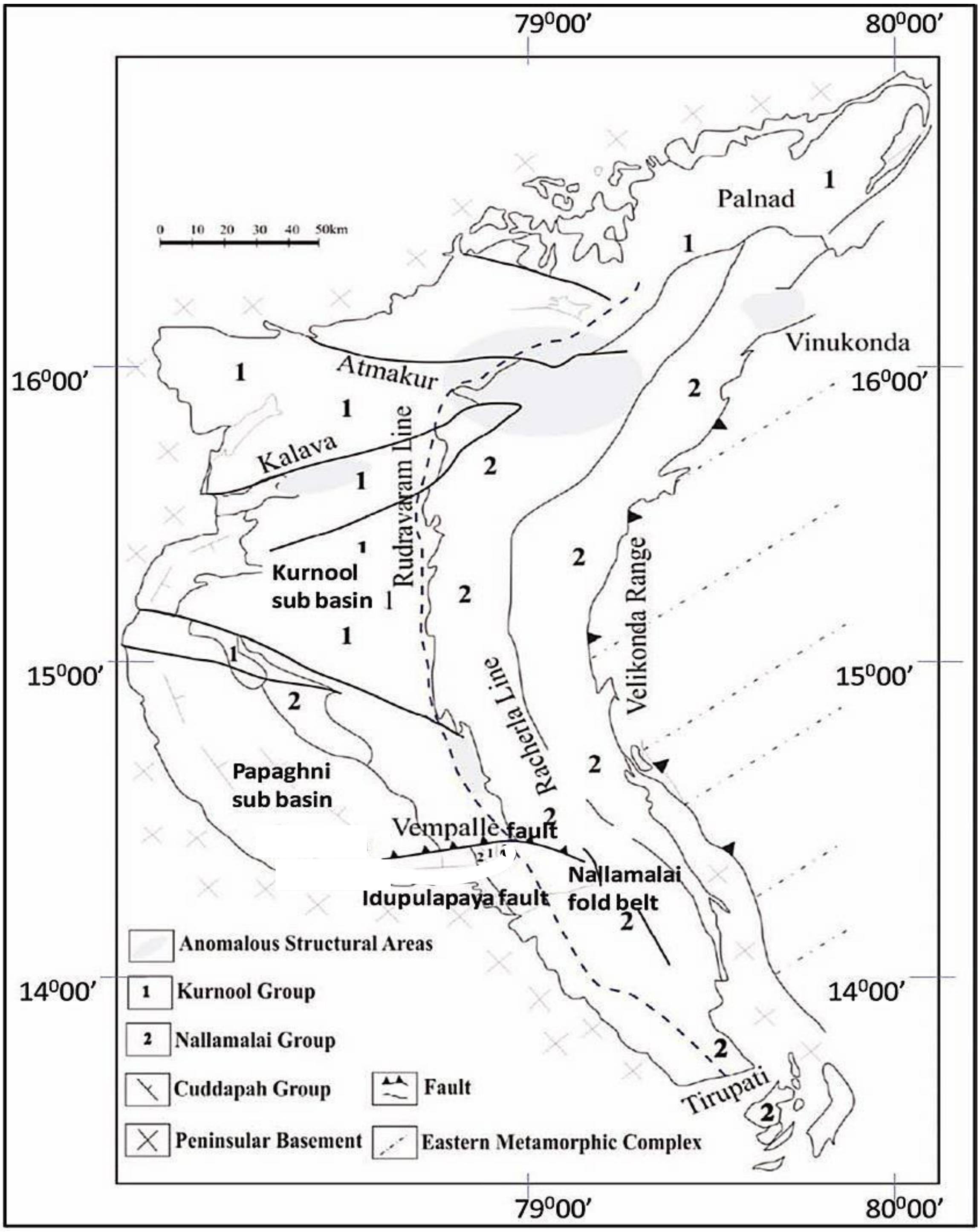

Figure. 2.2 Tectonic map of Cuddapah Basin showing regional structures (after, Meijerink et al., 1984).

### Atmakur-Kolhapur faults

The northern boundary of the Nandyal depression is affected by a set of E-W trending normal faults of varying throw and age.

### Iswarakuppam Dome

This is major domal structure exhibiting quaversal dips in the basin. It is constituted of core quartzite followed by the alternating sequence of quartzite and shale/phyllite.

### Structures around Racherla

A series of doubly plunging anticlines west of Racherla run obliquely through the Cumbum synclinorium. Some long trending tectonic lines are interrupted by the anticlines. The northernmost anticline, on the axial continuation of the eastern domal anticline, is cut off by the Racherla fault, which develops from the base of the long hogback near Cumbum town. Vertical and sinistral strike slip movements have taken place along the Racherla fault, which can be continued much farther to the south.

### Nallamalai Fold Belt (NFB)

NFB is an arcute belt of intense folding, faulting and thrusting in the eastern half of the Proterozoic Cuddapah Basin. Within this belt rocks of the Nallamalai Group have been folded into a series of doubly plunging anticlines/synclines interspersed by oblique and cross faults (Nagaraja Rao et al., 1987). Folding increases in intensity from west to east in the Nallamalai fold belt with low amplitude open folds progressively becoming tight isoclinal folds.

### Vellikonda Thrust

Cuddapah basin Eastern Boundary is known as Vellikonda thrust, runs for a length of about 480 km between Cuddapah basin and Nellore schist belt. The Vellikonda thrust is characterized by mylonitization in both its hangingwall (NSB) and footwall (Bairenkonda quartzite). The deformation is mainly characterized by feldspar grains possesses intragranular fractures. Such fractures take place when the thrust sheet emplaced at shallow crustal level at temperature 300°C (Passchier and Trouw, 2005).

**Post Kurnool deformation**

In the Palnad area, the Cumbum Formation rests over the Narji Limestone with a thrust contact which has to be post- Kurnool. Similarly, the Nallamalai Group on the western side in the Mydukuru-Khajipet area is thrust over Koilkuntla Limestone of Kurnool Group (Nagaraja Rao et al., 1987).

### 2.1.4 IGNEOUS ACTIVITY

Major igneous suites associated with Vempalle and Tadpatri Formations in the western part of the basin are dolerite, picrite and gabbro sills, basaltic flows, ignimbrite and ashfall tuffs. Kimberlite dykes and syenite stocks are found in the Cumbum rocks of Chelima-Giddaluru area. Large exposures of granite/ gneissic rocks within the domal structures within the Cumbum Formation are variously interpreted as instrusives into the sedimentary pile or reactivated portions of the basement gneisses (Nagaraja Rao et al., 1987).

## 2.2 LOCAL GEOLOGY

The Kurnool Group of sediments belongs to Meso- to Neoproteroic era (Kumar et al. 1993, 2001; Chalapathi Rao et al. 1996, 1999, 2013; Kumar, Heaman et al., 2007; Babu et al. 2008). The Palnad sub-basin (~3400 sq. km), located at the northeastern part of the intracratonic Cuddapah basin exposes Kurnool group of rocks, has faulted southern and eastern contact with the Nallamalai metasediments. Its western contact with the Srisailam sub-basin is either marked by fault or is separated by basement highs (granite inlier). The study area, Sarangapalli is located in the northern part of Palnad sub-basin where basement granitoids are unconformably overlain by Kurnool sediments comprising Banganapalle

Quartzite and Narji limestone. The area is partly soil covered with outcrops of Narji and Banganapalle formations.

Banganapalle Quartzite occurs as hillocks protruding towards the basin and Narji limestone in the low-lying area. The NE-SW trending faults traversed from basement to the sediments brought up the Banganapalle sediments to the surface.

The Banganapalle Formation is the oldest lithounit of Palnad sub-basin, represented by 10-100m thick quartz arenite and intercalated grey shale sequence with basal conglomerate. This is overlain by 10-70 m thick sequence of massive limestone with silicic stylolite and flaggy calcareous shale belonging to Narji Formation. The thickness of the Kurnool sediments in this part is recorded up to 200m. The basement granite is not exposed at the surface of the study area.

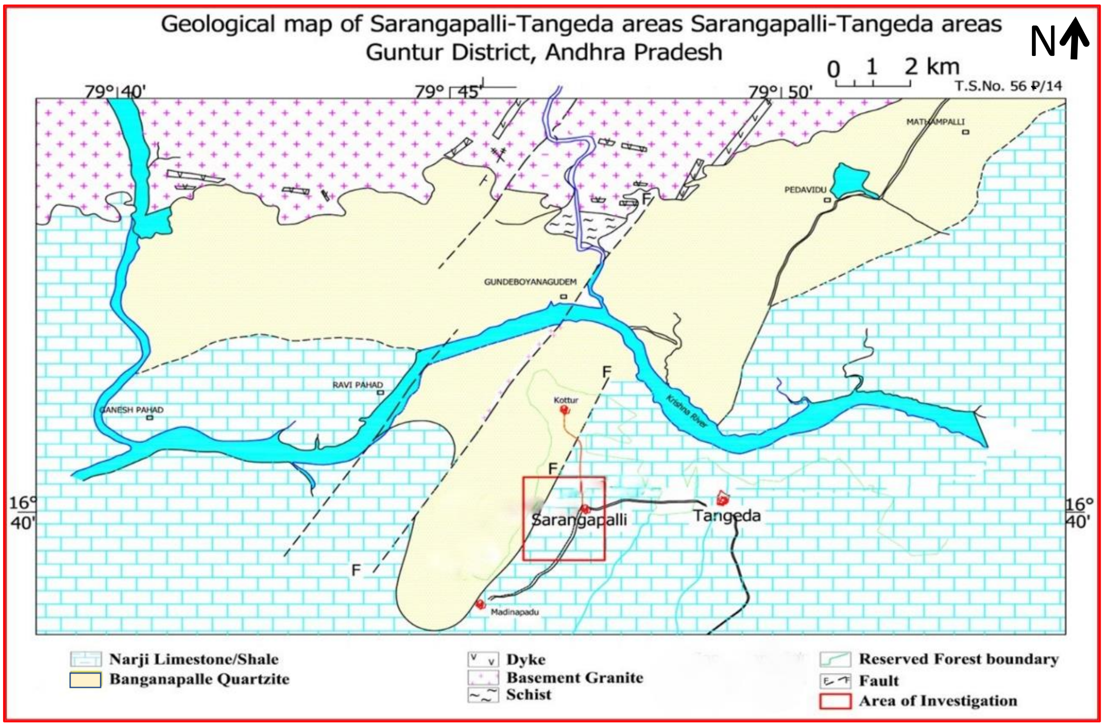

Figure. 2.3 Geological map of Sarangapalli-Madinapadu area (Modified after GSI)

# CHAPTER 3

# INTEGRATED FIELD STUDIES

Detailed geological mapping carried out over 10 sq. km area in Sarangapalli-Madinapadu (on 1:5000 scale). Preparations for the planning of mapping have been done such as consultations of old literature on different aspects like physiography, drainage pattern, accessibility, geology of the area as well as of adjacent areas or areas having similar geological set up, collection and study of toposheets (56P/10 and 57P/14) and Satellite images of the area to get acquainted with approach, accessibility, surface features of the area etc.

## 3.1 REMOTE SENSING STUDIES:

To understand the major geological and structural pattern of the study area, Remote Sensing study has been carried out prior to ground geological studies.

Lineaments are defined as mappable linear features of the earth's surface which differ distinctly from the patterns of adjacent features and presumably reflect subsurface phenomena. The work includes preparation of lineaments map by visual image interpretation (manually extracted); this has been shown possible relationships between lineaments and known geologic structures in the study area (fractures/ fault). From the literature, it can be concluded that lineaments usually occur as edges with tonal differences in satellite images.

In order to extract / interpret lineaments of Sarangapalli area, Guntur dist. A.P., satellite image (Landsat 7 ETM+) has been acquired from USGS website. After acquisition, image processing and image enhancement carried out using ARCGIS software. To increase spectral resolution of the image, composite image of band 1-7 (excluded thermal band 6) with 30m spectral resolution merged with panchromatic band 8 with 15m spectral resolution.

Panchromatic sharpen image further applied to radiometric, spatial and spectral correction to enhance the image quality.

For lineament extraction, principal component analysis (PCA) technique was used. PCA is an image transformation technique based on the processing of multi-band data sets that can be used to reduce the dimensionality in the data, and compress as much of the information in the original bands into fewer bands. PCA is applied to 6 bands (band 1,2,3,4,5,7) to compress the information in few bands. Table 3.1 illustrates the image statistics of the principal components (PCs) performed using ETM bands (1-5 and 7) as input channels.

**Table:3.1 Percent and cumulative eigen values, Principal component analysis**

| #PC | Eigen Value | Percent of Eigen Values | Accumulative of Eigen Values |
|---|---|---|---|
| 1 | 8942.85 | 94.31 | 94.30 |
| 2 | 339.72 | 3.58 | 97.89 |
| 3 | 176.27 | 1.86 | 99.74 |
| 4 | 14.34 | 0.15 | 99.90 |
| 5 | 7.00 | 0.07 | 99.97 |
| 6 | 2.45 | 0.03 | 100.00 |

The eigen values indicate the decreasing variance in successive principal components. The first principal component contains 94.31 % of the total variance. It means the maximum information lies in the PC1 (Figure3.1). The first three component contain 99.75% of the total variance. Lineaments were extracted manually using the principal component image shown in (Figure3.3).

**Interpretation of Remote Sensing Studies**

Geologically the area comprises Banganapalle quartzite ridge surrounded by Narji limestone. The Banganapalle quartzite is bounded by NE-SW trending faults to the East and west, due to which it stands above the Narji limestone. Major lineament trend extracted from satellite image are NE-SW and NW-SE which can clearly be correlated with faults and fractures in the area

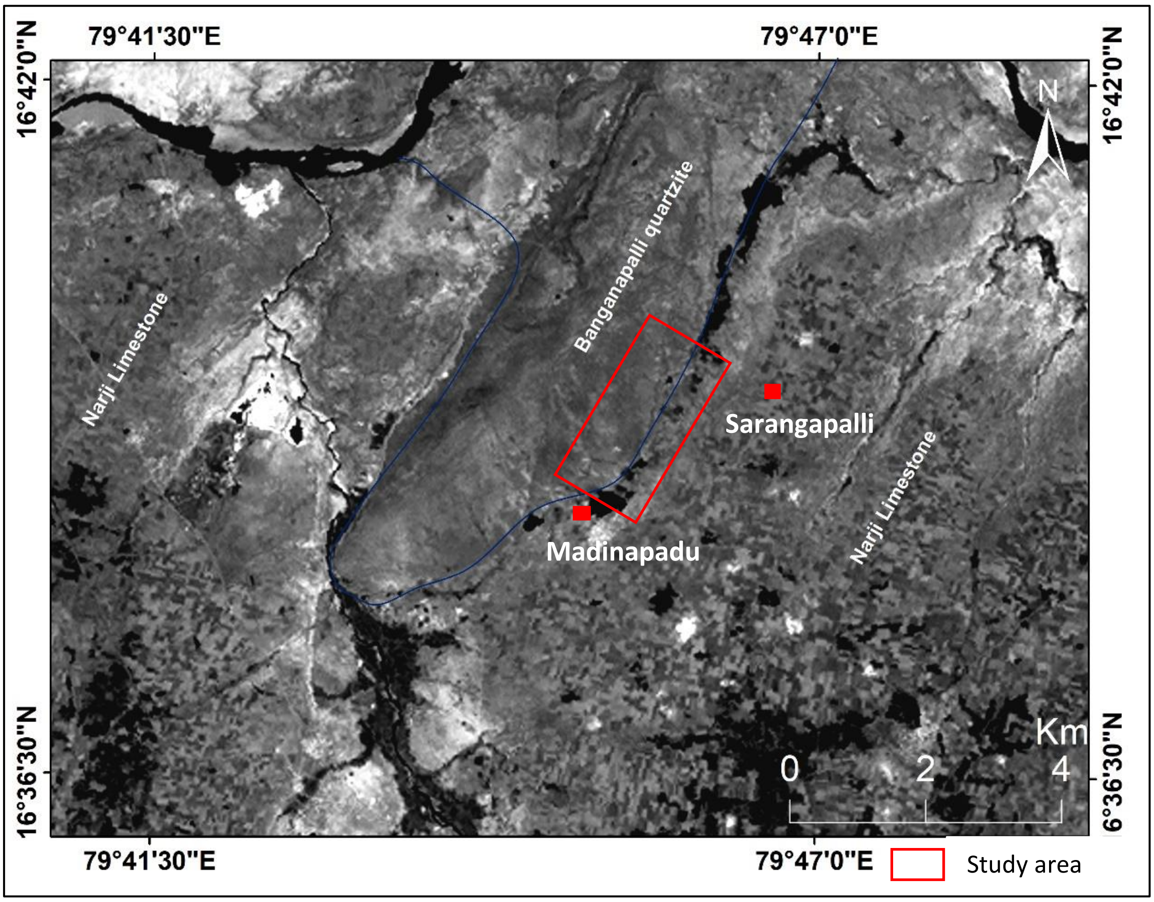

Figure 3.1 PC1 Image of study area showing boundaries b/w Banganapalle quartzite and Narji limestone.

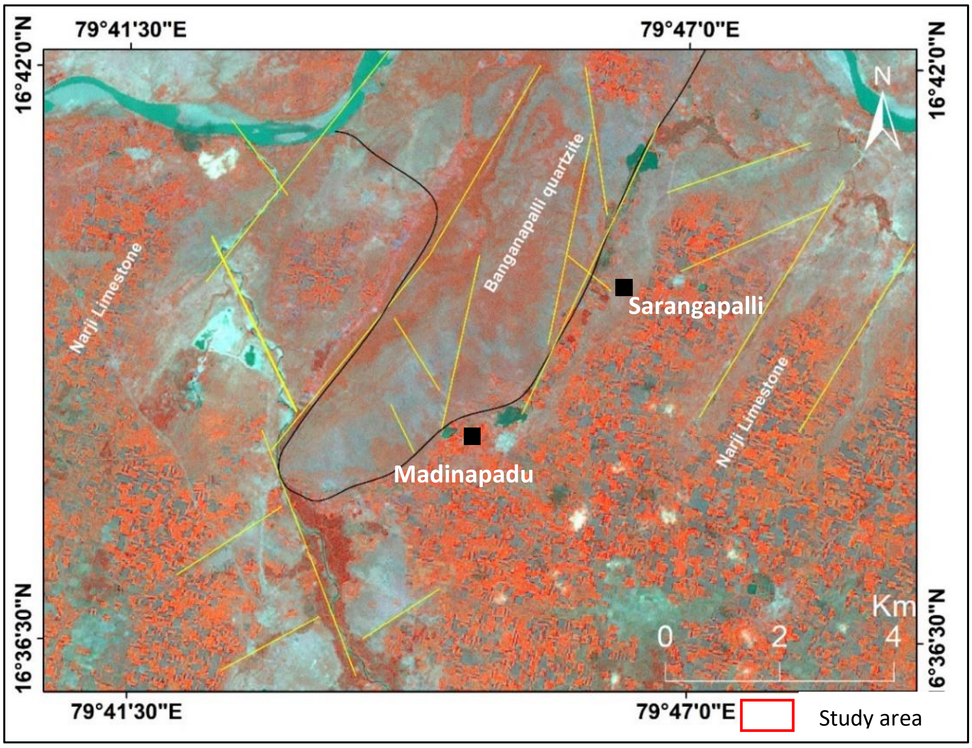

Figure 3.2 FCC (RBG) Image showing manually extracted lineament over study

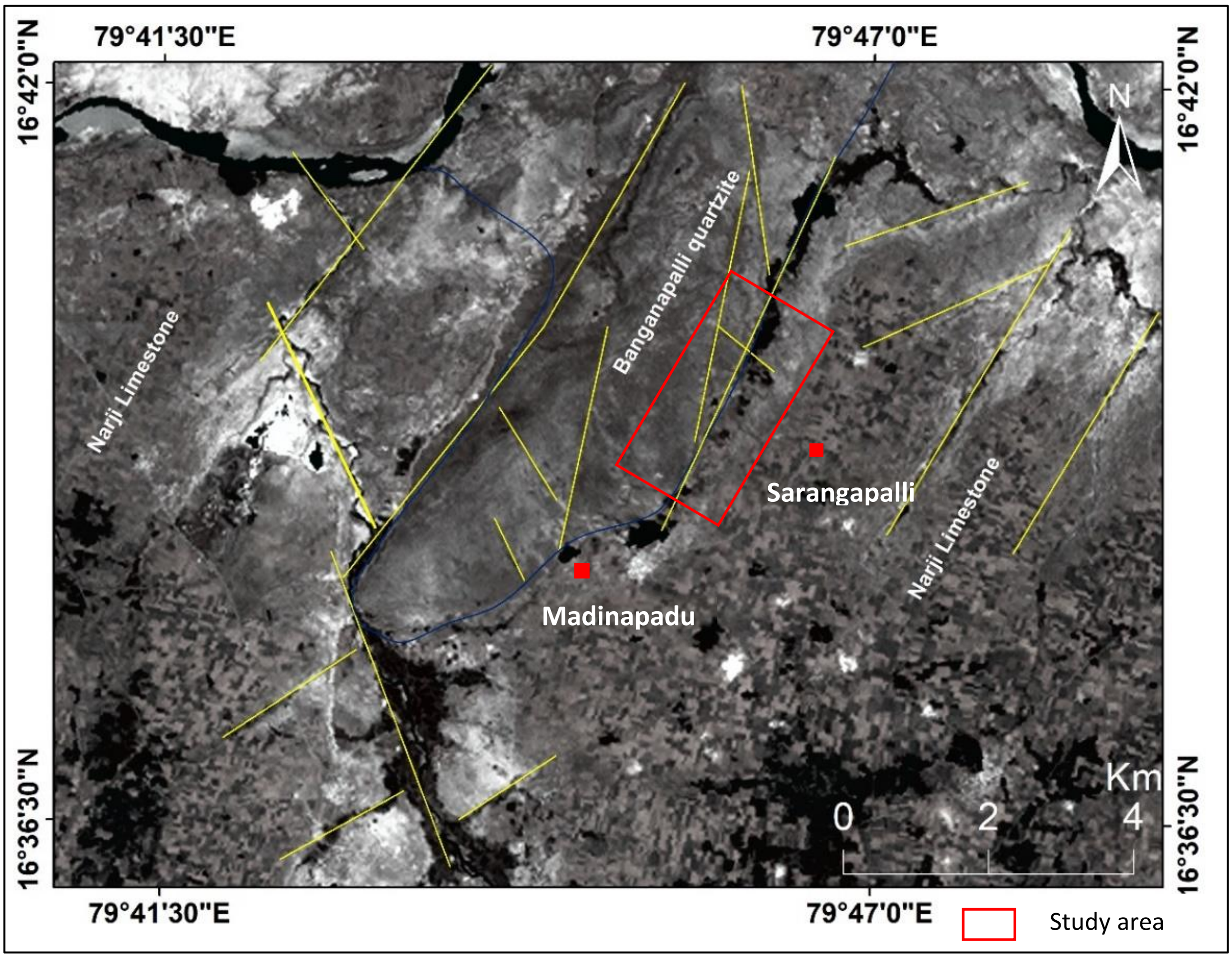

Figure 3.3 PC1 Image showing manually extracted lineament over study area.

(Figure 3.2 & 3.3). Sharp bend in NW-SE trending fracture in the south- western part of Banganapalle quartzite is clearly indicating NE-SW trending fault to the west of quartzite body.

## 3.2 MAPPING

### Traverse planning, plotting and recording of geological data

Few Regional traverses/orientation survey have been taken up to understand the ground condition of the study area. To know the maximum variation in the contact zone between Banganapalle and Narji, E-W profiles were preferred. At every location observation have been recorded such as, location (Lat, Long), lithology and their variants, structures (sedimentary and tectonic), attitude of the strata (strike/dip, dip direction), elevation and proper photographs of the features etc.

Geological observations and inferences made during field work have been plotted on the base map to prepare a complete geological map of the area. The data plotted on the map generally are: 1. Outcrop / projected outcrop pattern of different mappable rock units; 2. lithological contacts 3. Attitudes of primary structures like bedding, cross bedding etc. 4. Attitudes of secondary structures like fold, fault, and joint etc. (v) attitude of linear features. All these features have been plotted on the map using standard symbols. Different mappable rock units identified, traced and plotted them on the map. The approximate position and character of the concealed rocks are indicated by inferred litho-units and inferred contacts.

The study area is located at the northern part of Palnad sub-basin and exposes Kurnool Group of rocks represented by Banganapalle Quartzite and Narji Limestone. The contact between these two formations is marked by a N25°E trending fault (extending~5 km), which entrained the Banganapalle quartzite above the Narji limestone. The contact between the rock units is not discernible, mostly masked by cultivated land, probably due to higher degree of weathering along area of strain localization. Prepared detailed geological map (1:5000) of Sarangapalli area is shown in Figure3.4 along with section line A-B showing the faulted contact between Banganapalle and Narji formations.

The nature of contact between both the lithounits has been inferred as NE-SW trending reverse fault. The faulted nature of contact is evidenced by abrupt termination of lithologies, stratigraphical order indicates upliftment of Banganapalle Quartzite, major lineament in satellite imageries, presence of drainage, intense fracturing and quartz veination along the contact zone.

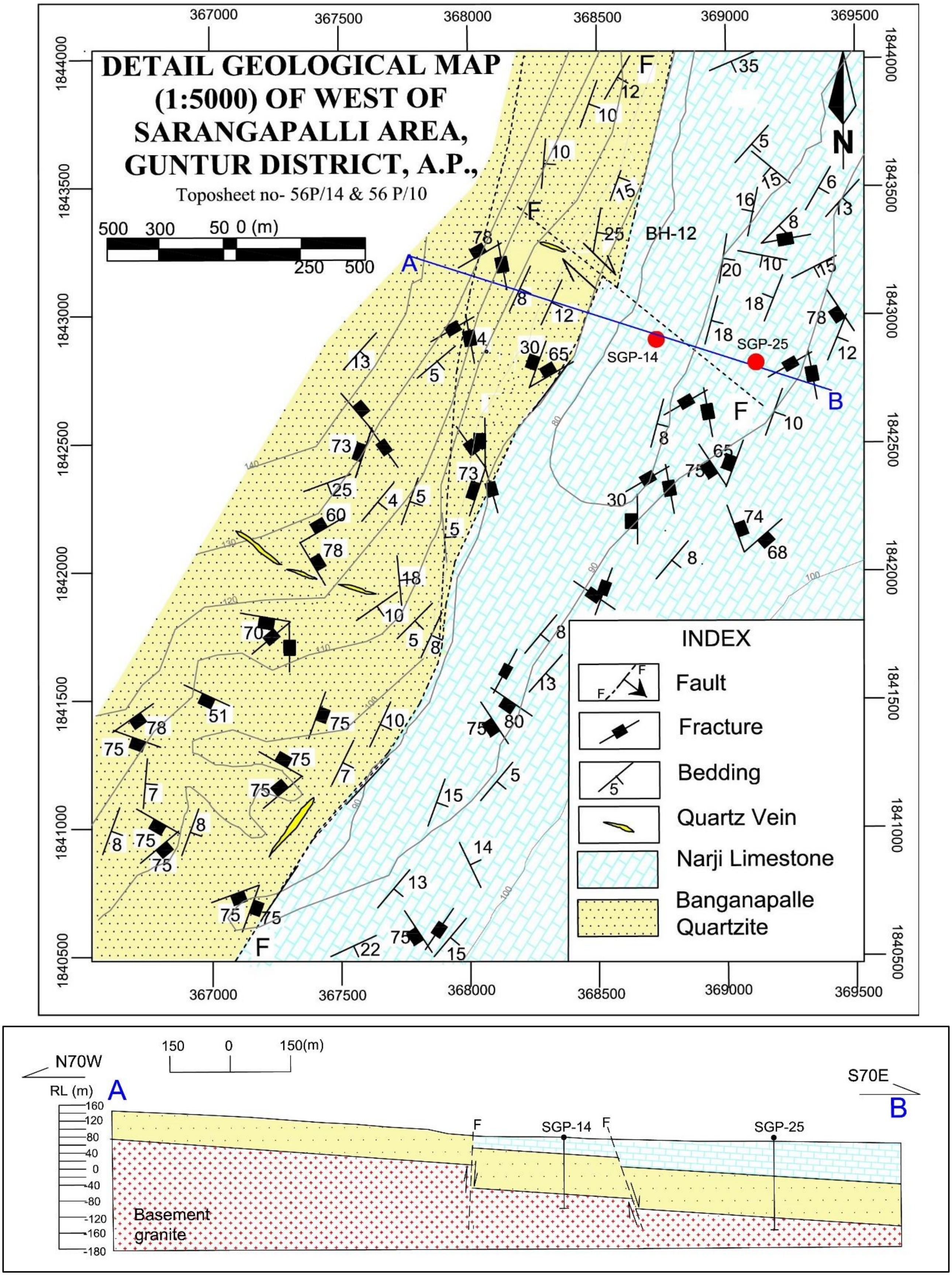

Figure 3.4 Geological map (1:5000) of Sarangapalli area (Above). Cross section along line A-B (below)

### 3.2.1 Banganapalle Quartzite

It is mostly represented by a massive to occasionally current bedded, grey-white to grey coloured, fine to medium grained, chemically matured, hard and compact orthoquartzite. It contains <5% of matrix and > 95% of quartz clasts, among total clast component, hence characterized as quartz arenites. The framework is clast supported, having moderately to well sorted, sub-rounded to rounded clasts bound by silica cement and matrix. The orientation of bed is sub-horizontal ($4^0$ to $22^0$), dipping towards SE (Figure 3.5 a). Bedding is mostly obliterated because of massiveness in quartzite, though cross bedding as primary sedimentary structure is commonly observed in this rock unit (Figure 3.5 b). The whole lithounit exposed in the mapping area is intensely dissected by fractures of various trends, along with quartz veination associated with considerable number of fractures (Figure 3.5 c&d). Due to intense ferruginization it appears red at the surface. Limonitic encrustation at the surface of beds was recorded at few locations. Background radioactivity in this litho-unit is 1-2 ppm (taken by Radiation survey meter / RSM).

### 3.2.2 Narji Limestone

It is represented as grey white, greyish green to dark grey coloured, fine grained, hard and compact, laminated planer bedded to massive limestone. The beds are generally sub-horizontal, dipping towards SE with the dip amount ranging from 2° to 22°. Convolute lamination as penecontemporaneous deformation is commonly observed. Pressure solution feature (stylolite) has also been observed as evidence of penecontemporaneous deformation (Figure 3.6a).

These stylolites are generally parallel to the bedding plane and shaped like “beds of nails” overall planer, but with pointy bits that poke up and down, perpendicular to that plane. Oxidized pyrite has been encountered at places. Differential weathering in impure limestone has also been observed along the traverses. It is moderately fractured with major trends NW-

SE and NE-SW, among which quartz and calcite veination along NE-SW trending fractures has been recorded at some place (Figure 3.6b&c). Differential weathering is also noted at places (Figure 3.6d). Background radioactivity in Narji limestone ranges 2 to 3 ppm (taken by Radiation survey meter / RSM).

Panoramic view of Banganapalle Quartzite and Narji Limestone is given in Figure 3.7.

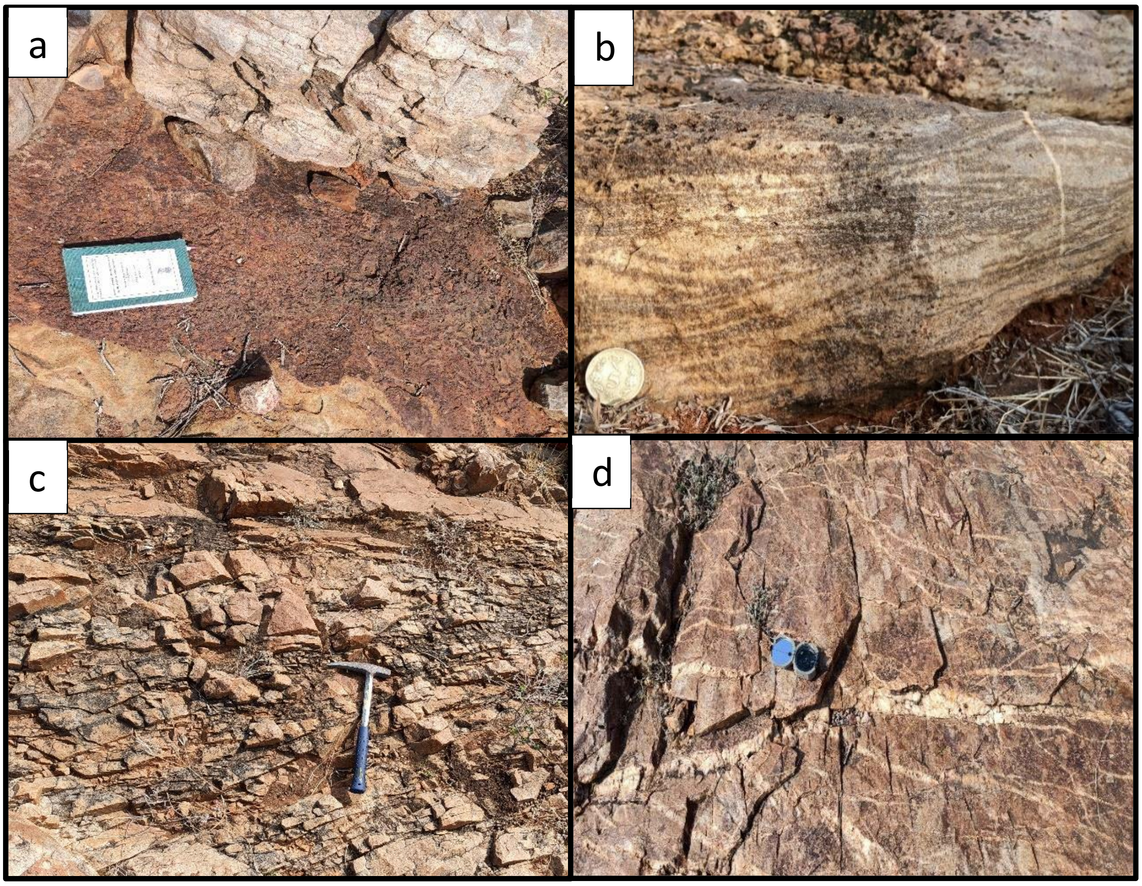

Figure 3.5. (a) Limonitic encrustation at the surface of Banganapalle quartzite, (b) Trough cross bedding in Banganapalle quartzite, (c) Highly fractured Banganapalle quartzite and (d) Network of quartz veins (NE-SW and NW-SE) in Banganapalle quartzite.

## 3.3 STRUCTURAL FRAMEWORK

### (a) Fractures

Fractures are planer or sub planer discontinuities, creating two free surfaces, across which the cohesion of the material is lost, develops due to brittle deformation. A widely observed correlation between high fracture density and mineralization throughout terranes and geological time indicates a fundamental underlying ore-forming process. A total number of 488 joints/fractures data have been collected from the exposed outcrop of the litho-units in the study area and their corresponding rose diagrams have been prepared (Figure 3.8a&b). All the

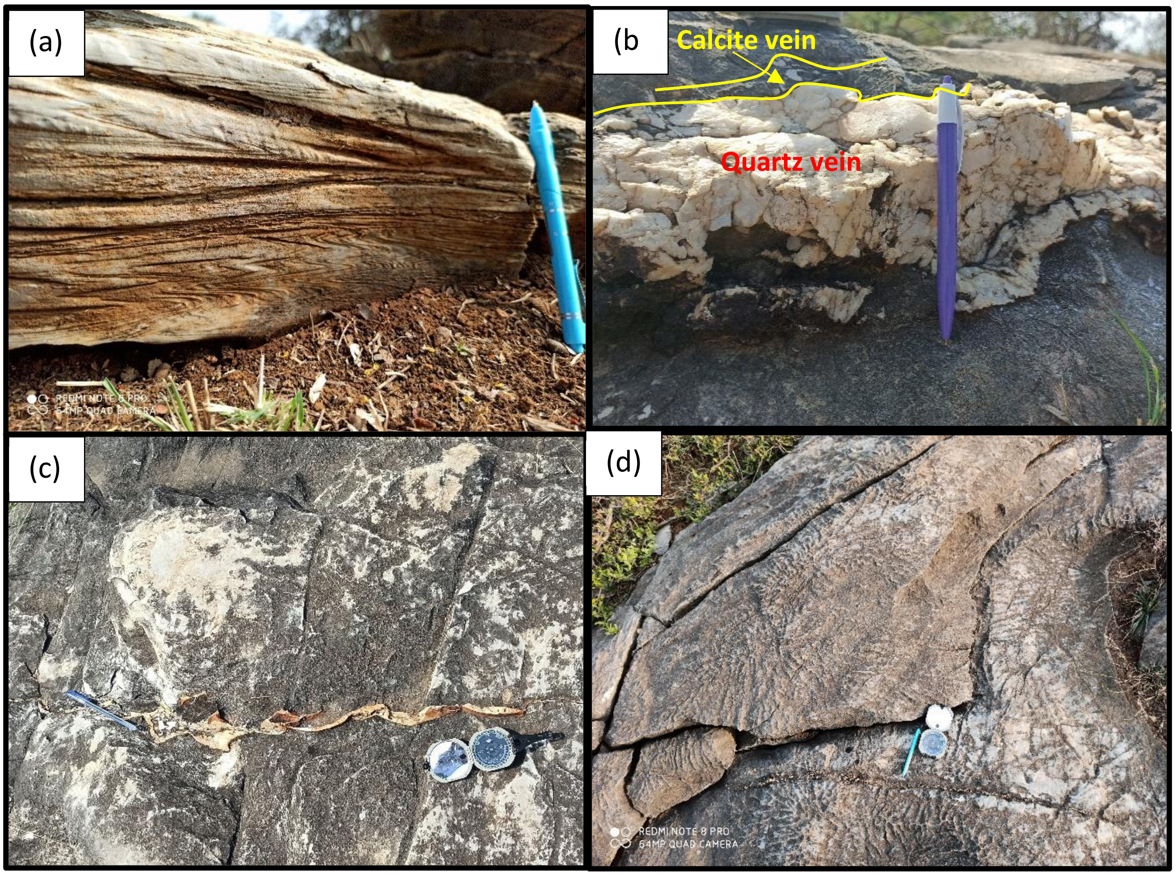

Figure 3.6 Convolute lamination in Narji limestone, (b) & (c) Quartz and Calcite vein in Narji limestone, (d) Differential weathering in limestone.

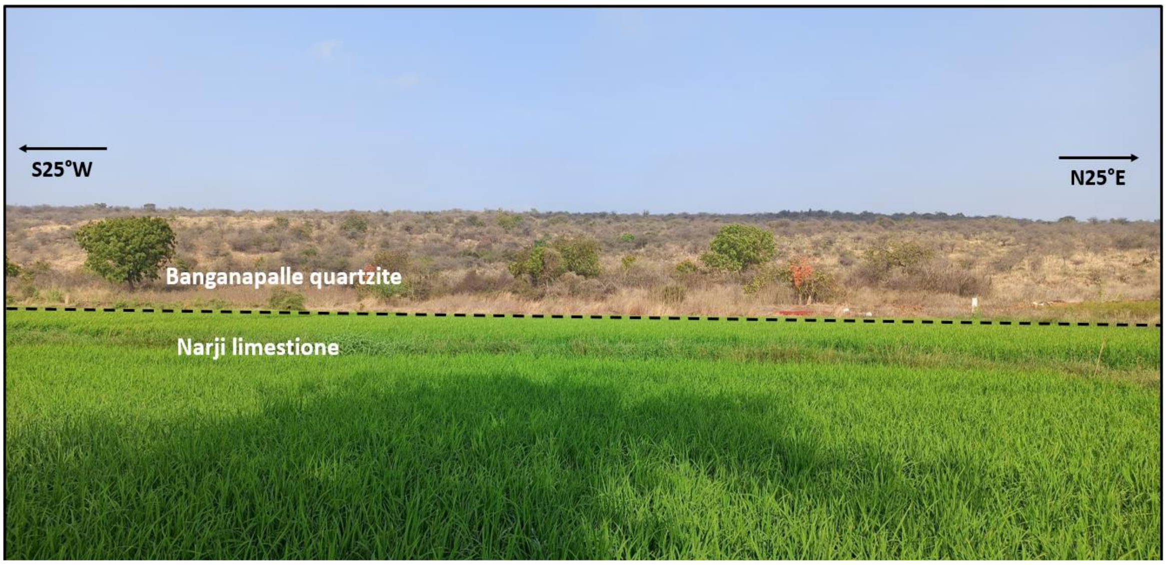

Figure 3.7 Panoramic view of Narji limestone (masked by cultivated land) and Banganapalle quartzite hillock.

fractures sets are mainly sub-vertical to vertical with length and spacing between the fractures varies from centimetre to meters. Both the litho-units show polymodal distribution of fractures (Figure 3.8a&b).

### Banganapalle Quartzite

The Banganapalle Quartzite is intensely fractured and multidirectional fracture sets have been recorded in the field traverses. Major fracture trends N-S, NE-SW, NW-SE and E-W are recorded in Banganapalle quartzite (Figure3.8 a). The density of fractures increases near the fault zone (NE-SW trending fault).

### Narji Limestone

The intensity of fractures is less in Narji limestone in comparison to Banganapalle Quartzite. Trend of prominent fractures/joints planes are recorded 310°, 35°, N-S and E-W. Corresponding rose diagram for these fractures showing that major concentration of fractures is confined in NW-SE direction (Figure 3.8 b), perpendicular to regional strike direction. The NE-SW fracture set is occasionally filled with quartz veins. Association of calcite vein with quartz vein in NE-SW trending fractures were also observed in Narji limestone.

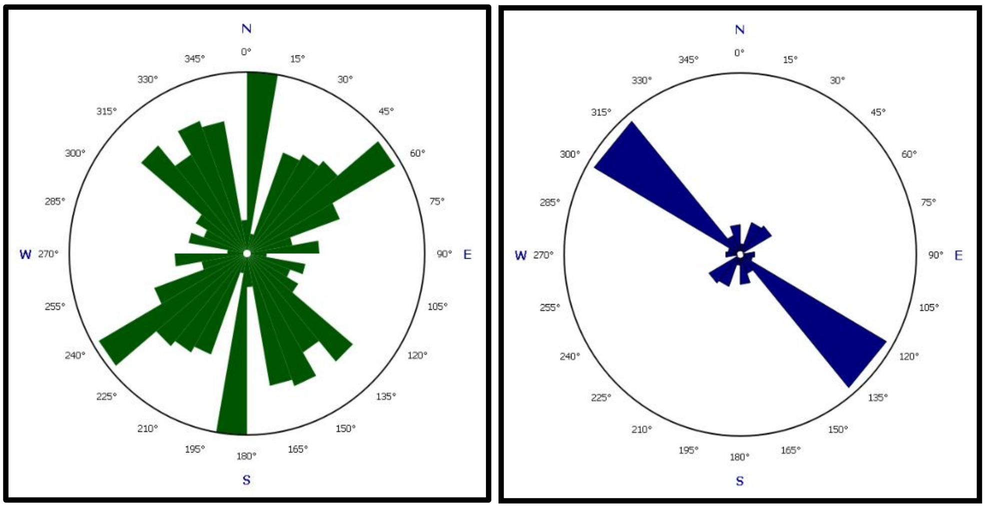

Figure 3.8 (a) Polymodal trends of mapped fractures in quartzite (n=288), (b) Bimodal trends of mapped fractures in limestone (n=200)

### Chronology of Fractures

To understand the stress regime, fracture data (n=558) were collected and plotted using rose diagram which suggest four major trends of fractures in the area. NE-SW and NW-SE trending fractures are more common than N-S and E-W trending fractures. Based on field observation such as cross cutting relation between the different fractures (Figure3.9), chronologically N-S trending fractures were recorded as oldest followed by NE-SW, NW-SE and E-W. and E-W (Youngest).

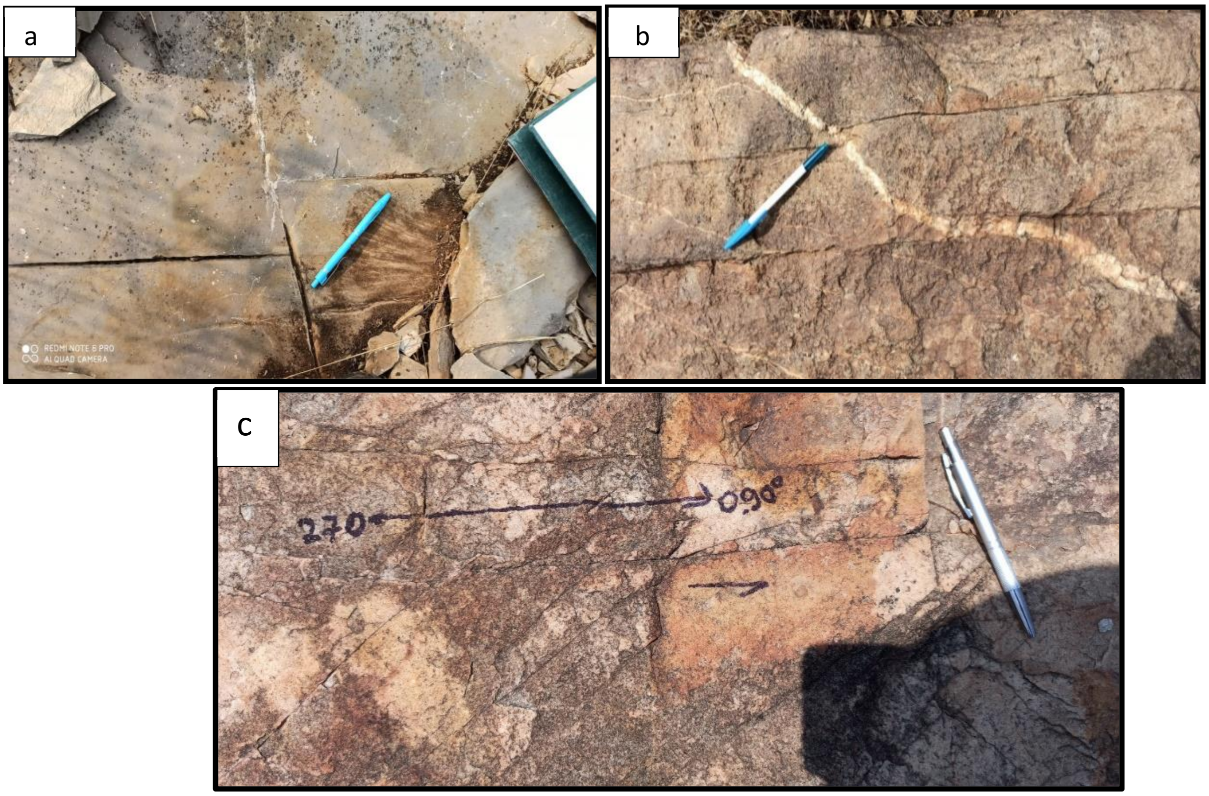

Figure 3.9 (a) NE-SW fracture is older than NW-SE trending fracture set in Narji limestone (pen is pointing towards north), (b) NW-SE fracture filled with quartz vein is younger than NE-SW trending fracture in Banganapalle quartzite (pen is pointing towards north) and (c) E-W in younger than NE-SW fracture set.

### (b) Quartz Veination

Quartz veins are found in association with both the lithounits. These veins are mostly fracture related and have clear contacts with their host rocks.

#### Banganapalle Quartzite

Quartz veins of thickness centimeters to decimetres and from decimeters to hundreds of meters long was very frequently observed and recorded in Banganapalle Quartzite. The density of quartz veination increases near the NE-SW and NW-SE trending faults (Figure 3.10). Veination along NE-SW, NW-SE, ENE-WSW is commonly observed in the field exposures of the area (Figure 3.9 a). The NW-SE trending quartz veins in Banganapalle quartzite are mostly thicker (decimeters) and longer than other veins in the area are correlatable with larger fractures / NW-SE trending cross fault (Figure 3.10 a).

**Narji limestone**

Quartz veination was occasionally observed in Narji limestone. The dimension of veins recorded in Narji limestone is readily less (mostly cm scale). It is dominated by NE-SW trending fracture filled quartz veins mostly associated with calcite vein.

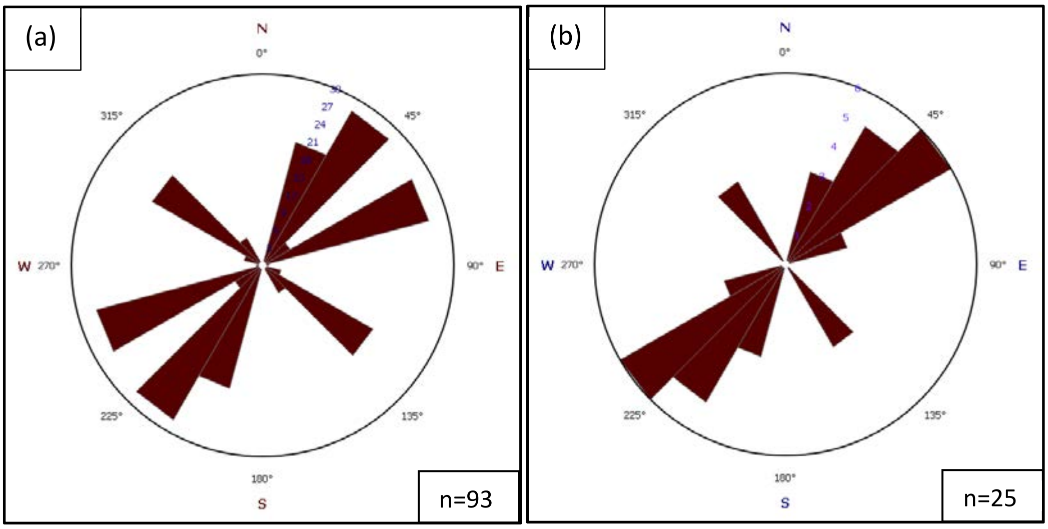

Figure 3.10 Rose diagram for quartz veins trend analysis, (a) Banganapalle quartzite and (b) Narji limestone.

**Quartz veination** is mainly confined with NE-SW and NW-SE trending fractures having dimension cm to >100m in length and cm to >5 m in width. Highly fractured rock and intense quartz veination suggesting that Banganapalle quartzites might have been affected by multiple phases of deformation in geological past. Quartz veination is indicative of Post-Narji hydrothermal event in the study area.

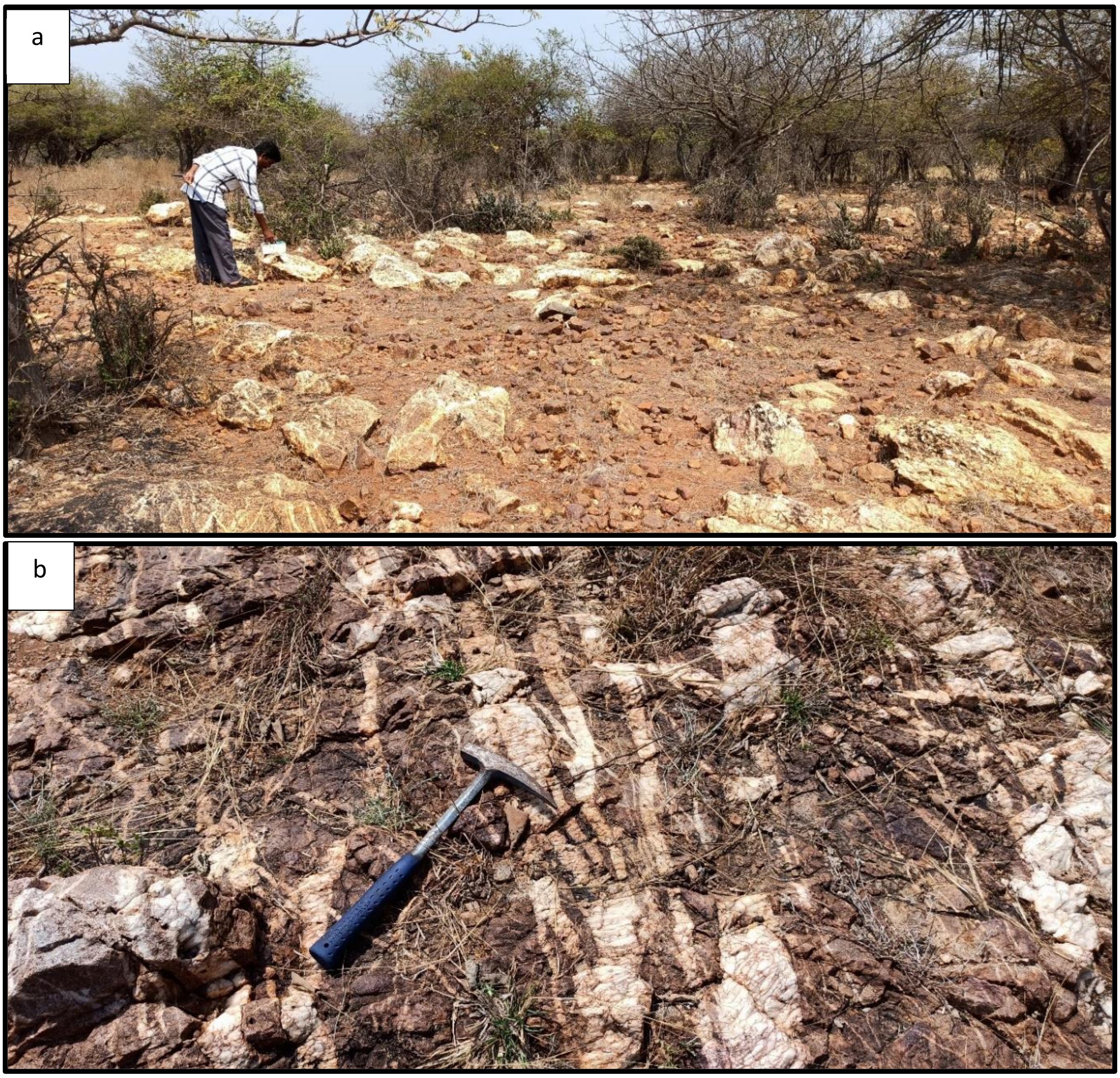

Figure 3.11 Quartz veins in Banganapalle quartzite: (a) NW-SE trending thick quartz vein, (b) Intense veination near the NE-SW trending fault zone along NE-SW trending fractures.

### (c) Tension gash

Quartz filled veins have been recorded in en-echelon pattern within the Banganapalle Quartzite in the study area (Figure 3.12). Presence of these slightly sigmoidal-shaped array of quartz veins clearly indicates the movement or shearing along some particular zone within the quartzite. Generally, tension gashes form in different stages of shearing. Rotation of these veins are mainly controlled by the intensity of the shearing. Rare but typical shear sense indicator “tension gashes” recorded in field identified as riedel shear corresponding to main NE-SW trending fault indicating shearing along the fault. The geometry of these veins reveals slight to moderate sigmoidal nature which may indicate the variable influence of shearing on the fracture filled veins. Principal stresses have been analysed with the help of tension gashes indicate N-S compression and nearly E-W extension.

Acute angle between tip of the sigmoidal shaped quartz veins with the shearing plane indicates the sense of shearing. Here, the top tip indicating N45$^0$E sense movement. In this area such features were recorded rarely but presence of few such type of feature indicates the movement in N45$^0$E-S45$^0$W direction.

Direction of principle stresses also have been measured using the study of tension gashes. Minimum compressive stress σ3 which is normal to the un-rotated part of the gash vein showing near about East-West extension and σ1 (Maximum compressive stress) perpendicular to the σ3.

**(d) Slickensides**

Few slickensides/striations (n=03) have been noticed within the Banganapalle quartzite. Because of scarcity of such type of structural data in the area, it has much significance. Slickensides/striations are generally indicating friction slip along the weak plane during faulting and folding. In the area, planes belong to such striations are considered as fracture planes along which movement have been taken place.

Figure 3.13 displaying striation is pitching nearly parallel to the trend of the existing fracture plane (310°/ 75°→040°). It has been considered as strike-slip movement with 8 ° dip component. It is the rarest evidence which has been recorded as strike slip movement. The particular fracture trend is also spatially correlatable with the similar trending fault which has been recorded in the borehole data.

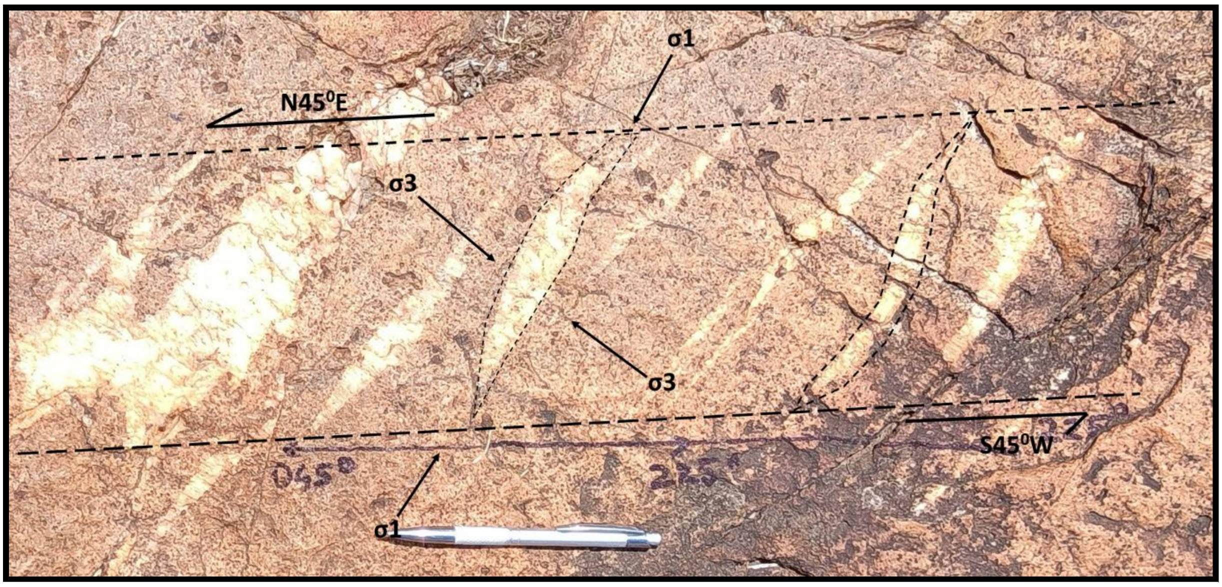

Figure 3.12 Quartz-filled tension gash within the Banganapalle quartzite

Figure 3.13 Striation observed along NW-SE (N310) fracture plane in Banganapalle quartzite.

### Evidences of NE-SW trending fault

- Presence of NE-SW trending lineament on satellite image.
- Banganapalle quartzite standing above the Narji limestone.
- Intense fracturing and brecciation along the fault zone.
- Intense veination (NE-SW trending) along the fault zone.

- Presence of NE-SE drainage along the weak plane.
- Presence of NE-SW shearing plane (deduced from tension gashes) suspecting oblique slip nature of fault.

**Evidences of NW-SE trending fault**

- Presence of NW-SE trending lineament on satellite image.
- Intense fracturing and development of ferricrete was witnessed along the slip planes (Figure3.14)
- Presence of thick quartz vein near the fault zone.
- Vertical displacement in lithounit recorded in borehole data.
- Presence of drainage along weak plane generated due to faulting.

Fault-slip measurements reveal presence of NW-SE trending cross fault displacing the earlier NE-SW trending major fault. Fault-slip data recorded in manner of pitch and plunge of the slickenside and attitude of associated plane suggesting the oblique to bedding parallel slip having normal and dextral sense of movement which is also supported by drainage, lineament on satellite imagery, development of ferricrete along the fracture zone and throw (up to 50m) recorded in borehole data.

Based on the detailed field observation, it has been observed that geologically the study area is influenced by deformation as manifested by highly fractured nature of the rocks. Faults/fractures provide path for the fluid mobilisation.

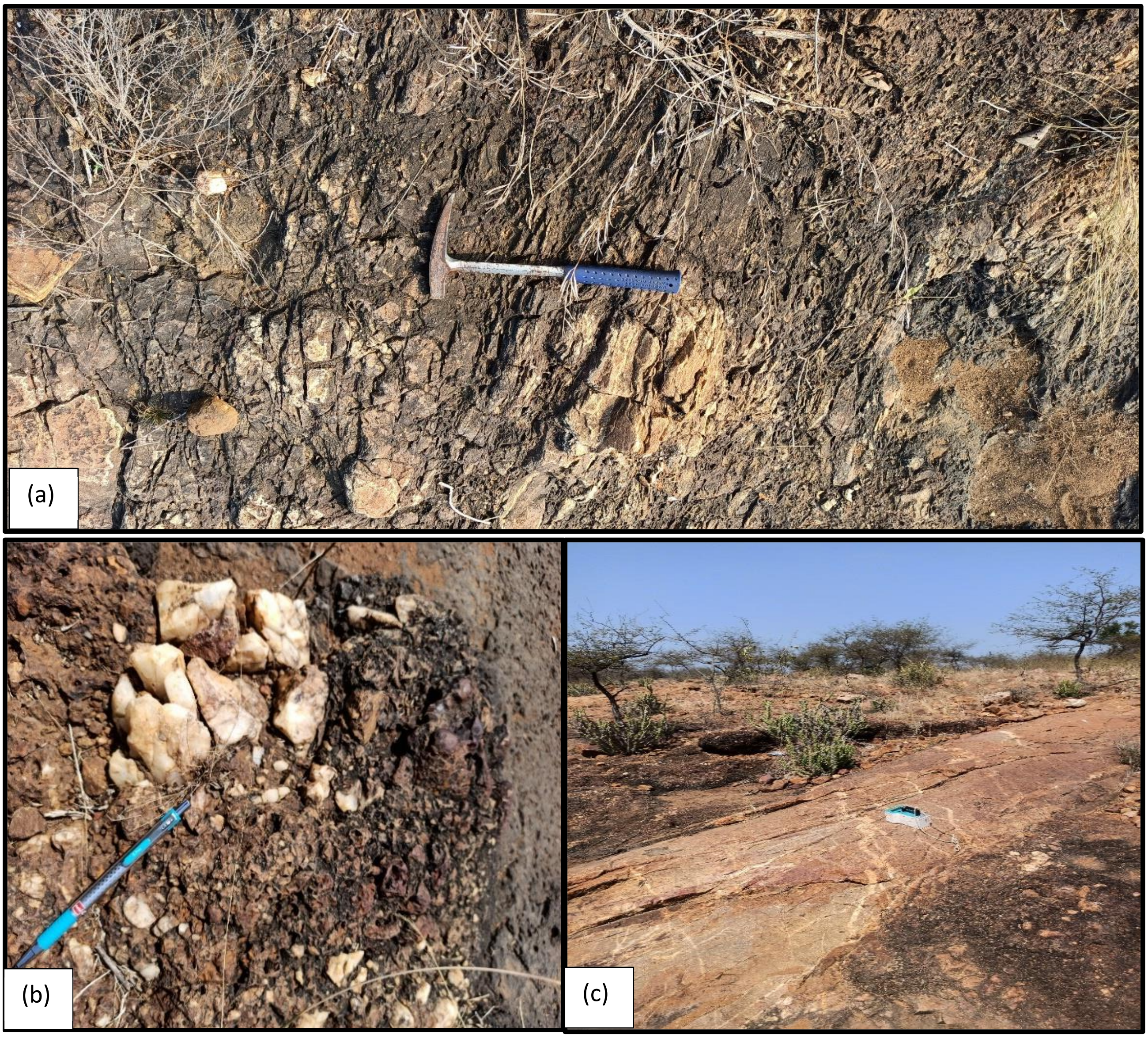

Figure 3.14: Field photographs of Banganapalle quartzite showing, (a) Intense fracturing, (b) Development of ferricrete along the NW-SE trending fault (c) veination along the fault zone.

## 3.4 INTEGRATION OF FIELD DATA WITH AVAILABLE AIRBORNE GEOPHYSICAL DATA:

Geophysical data helps in understanding the subsurface lithology/geology depending on the variation in physical properties of rock like, density, magnetic susceptibility, electrical conductivity and radio elemental distribution. It is also helpful in estimating/interpreting disposition and chronology of geological structures. Potential methods namely, gravity and magnetic methods are being used over a century to map basement topography and structures. Northern part of Cuddapah basin was flown using, VTEM system comprising time domain electromagnetic, magnetic and radiometric data, during the year 2009-10.

In general, the conductivity is observed due to shales, carbon phyllites, highly fractured formations, alterations and saline water. Recent advances in airborne EM equipment has increased the dipole moment of airborne transmitters and reduction in system noise levels, induced polarization effects are now routinely detected usually at later delay times after EM transients have decayed (Macnae, 2016). These induced polarization effects are only detectable in the near surface. Taking this fact and surficial nature of conductivity into account the transients having the negative EM response have been studied. These negative EM responses are due to the presence of disseminated sulfides and alteration features (Ramesh Babu, et al., 2017).

. The figure 3.15 shows the dB/dt channel image of 26th channel of VTEM data, overlaid by the EM and magnetic data. The conductive zone shown in red color are shales of Narji and Banganapalle Quartzite. The negative values in the image are the negative EM responses (dark blue color), indicating presence of sulfides and alteration zone below Banganapalle quartzite to the west of Sarangapalli area.

Magnetic data is useful in mapping basement topography, structures and magnetic dykes. The total magnetic intensity image is shown in Figure 3.16 showing higher amplitudes in the NE part indicating shallow basement or a granitic basement with higher magnetite content. The structures mapped from magnetic data (based on magnetic breaks) have three general structural trends, NNE-SSW, NE-SW, NW-SE. Few faults/fractures interpreted from the magnetic data coincide with EM interpreted structures indicating the disturbance/reactivation to be after sedimentation.

### 3.5.1 Observations

The geophysical data helped in identifying continuation of faults in soil cover areas. The total magnetic intensity image is revealing three major fracture/ fault trends, NNE-SSW, NE-SW, NW-SE in the study area. The NNE-SSW trending faults bounding Banganapalle Quartzite (Figure 3.18) suggesting upliftment of Banganapalle quartzite along these faults which is also observed during field studies. The NW-SE (N310) trending fault (strike slip) passing through Sarangapalli area displacing NNE-SSW trending fault (Figure 3.16). This fault has dextral sense of movement and is well correlatable with the field studies (fault which is located between borehole nos. 12 and 14, Figure 3.4). Slickenside data collected during field studies along this fault plane is revealing its oblique slip nature as already discussed in section 3.3.

From integrated studies of field data and geophysical data it is clear that the area is affected by tectonic activity in the geological past. Major structures are following NNE-SSW, NE-SW and NW-SE trends. E-W fracture set observed during field studies is not controlling any major feature. NNE-SSW trending major faults in the area are believed to form earlier followed by NW-SE trending faults.

The negative responses extracted from dB/dt image of 26th channel of VTEM data are below the Banganapalle Quartzite, which is bounded by two NNE-SSW trending faults as observed in Figure 3.15. Presence of major structures (faults/ fractures), sulfides and alteration zone are making this area suitable for unconformity proximal uranium mineralization.

Geophysical interpretation overlaid on geological map given in Figure 3.17.

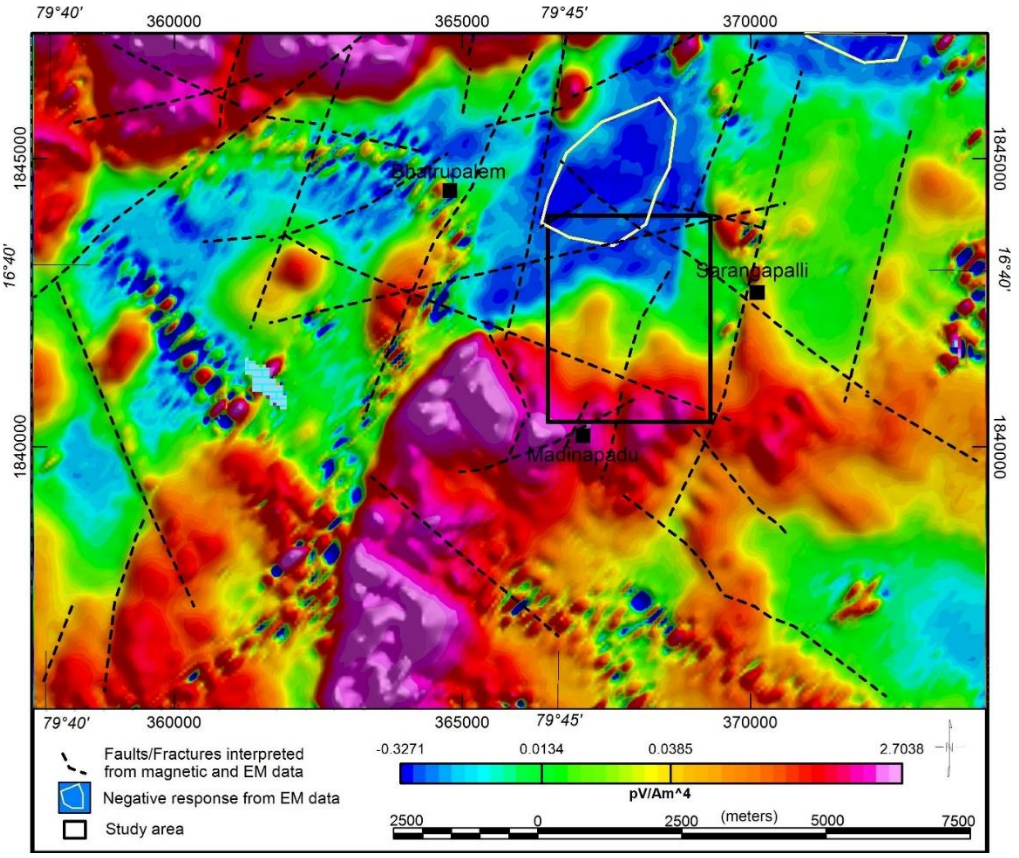

Figure 3.15 HTEM late channel 26 grid image (1953 µs) image. The blue zones highlight the negative responses recorded over the outliers (shown in yellow polygons) to the west of Sarangapalli area.

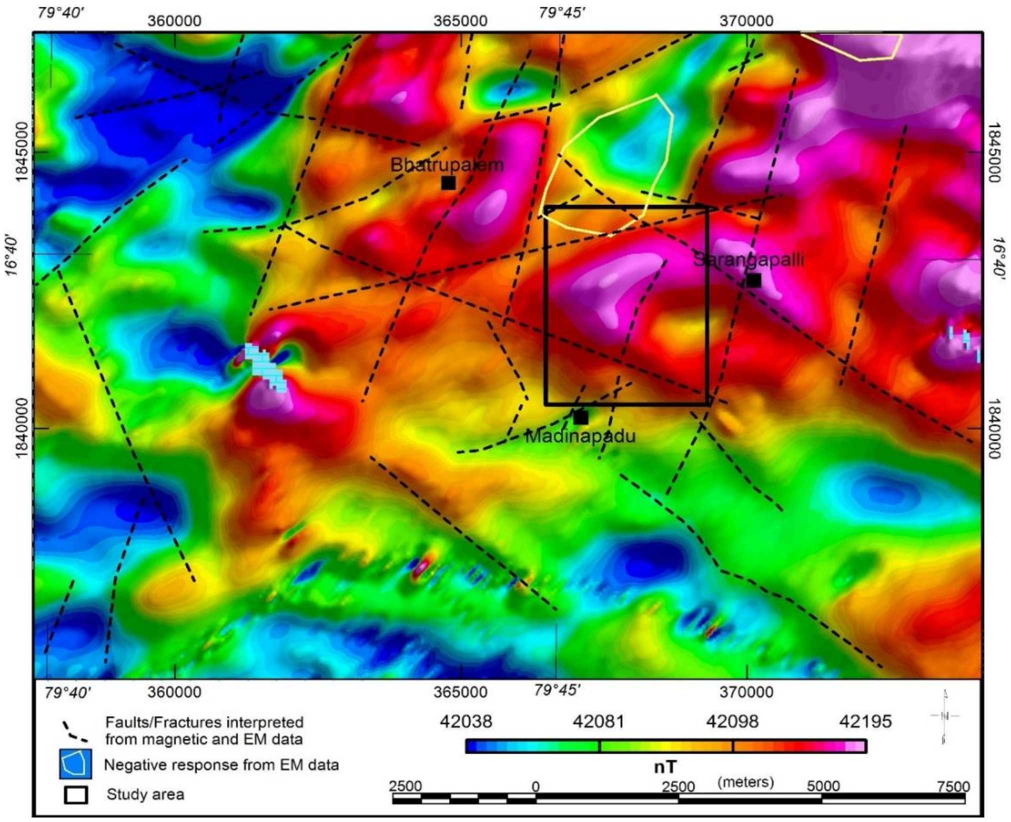

Figure 3.16 TMI (Total Magnetic image of Sarangapalli-Madinapadu area with demarcating major fault/ fractures present in the area.

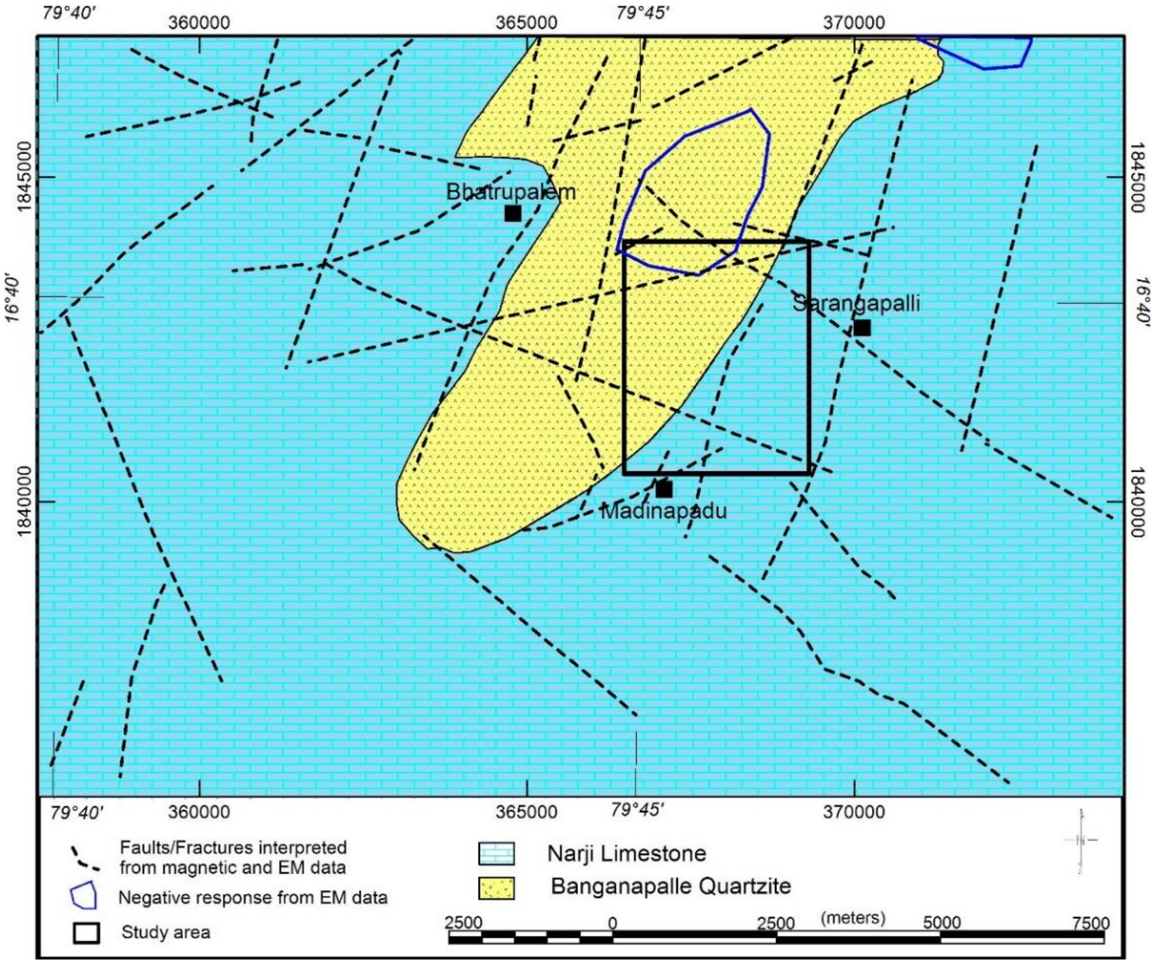

Figure 3.17 Geological map of Sarangapalli-Madinapadu area overlain by Magnetic and EM data.

## 3.5 ISOPACH AND ISOGRAD MAP OF MINERALIZATION

Isograd and isopach maps of mineralization (0.01% $U_3O_8$ cut off) have been prepared using Surfer software. The trend of ore body is NE-SW, parallel to the main fault present in the area. The prepared isograd, isopach map given in figure 3.18a&b respectively. Overlaid image of isopach and isograd map is given in figure 3.18c.

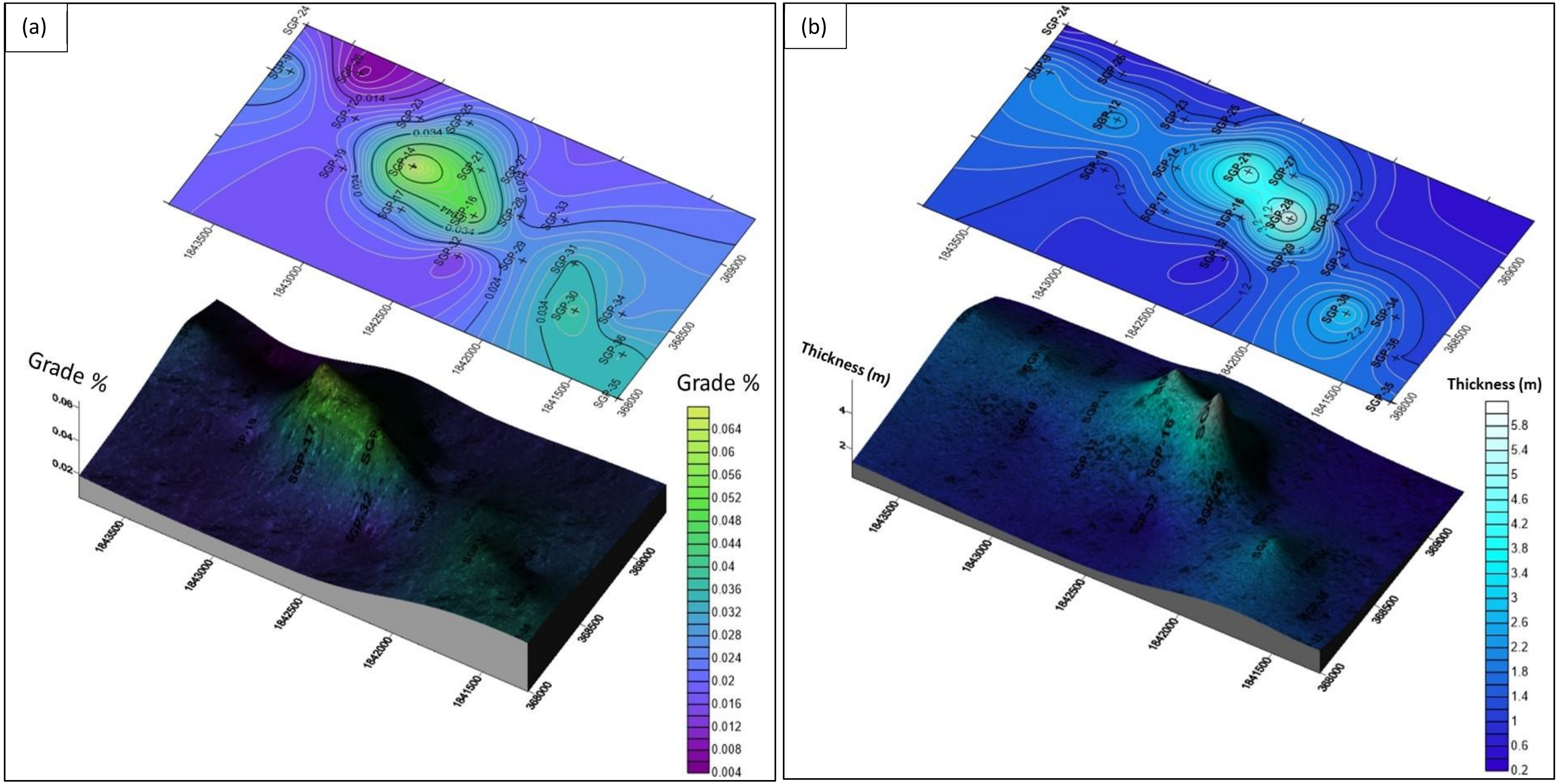

Figure3.18 (a) Isograd Map of mineralization, Sarangapalli area, Guntur district, Andhra Pradesh, (b) Isopach Map of mineralization, Sarangapalli area, Guntur district, Andhra Pradesh.

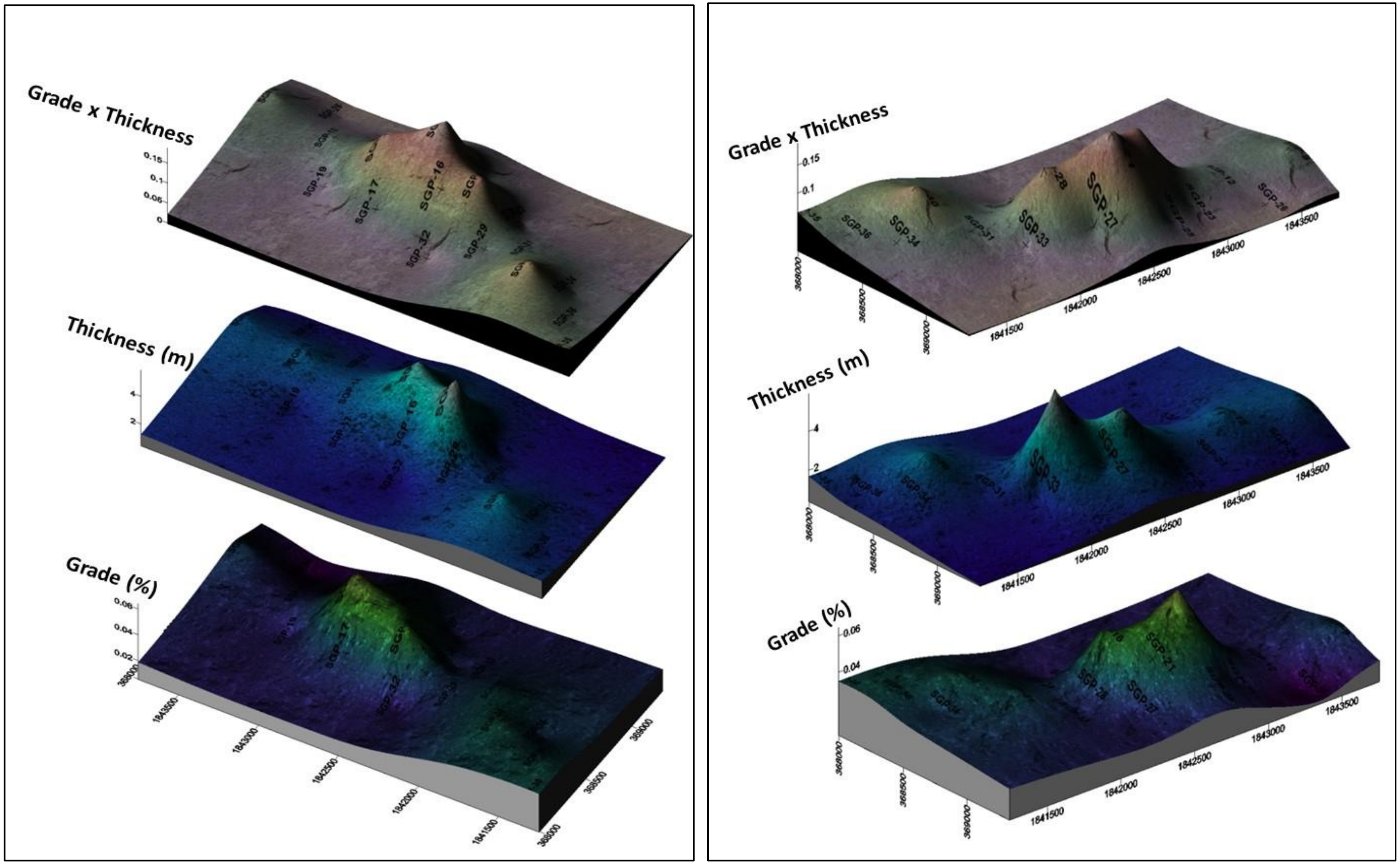

Figure3.18 (c) Overlying image of isograd, isopach and grade*thickness map (3-dimentional). Left: Normal view, Right: Reverse view.

# CHAPTER 4

# PETROMINERALOGY

For host rock characterization of Sarangapalli-Madinapadu area systematic sub-surface sampling (n=24) has been carried for petromineralogical studies. Samples have been studied mesoscopically as well as microscopically and are characterised based on mineral assemblages, texture, grain size, mutual relationship, alteration features, radioactive mineral phases etc. Based on these studies dominant rock types are identified as quartz arenite, subfeldspathic arenite and and biotite granite.

## Sample Preparation

At the onset, the samples were megascopically examined and important observation were noted and representative samples were collected for microscopic studies. These samples were examined under the ultraviolet lamp for detection of soft and fluorescent secondary uranyl minerals. Friable samples were firmly cooked and cemented with a penetrating binding substance like canada balsam before slicing. In case of radioactive samples, radioactive portion was first selected using scintillometer and representative portion slabbed/sliced. The selected slabs/slices were subjected to chromogram test for locating concentration of uranium minerals with easily soluble uranium. The sample requires to be thin enough (approx. 0.03 mm) for light to pass through while studying under optical microscope. Hand grinding of the section is done using 400 mesh size silicon carbide powder with water and repeated with 600 and 800 mesh sizes. The representative thin slice of the sample is mounted on thin glass slide by colourless transparent cement (epoxy) having refractive index closer to the glass and ground to a thickness of 0.03mm. Both the cut slab and the glass slide mounted thin section were polished with diamond pastes of different grades (0.25μ, 1 μ, 6 μ) until a brilliantly reflecting surface was developed. The polished mounts and thin sections are suitable for incident light microscopic observation and alpha particle autoradiography. While commencing the petrographic study it was confirmed that the thin sections of standard thickness 30µm or 0.03mm of quartz and feldspar grains show first-order grey-white interference colours. Such observations confirm perfect alignment of the optical settings of the microscope for good petrographic observations.

### Supportive Aids used for Identification of Radioactive Minerals in Petrology Lab

All the economically important radioactive minerals have optical properties overlapping with common ore minerals. Only on the basis of optical properties, it may not be appropriate to characterize specific radioactive mineral.

Common aids used in petrology lab related to alpha particle autoradiography:

I). Cellulose Nitrate films

II). Chromogram test

### CN Film Autoradiography (SSNTD)

Cellulose Nitrate films are in the form of flexible sheets, available in two types.

**a)** CN-85 Film: Transparent and consists of 85-micron thick layer of cellulose nitrate on an inert polyester substrate.

**b)** LR-115 Film: It is deep red in colour and consists of 12-micron thick layer of Cellulose Nitrate.

Both the films are alpha sensitive with energies below 4 Mev and are insensitive to beta, gamma and light radiations.

### Methodology adopted in using alpha-sensitive film

CN-85 film was used for autoradiography. These films were put in direct and even contact with the polished surface of the radioactive mineral in the thin section for period ranging from 24 hours to upto 5 or 7 days depending on the nature of radioactive minerals. Before putting the film on a thin polished section, radioactive indicator marks were put on the glass slide, which will help for matching the film after the etching of the film. The indicator material is prepared by mixing of powder of uraninite, uranyl nitrate or MDU (yellowcake) in nail polish. After due time, the film was removed and etched in 10% aqueous solution of NaOH in case of CN-85 and 20% aqueous solution of NaOH in case of LR-115 film. Generally, the time allocated for etching in present case was 2-3 hours at 35° C to 40° C. But to be on safer side films were kept in the solution for overnight etching at normal room temperature to enhance the size of alpha tracks. The alpha bombardment on the alpha sensitive films causes damage to the structure of the film. So, when etched in alkali solution these phases will be more reactive compared to rest of the film. This will leave the tiny black marks on the film called as tracks; as these are due to alpha bombardment, therefore called as alpha tracks. These can be easily observed under the microscope. The pattern and density of the alpha tracks, when combined with other optical properties give fairly good idea about the radioactive mineral(s) present.

**1) Possible nature of the radioactive mineral-** If uranium and thorium occur as essential element in minerals it will give high-density tracks. But if they occur as non-essential elements the track density will be low. Thus, uraninite would always produce very high-density alpha tracks, whereas zircon would normally produce very low-density tracks.

**2) Mode of occurrence-** The occurrence of radioactive mineral source can be understood by examination of patterns formed by the alpha tracks. The trail of tracks may suggest that the radioactive minerals a vein like structure or occur along a fissure or weak plane whereas cluster of alpha tracks indicate that the radioactive minerals occur as discrete disseminated grains. The relative density of the tracks can only be matched keeping exposure time and etching conditions same.

The density of the tracks depends on

a) Nature and composition of radioactive minerals.

b) Size, as the finer grain of same mineral will give low density tracks than coarser grain.

c) Age of radioactive minerals- Two grains of the same size and minerals may give different density tracks, if they differ in the age. The grain older in age will give lesser density tracks in comparison to the grain of same mineral of the younger age.

**Advantage**

a) Easy to match with the radioactive sources.

b) Track contrast is good and can be enhanced by giving longer time for etching in case of CN - 85 films.

**Chromogram test**

It is a chemical method and used to locate the presence/absence of easily soluble / leachable uranium rich source. This method involves:

a) Taking a dried photo printing paper soaked in photographic fixer (called as hypo, chemically named as sodium thiosulfate)

b) Wetting this photo printing paper with 1:1 Nitric acid solution

c) The surface of the polished slab or thin / polished section is pressed against it for a minute.

d) Removing the slab and treating the paper in potassium ferro cyanide solution. One may get brown spots, rose-red spots, and these may correspond with presence of leachable uranium (U), copper (Cu) and Iron (Fe) in the samples respectively.

e) For confirmation a drop of NaOH solution is put on brown spot, if it disappears it confirms presence of mineral phase with leachable uranium, e.g. uraninite, pitchblende, coffinite, and secondary uranium minerals. Refractory minerals like brannerite and davidite respond negative (-ve).

Uranium (VI) oxide reacts with nitric acid

$$U_3O_8 + 6HNO_3 \rightarrow 3UO_2(NO_3)_2 + 5H_2O \;\ldots\ldots\ldots\; (4.1)$$

Uranium (IV) oxide reacts with nitric acid

$$3UO_2 + 8HNO_3 \rightarrow 3UO_2(NO_3)_2 + 2NO + 4H_2O \quad \ldots\ldots\ldots (4.2)$$

(Uranyl nitrate) + (Potassium ferrocyanide) →Uranyl ferrocyanide

$$2UO_2(NO_3)_2 + K_4Fe(CN)_6 \rightarrow (UO_2)_2Fe(CN)_6 + 4KNO_3 \quad \ldots\ldots\ldots\ldots (4.3)$$

The prepared thin section is observed under a polarising microscope "Leica DM2700P" for different optical properties of the constituting minerals.

### 4.1 Basement granite

**Megascopic Description:** In hand specimen it is medium to coarse grained light to dark grey colored granite with quartz, feldspars and biotite as essential minerals. Broadly this rock unit exhibits equigranular texture (Figure. 4.1a). Intense sericitization of feldspars is characteristic alteration feature present in the granite of Sarangapalli area near the unconformity contact. Due to appreciable presence of sericite the rock shows an overall dull yellow color (Figure. 4.1b) near the unconformity contact and nearly 3-4 meter below the unconformity contact. The rock is moderately fractured and these fractures are subvertical to vertical in nature and often filled with chlorite, quartz and pyrite. Chlorite occurs as fracture filling vein of thickness ~ 1mm identified by its dark green color and occurs throughout the granitic unit. These veins show criss-cross relationship sometimes (Figure. 4.1c). Chloritisation of biotite is present near the chlorite veins is identifiable with the help of hand specimen. Quartz veins of thickness ~ 1cm are present along the fractures are present at places (Figure. 4.1a). Pyrite is also present as fracture filling in granite suggesting its hydrothermal origin (Figure. 4.1d). At some places, pyrite present in close association with quartz vein along the fracture suggesting their origin from single hydrothermal event (Figure. 4.1e).

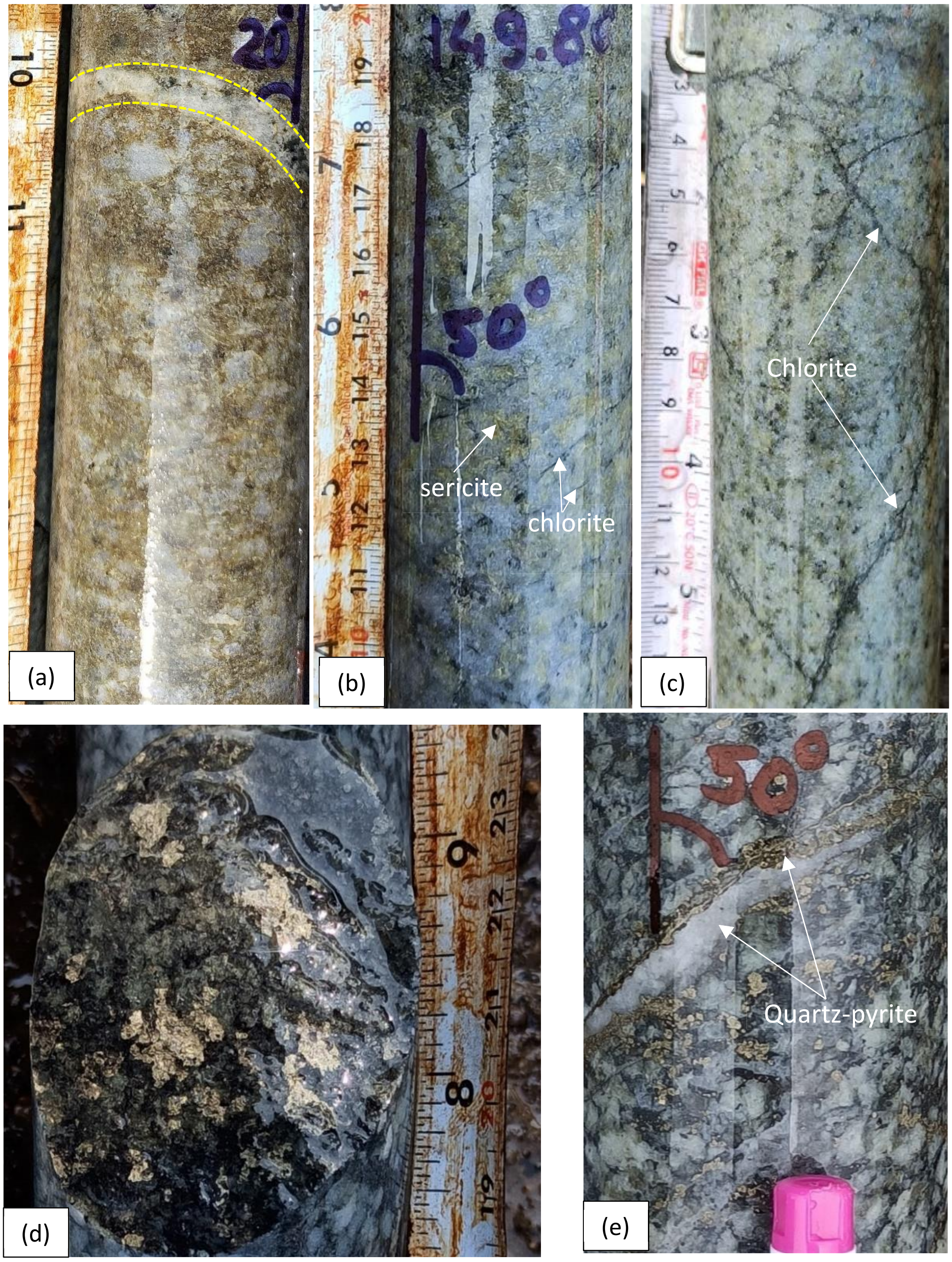

Figure. 4.1 Borehole core of granite showing, (a) equigranular (granitic) texture and a silica vein along a fracture, (b) feldspars altered to sericite (dull yellow) and chlorite (dark green to black) vein along the fracture, (c) Chlorite (dark green to black) vein along the fracture, (d) Pyrite as fracture filling and (e) Quartz-pyrite vein along the fracture.

**Microscopic Description:** Microscopically the rock is coarse grained. Quartz, orthoclase, microcline, plagioclase (albite-oligoclase) and biotite are essential rock forming minerals identified under microscope while zircon, allanite, magnetite, hematite, apatite and anatase are identified as accessary mineral phases. Quartz is mostly anhedral, while plagioclase and alkali feldspars are subhedral in nature (Figure.4.2a). Biotite mostly observed in flaky form (Figure.4.2b). The overall texture of rock unit is hypidiomorphic equigranular. Perthitic and myrmekitic intergrowth textures are very common in the studied samples. Zircon is zoned with perfectly euhedral (hexagonal) crystal phases. The perthite texture indicating exsolution due to cooling of a grain of alkali feldspar with a composition intermediate between K-feldspar and albite (Figure.4.2c). The myrmekitic texture is present as wormy intergrowth of quartz in feldspar (Figure.4.2d) developed during the late stages of crystallization if the two minerals (quartz and feldspar) grow simultaneously in the presence of volatile phase. Zircon sometimes occurs as inclusion in biotite (Figure.4.2e) and it is very abundant in comparison to other accessary phases (Figure.4.2f). Zircon found to be altered in samples which are selected from the radioactive zone (Figure.4.2g). The zircon susceptibility to alteration increases in crystals with structure disorder due to metamictization (Ewing et al., 2003) and fracturing (Krogh and Davis, 1975). Zircon grains with high concentrations of U (and Th) are generally more susceptible to alteration, since the radioactive decay of these elements leads to the progressive damage of crystal structure with time. Krogh and Davis, 1975 showed that the main effect of radiation damage is to prepare the crystal for later alteration, which can subsequently be initiated by interaction with fluid even at low temperatures. Degree of alteration of zircon with hydrothermal activity depends on the uranium content in the zircon (Kaulina et al., 2020). Allanite is also found in altered form (Figure 4.2g). Zircon and upto some extent allanite might have contributed as a source for uranium mineralization. (Figure. 4.2h).

**Deformation:** It is highly fractured and thus indicating brittle deformation in the area (Figure.4.2i). The intensity of fractures is more in samples containing radioactive minerals. Individual grains are fractured to various degree and these fractures are filled with sericitic and chloritic material. Polycrystalline quartz is observed indicating recrystallization (Figure.4.2j).

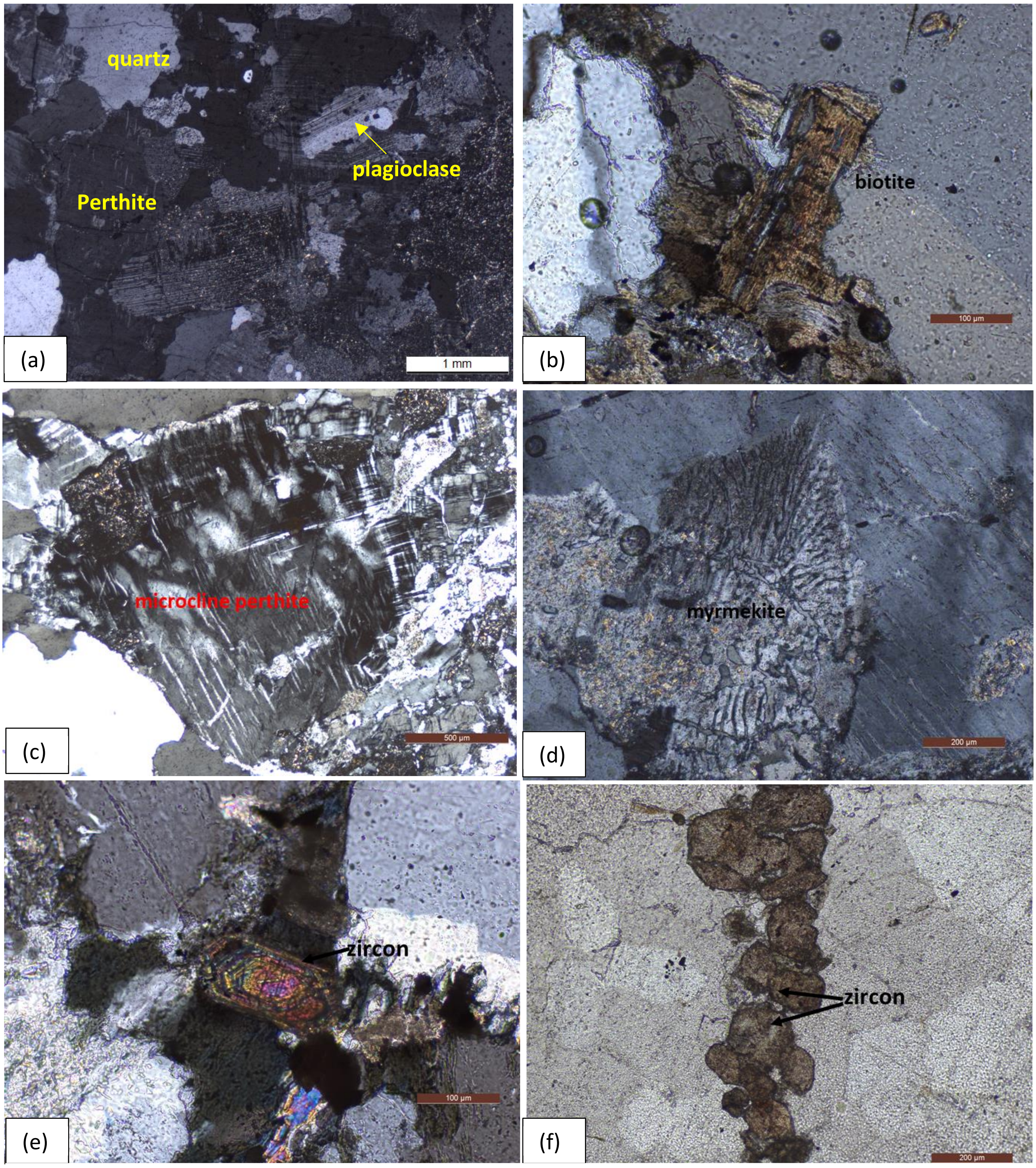

Figure. 4.2 Microphotographs of basement granite showing, (a) anhedral quartz with subhedral feldspars TL,2N (b) Typical biotite in flaky form TL,2N. (c) Microcline perthite TL,2N. (d) Quartz and feldspar intergrowth TL,2N. (e) Zoned zircon as inclusion in biotite TL,2N. (f) Zircon abundance TL,1N.

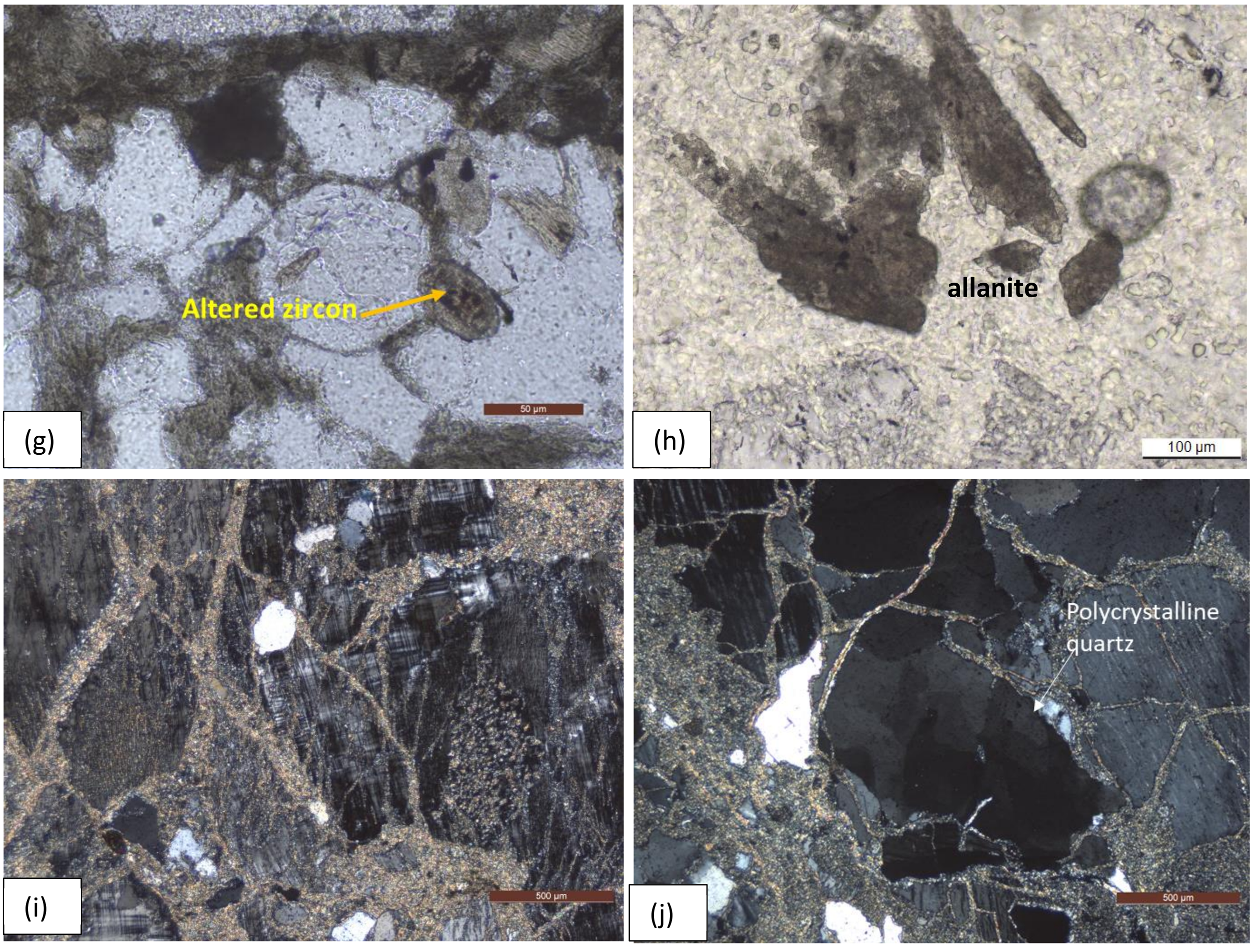

Figure 4.2 (g) Altered zircon TL,1N. (h) Altered allanite TL,1N. (i) Highly fractured quartz and alkali feldspar TL,2N. (j) Polycrystalline quartz TL,2N.

**Alteration:** Sericitization and chloritization are the dominant type of alteration observed in the basement granite of Sarangapalli area.

a) **Sericitization:** The feldspar grains mainly plagioclase is sericitized with inclusion of fine specks of white mica. Plagioclase shows variable degree of sericitisation (Figure. 4.3 a,b). The degree of sericitization is very high near the unconformity contact and dies out slowly at 3-4 m below the unconformity contact. Due to very high degree of alteration, the entire grain of plagioclase is almost converted into sericite at places (Figure 4.3b). Beside occurring as an alteration product of feldspar, sericite also occurs along the fractures (Figure. 4.3c). Hydraulic microcrack also generated as sericitization progressed and these fractures are filled with sericite (Figure. 4.3d).

b) **Chloritization:** Microscopic studies reveals two modes of occurrence of chlorite. It is occurring as thin veins along the prominent fracture planes in the country rock which is suggesting its derivation from hydrothermal solution (Figure.4.3e, f). It also seems to replace biotite in some places i.e. alteration of biotite into chlorite. Alteration is present along the periphery of biotite flakes shows gradation towards the core (Figure.4.3g, h). Presence of mafic minerals (biotite in case of Sarangapalli granite) or introduction of iron and magnesium by some secondary process may boost chloritization.

Chlorite as vein filling is very prominent in both radioactive and non-radioactive part while alteration of biotite into chlorite is commonly present in the radioactive zone and less common in non-radioactive portion.

**Ore Minerals:** Pyrite, chalcopyrite and magnetite are the main ore minerals identified from microscopic studies. Pyrite occurs as veins, anhedral crystals and euhedral clusters along the fractures in sericite matrix (Figure. 4.4a, b), is believed to formed through hydrothermal solution. Chalcopyrite also occurs as veinlets and small grains in proximity to pyrite. Magnetite abundance is very less and is closely related to alteration of biotite into chlorite (Figure.4.4c).

Uraninite and coffinite are identified as the main radioactive mineral phases present. Uraninite occurs as irregular grain has corresponding dense alpha tracks and shows variable degree of coffinitisation from the grain boundary. The uraninite partially replaced by coffinite, is intimately associated with disseminated ultrafine anhedral pyrite, later fractured along which sericite is introduced to the system (Figure. 4.4d). Coffinite occurs as both, fracture filling veins

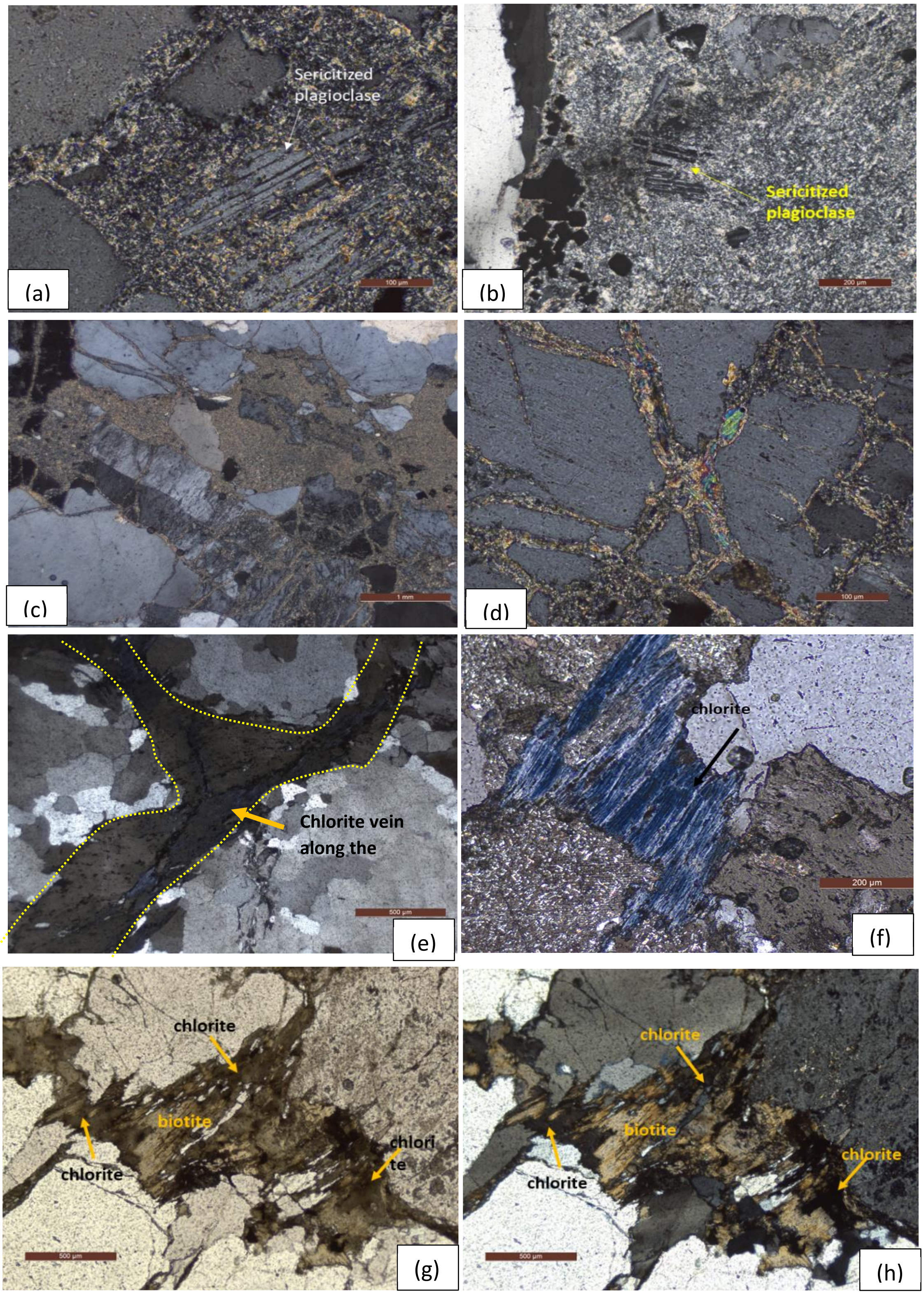

Figure 4.3 (a) & (b)Relict plagioclase grain showing higher degree of sericitization TL,2N. (c) sericite along the fractures in alkali feldspar TL,2N. (d) Hydraulic microcracks generated during progressive sericitization TL,2N. (e) & (f) Chlorite vein along the fractures TL,2N. (g) Biotite altering into chlorite TL,1N. (h) Biotite altering into chlorite TL,2N.

closely associated with disseminated pyrite (Figure. 4.4e) and as anhedral aggregates of various size associated with pyrite (Figure. 4.4f). Medium to high density alpha tracks are recorded in all type of occurrences. Coffinite is brownish grey in color and shows anisotropic transmission of light. Uraninite is distinguished from coffinite on the basis of its high track density and high reflectivity. Coffinite has possibly formed due to reaction of uraninite and silica. At places uraninite/ coffinitised uraninite is rimming the pre-existing pyrite grains can be interpreted as development of pyrite pre- crystallization of uraninite/coffinite grains.

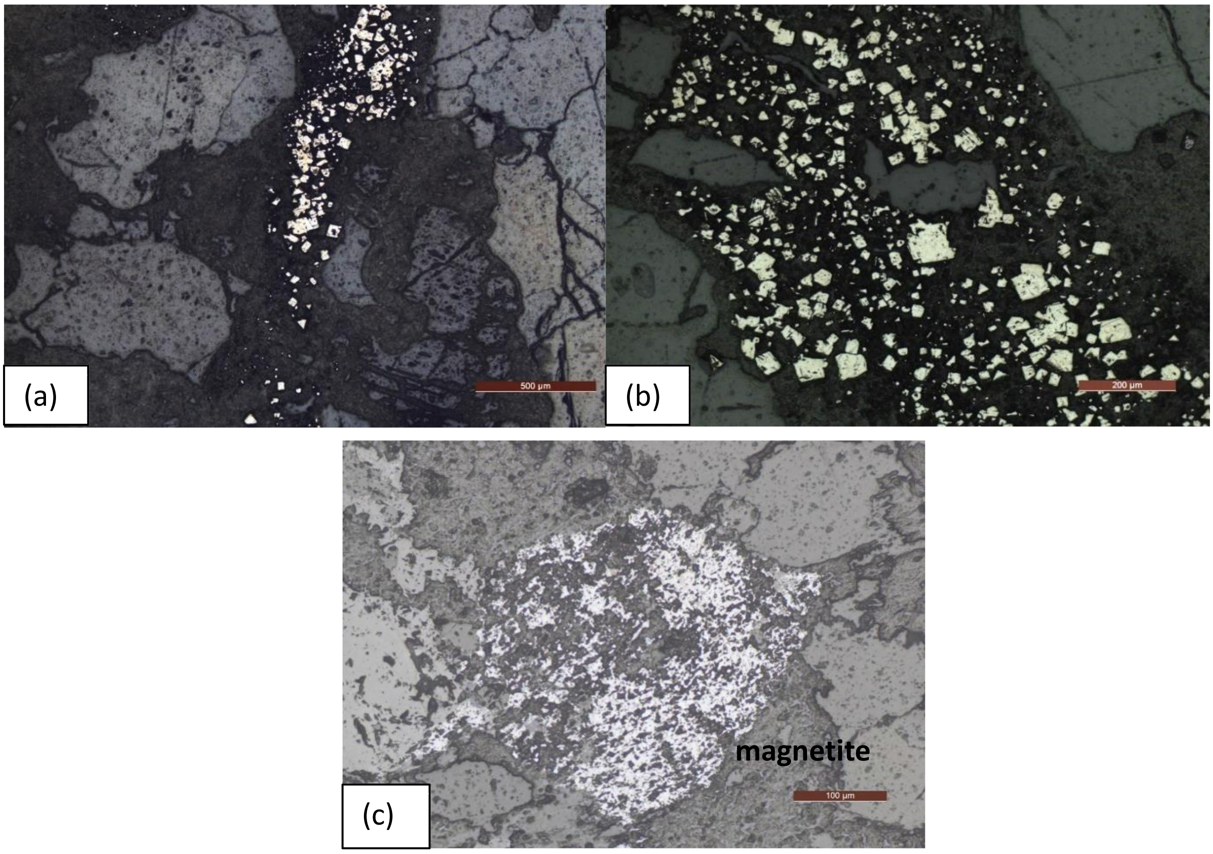

Figure 4.4 Microphotographs of basement granite showing, (a) & (b) pyrite along the fracture in sericite matrix RL,1N. (c) Subhedral magnetite RL,1N.

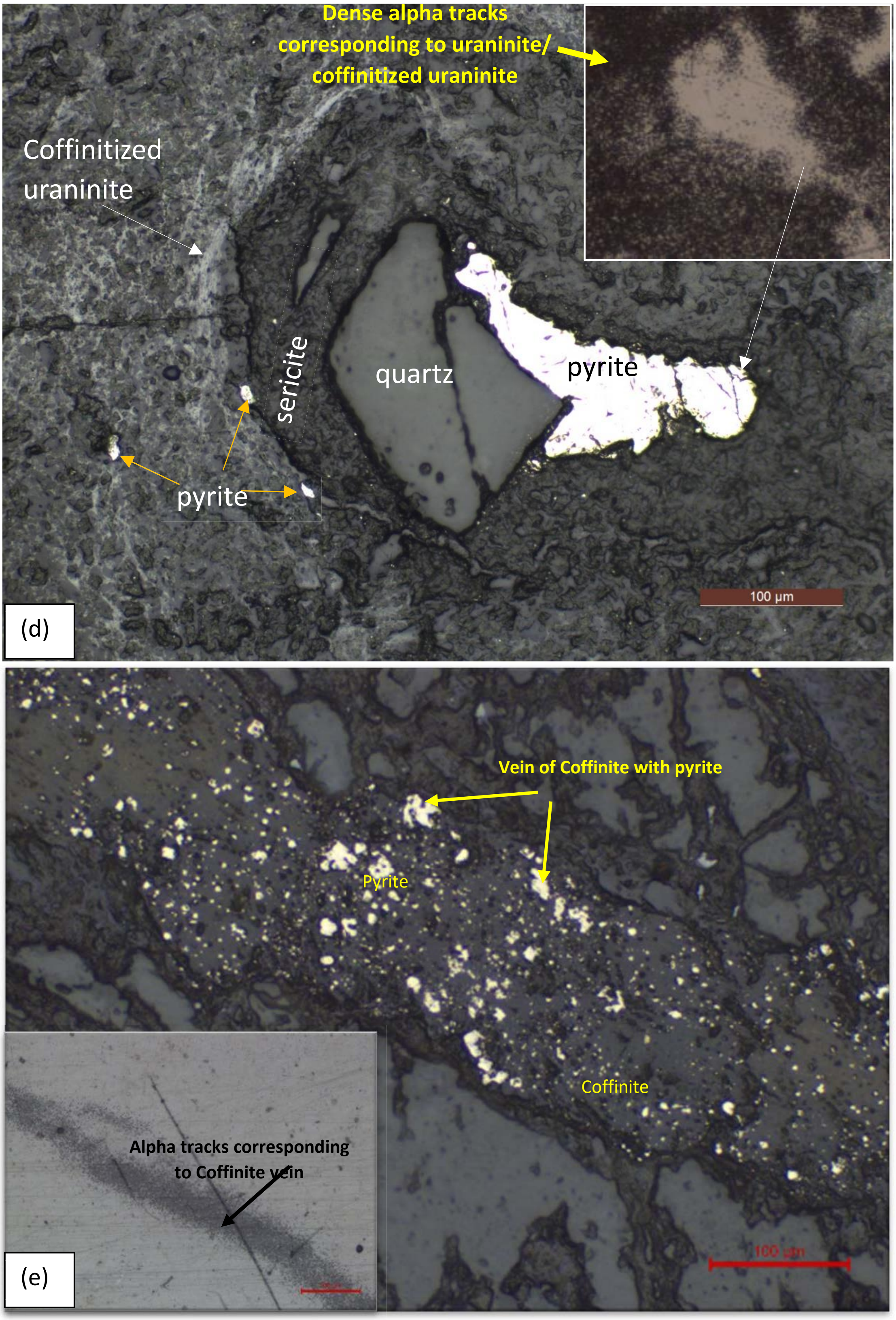

Figure. 4.4 (d) Coffinitized uraninite intimately associated with pyrite along with high density alpha tracks corresponding to coffinitized uraninite RL,1N. (e) Coffinite vein intimately associated with pyrite along with and high-density alpha tracks corresponding to Coffinite vein RL,1N.

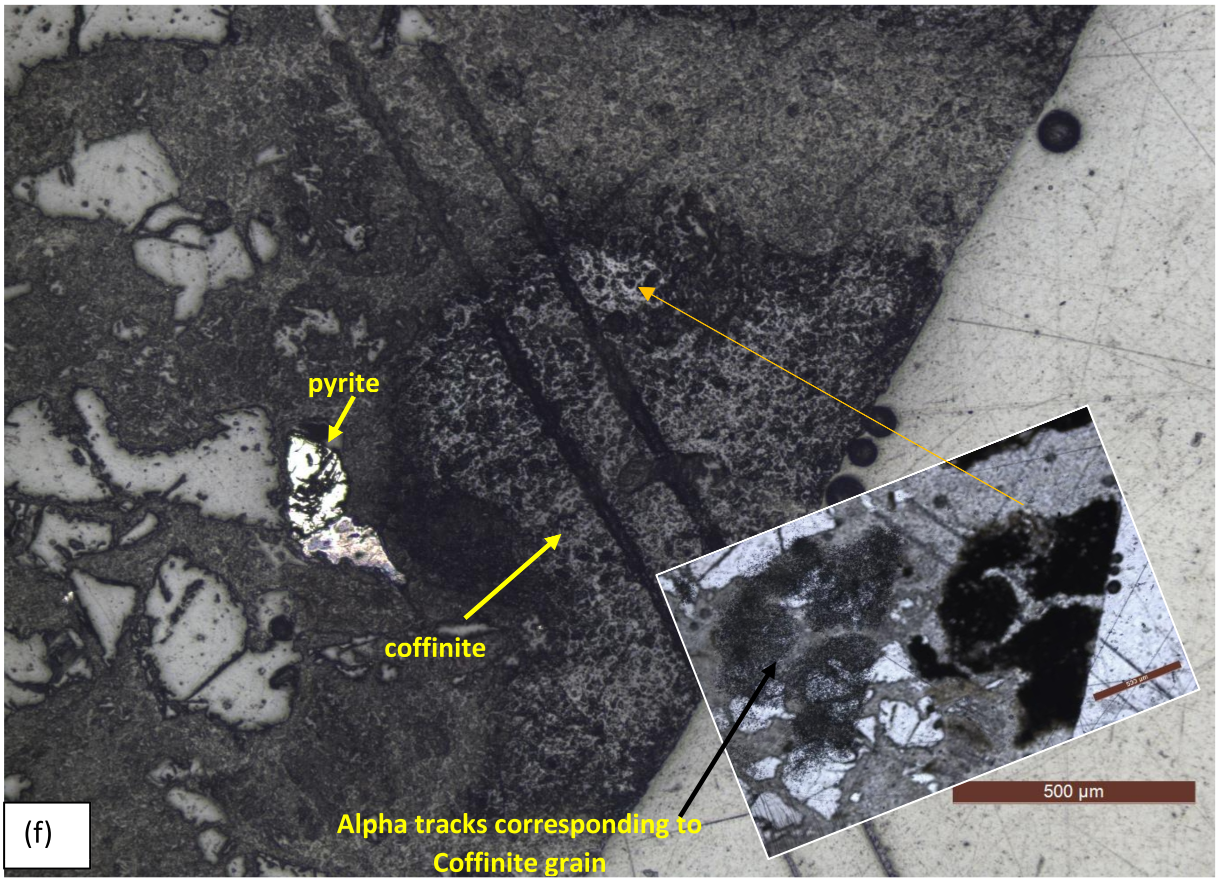

Figure. 4.4 (f) Anhedral coffinite grain adjacent to pyrite along with high density alpha tracks RL,1N.

### 4.2 Banganapalle Quartzite:

**Megascopic Description:** The Banganapalle Quartzite near the unconformity is mainly represented by conglomerate grading upward to subfeldspathic arenite to quartz arenite. Mineralization is proximal to unconformity and it is hosted by conglomerate and subfeldspathic arenite. Conglomerate occurs as ~5-20 cm thick bed represented as oligomictic matrix supported unit. This polymictic conglomerate consists subangular to sub-rounded pebbles of quartz, feldspar and quartz arenite varies from 0.5 to 2 cm in size (diameter). Major part of Banganapalle Quartzite near the unconformity is represented by subfeldspathic arenite, sometimes it is seen directly above the unconformity contact without any traces of conglomerate or pebbly horizon. Since mineralization is mainly hosted by subfeldspathic arenite unit of Banganapalle Quartzite so main focus of petromineralogical studies is on this lithic unit.

The subfeldspathic arenite is nearly 4 to 5 meter-thick and is represented as medium to coarse grained, light grey colored, hard and compact, stylolite (perpendicular to core axis) bearing massive quartzite, contains clasts of quartz and feldspars. The stylolites are perpendicular to core axis representing vertical compaction due to gravity or any other tectonic activity. Few quartz and feldspar clasts of ~0.5 cm diameter can be seen in this unit indicating its textural immaturity due to minor changes in energy condition. The core is highly altered to light dusty yellow color mineral which is identified as sericitization of feldspars in the subfeldspathic unit. Due to appreciable amount of sericitization the core is appearing dull yellow (Figure.4.5a). Subvertical fractures (at an angle $10^0$-$30^0$ from core axis) to vertical fractures can be seen at various levels. These fractures are sometimes filled with silica and pyrite veins. Radioactive mineral also observed as fracture filling veins confirmed by CN film exposures directly above the core (Figure. 4.5c). During Chromogram test radioactive phase is identified along the microfractures (Figure. 4.5d). Pyrite occurs as two modes: a) Fine grained, cubic, disseminated pyrite of diagenetic origin (Figure.4.5b); b) In the form of fracture filling vein of hydrothermal origin.

.

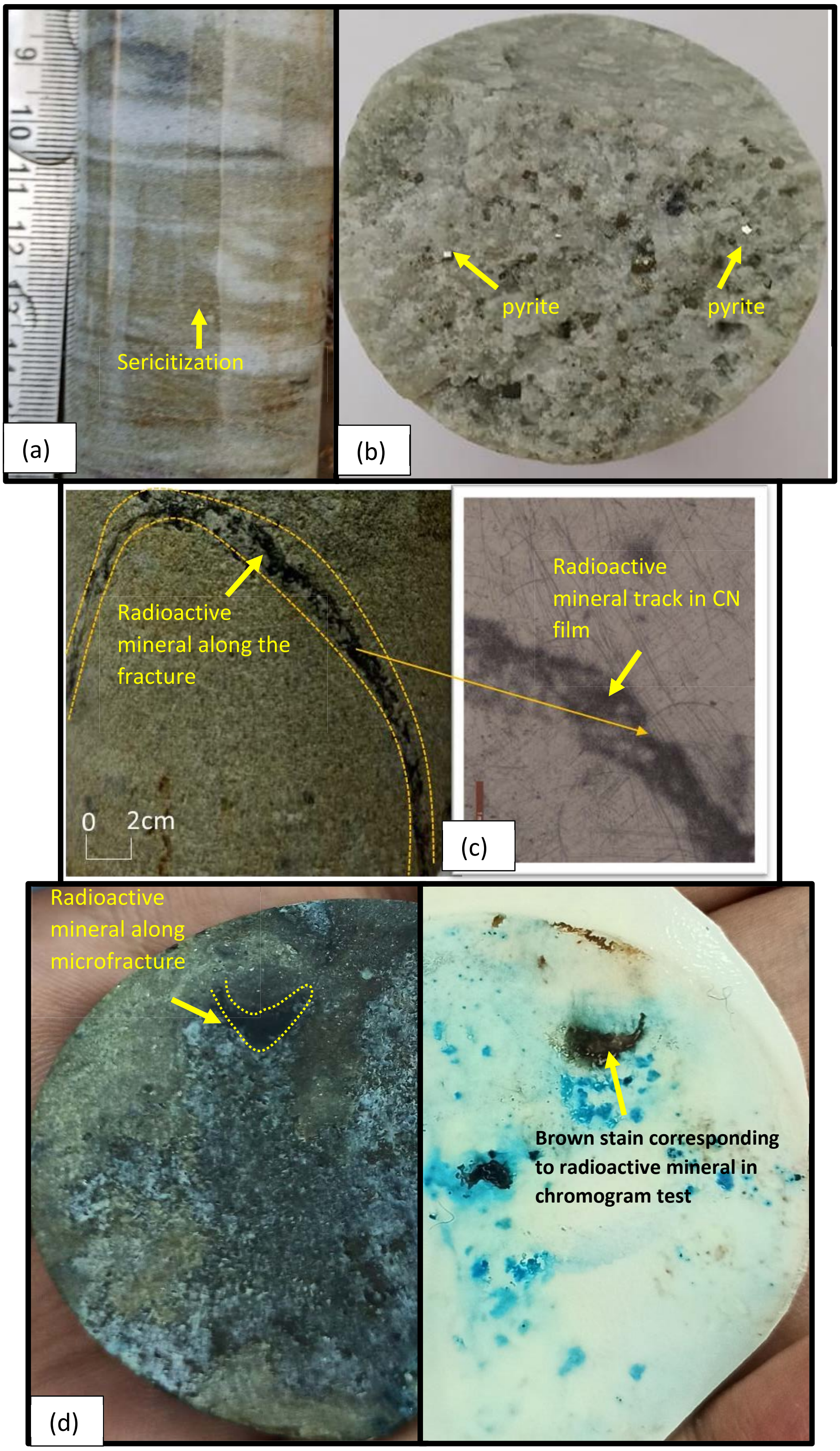

Figure. 4.5 Macroscopic photographs Banganapalle quartzite showing, (a) Sericitization as alteration product giving dull yellow coloration (b) Disseminated, cubic pyrite of diagenetic origin (c) Radioactive mineral along a subvertical to vertical fracture and its corresponding alpha tracks on CN film (d) Radioactive mineral along a microfracture giving brown strain in chromogram test.

**Microscopic Description:** It consists predominantly of quartz with subordinate plagioclase, microcline, perthite, chert, biotite, muscovite, sericite as framework minerals (Figure 4.6a-d) and zircon, tourmaline, sphene as heavy minerals. In terms of texture, it is medium to coarse grained; moderately well sorted framework minerals are largely unimodal but bimodal, finer variations are also seen. The framework consists of clasts of monocrystalline and polycrystalline quartz. A few lithic fragments of quartzite (Figure. 4.6e) and granite (Figure. 4.6f) are seen signifying the presence of granite and quartzite in the provenance. Secondary silica overgrowth (Figure. 4.6g) in optical continuity with quartz clasts suggesting siliceous cement. Sericite/clay occupying the matrix (Figure. 4.6h). Detrital zircon is corroded from the boundary showing its partial erosion during transportation (Figure. 4.6i). Irregular to sutured grain contact of framework quartz at places indicating the compaction processes the rock has undergone during diagenesis (Figure. 4.6j). The grain size of framework mineral varies from 0.15mm to 1.45mm with average 0.58 mm (n=300). The grains are subrounded to well-rounded in nature. This mineralised siliciclastic rock exhibits major quartz clast-supported texture (feldspar 12-30%), siliceous cement, sericite/clay matrix and negligible lithic fragments hence named as subfeldspathic arenite.

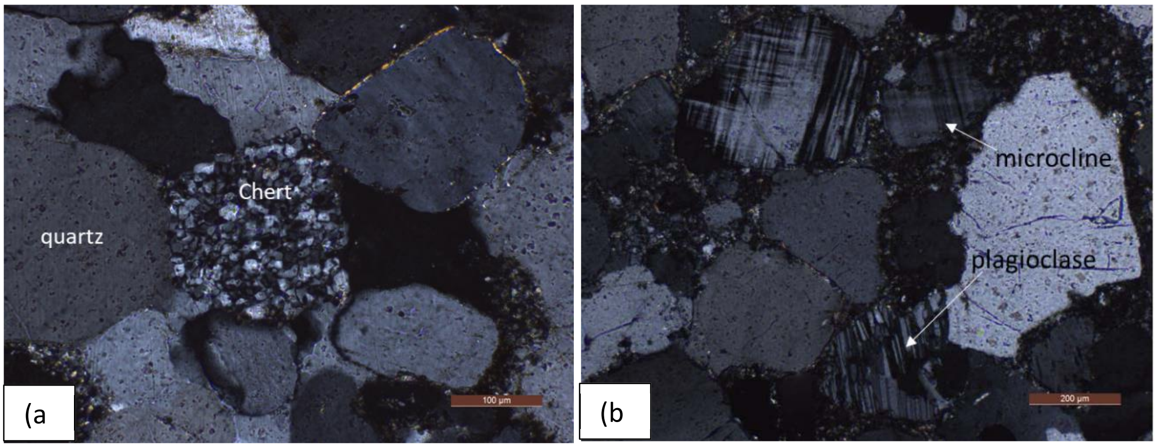

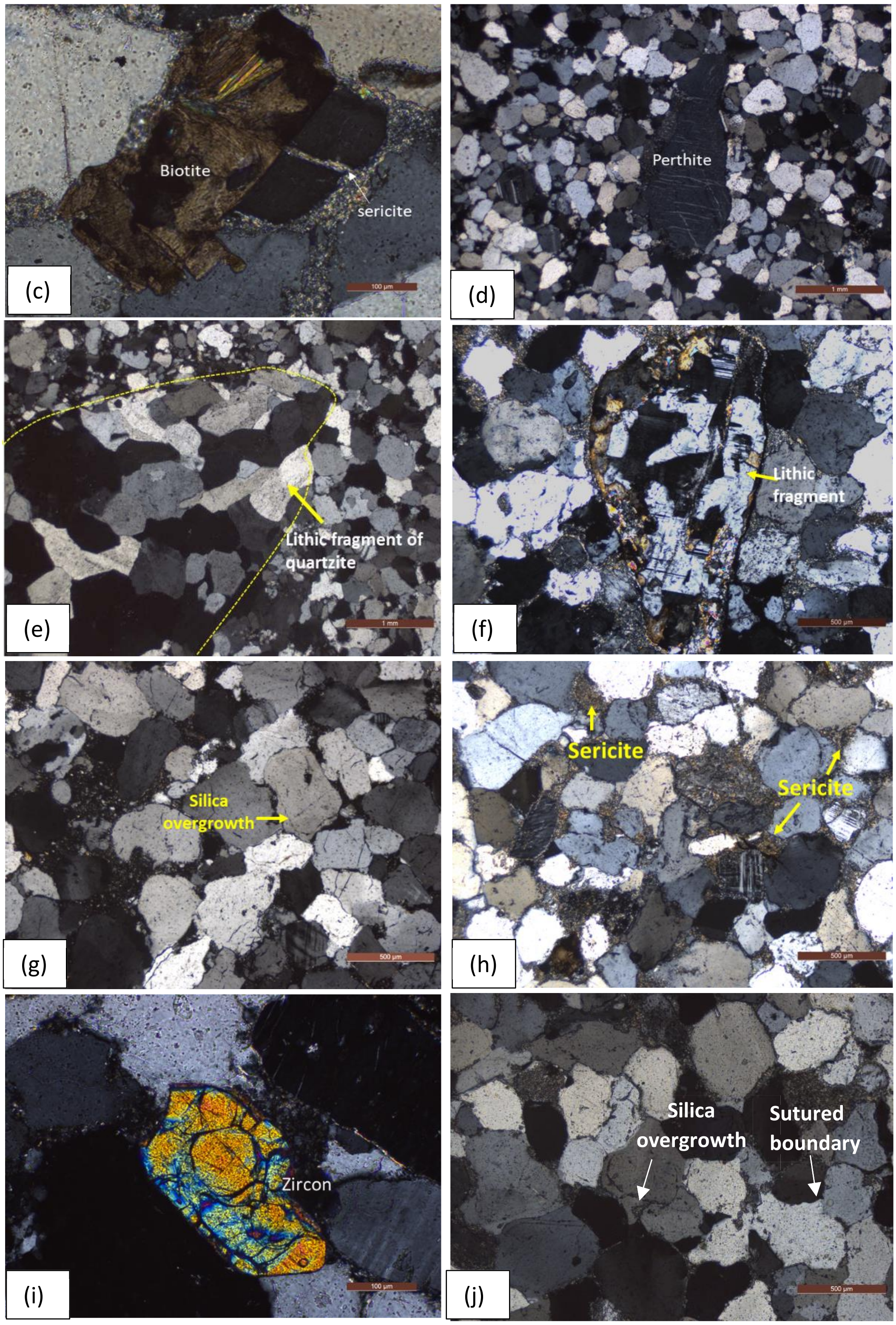

Figure. 4.6 Microphotographs of Banganapalle quartzite showing, (a), (b), (c) & (d) Showing framework minerals TL,2N. (e) Lithic fragment of quartzite TL,2N. (f) Lithic fragment of granite TL,2N. (g) Silica overgrowth in optical continuity with quartz clast TL,2N. (h) Sericite occupying the matrix TL, 2N. (i) Detrital zircon partially eroded during transportation TL,2N. (j) Sutured boundaries of quartz showing compaction during diagenesis TL,2N.

**Deformation:** It is highly fractured indicating brittle deformation in the area. The intensity of fractures is more in samples containing radioactive minerals (Figure.4.7a) however not all the mineralization occurs along the fracture, some is along the grain boundary or weak planes in rock. Individual grains are fractured to various degree and these fractures are filled with sericite (Figure.4.7b&c). Undulated appearance of muscovite also showing the effect of deformation / compression (Figure.4.7d).

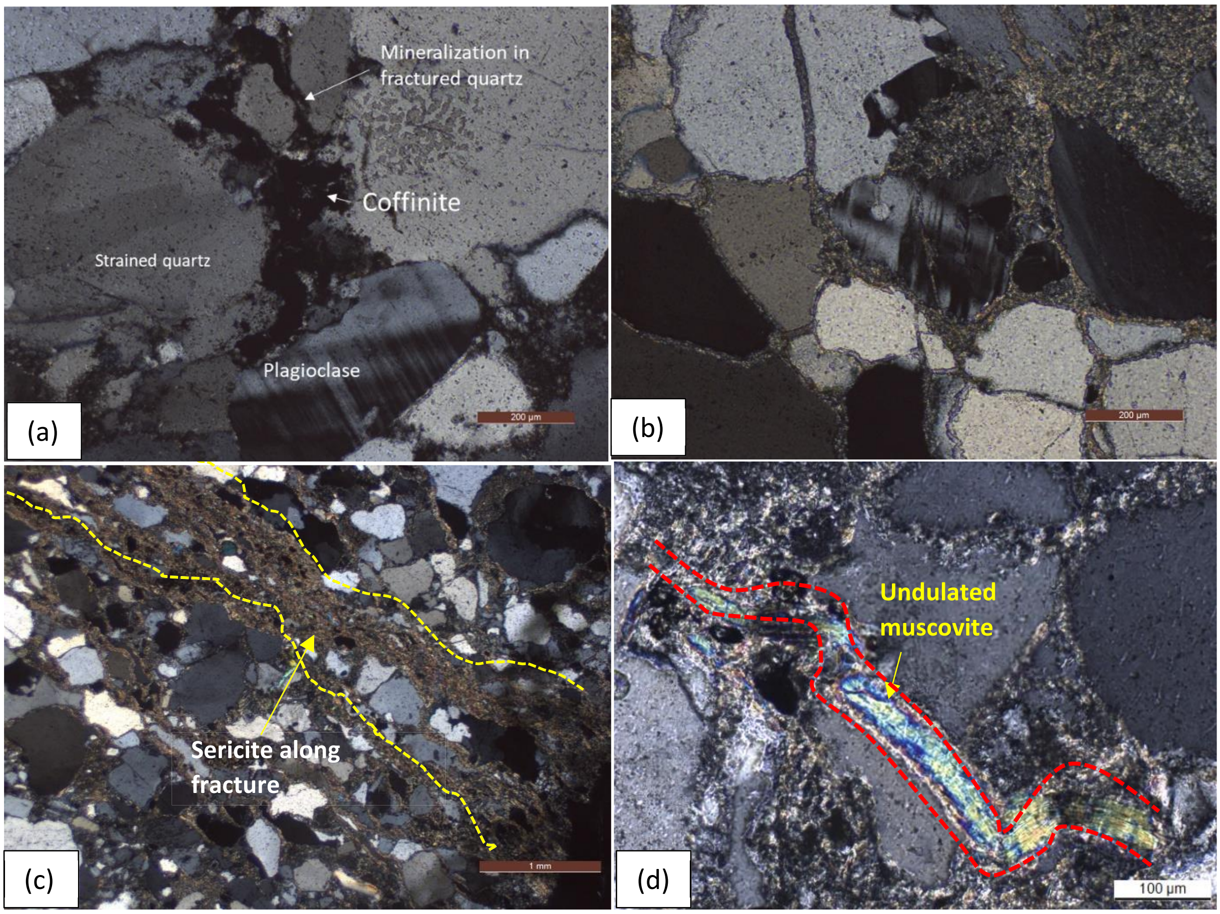

Figure. 4.7 Microphotographs of Banganapalle quartzite showing, (a) fracture quartz and mineralization (opaque) along the fracture TL,2N. (b) fractured quartz and feldspar grains occupied by sericite TL,2N. (c) Sericite along the fracture TL,2N. & (d) Undulated muscovite showing compression TL,2N.

**Alteration:** Dominantly sericitization along with minor chloritization are alteration present in Banganapalle Quartzite.

a) **Sericitization:** The plagioclase is sericitized with inclusion of fine specks of white mica (Figure. 4.8a). The degree of sericitization is very high near the unconformity contact and dies out slowly at 3-4 m above the unconformity contact. Sericite is also occupying the fractures of upto 1mm thickness (Figure. 4.8a). Along these fractures, quartz clasts are seen corroded from the grain boundary near the contact of sericite due to interaction with hydrothermal solution (Figure. 4.8b).

b) **Chloritization:** As basement granite, replacement of biotite with chlorite from the grain boundary (Figure. 4.8c) and Chlorite occupying the interstices of framework mineral in Banganapalle quartzite is noted (Figure. 4.8d). The uranium mineralization is associated with chloritized biotite / chlorite at some places.

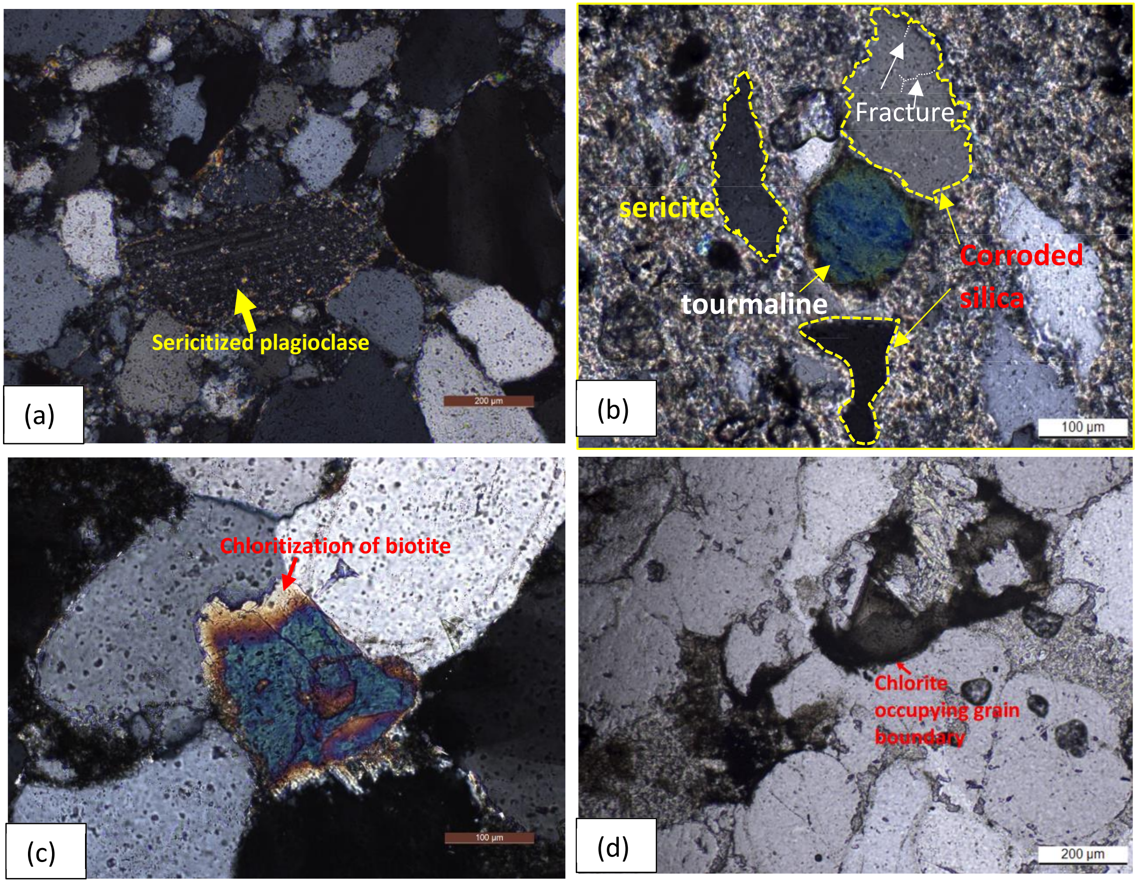

Figure. 4.8 Microphotographs of Banganapalle quartzite showing, (a) Sericitization of plagioclase TL,2N. (b) Corroded boundaries of quartz clasts in sericite matrix along the fracture TL,2N. (c) Replacement of biotite by chlorite from grain boundary TL,2N. & (d) Chlorite along the interstitial spaces of grain boundary TL,1N.

**Ore Minerals:** Pyrite and coffinite are the dominant ore minerals seen under thin section studies. Pyrite occurring as; 1-Disseminated euhedral crystals (perfectly cubic) of diagenetic origin (Figure. 4.9a), 2- Colloform pyrite (>50-micron size) (Figure. 4.9b, c), 3- In the form of fracture filling veins associated with coffinite suggesting its hydrothermal origin (Figure. 4.9d).

Coffinite is seen occupying the weak planes and along intergranular spaces of the framework minerals or fractures generated due to brittle deformation in the area, suggesting its epigenetic origin. Coffinite is translucent under transmitted plane polarized light, has near similar reflectivity to surrounding quartz grains and corresponding alpha-tracks are moderately high. Coffinite outlining the grain boundary of framework quartz and feldspar is seen intimately associated with ultrafine pyrite (Figure. 4.10a, b & Figure.4.11a). It is also occurring along the fractures of framework mineral (Figure. 4.11b&c). It is also seen associated with chlorite (Figure. 4.11d&e). At one place a coffinite vein is seen associated with diagenetic pyrite, hydrothermal pyrite vein and chlorite (Figure. 4.12a, b).

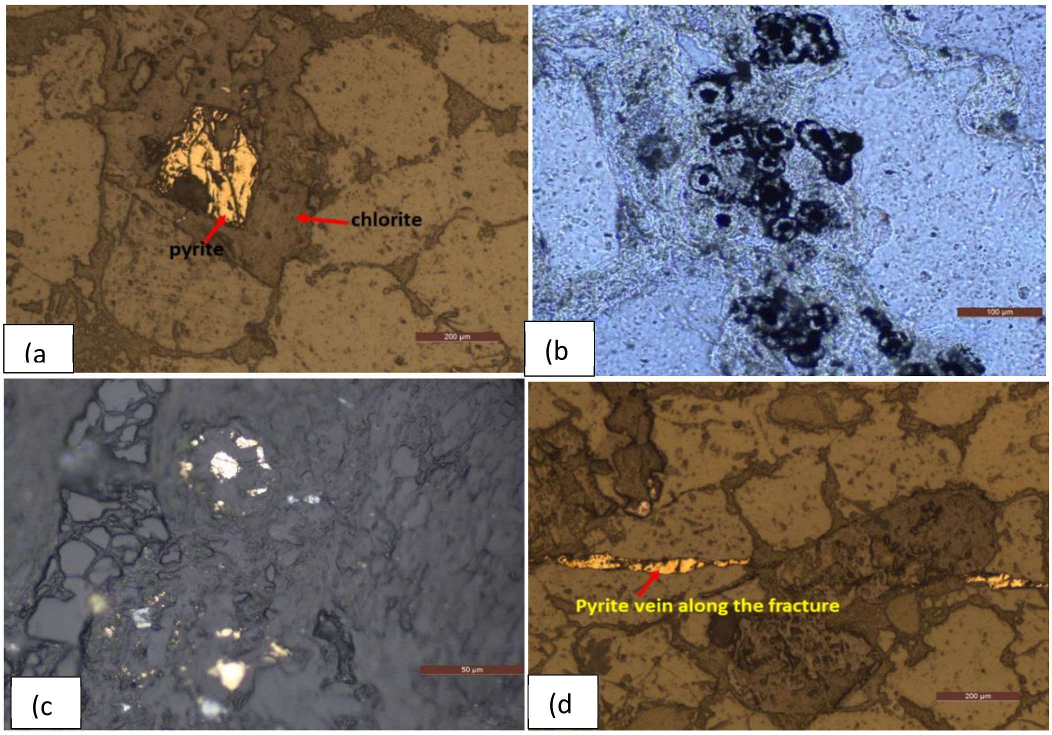

Figure. 4.9 Microphotographs of Banganapalle quartzite showing, (a) fractured euhedral pyrite RL,1N. (b) Colloform pyrite TL,1N. (c) Colloform pyrite RL,1N. & (d) Pyrite vein along the fracture RL,1N.

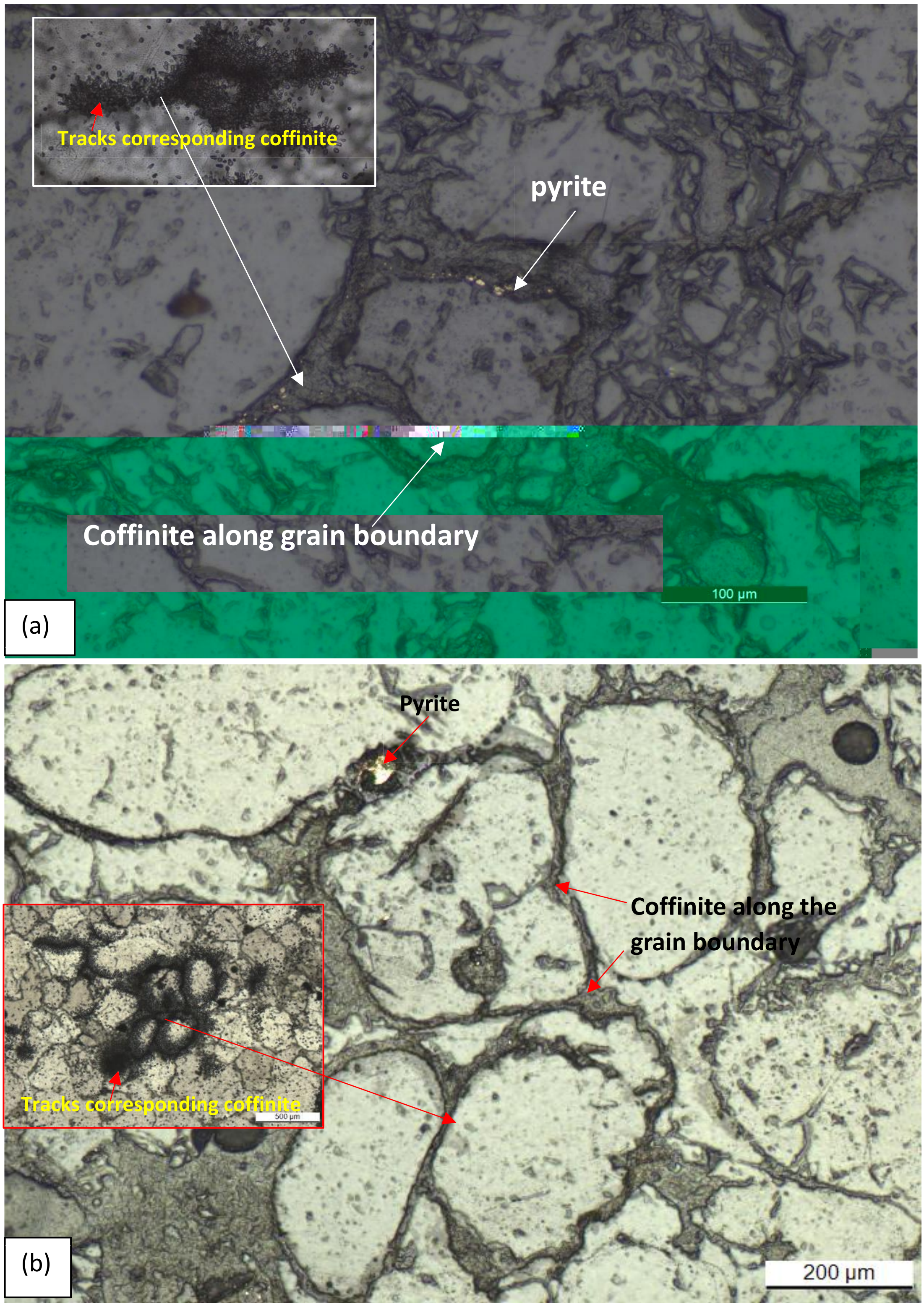

Figure. 4.10 Microphotographs of Banganapalle quartzite showing, (a)&(b) Coffinite associated with ultrafine pyrite RL,1N.

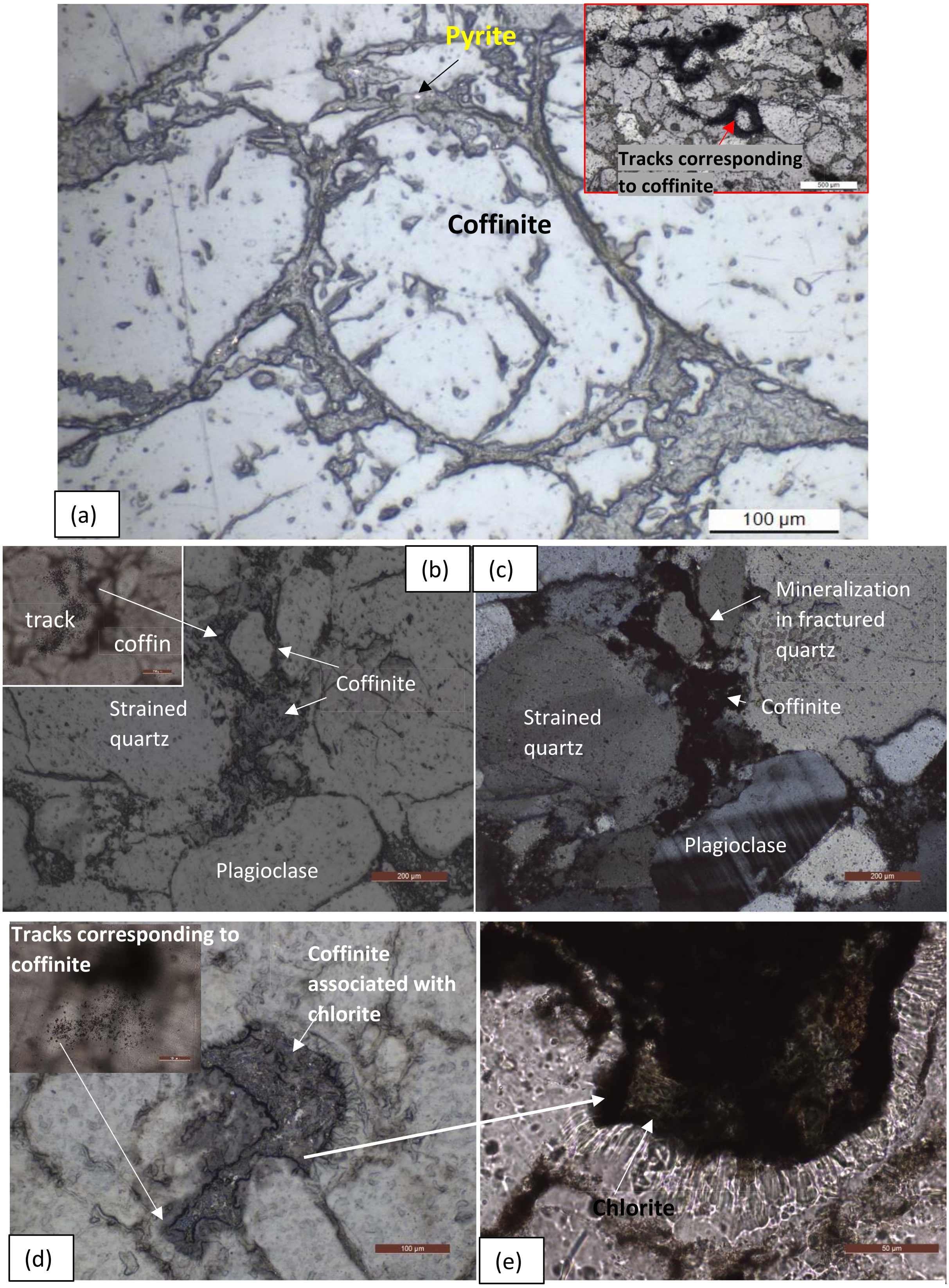

Figure. 4.11 Microphotographs of Banganapalle quartzite showing, (a) Coffinite outlining the grain boundary associated with ultrafine pyrite. (b) & (c) Coffinite along the along the fracture, RL,1N & TL,2N respectively. Coffinite associated with chlorite, (d) RL,1N & (e) TL,2N.

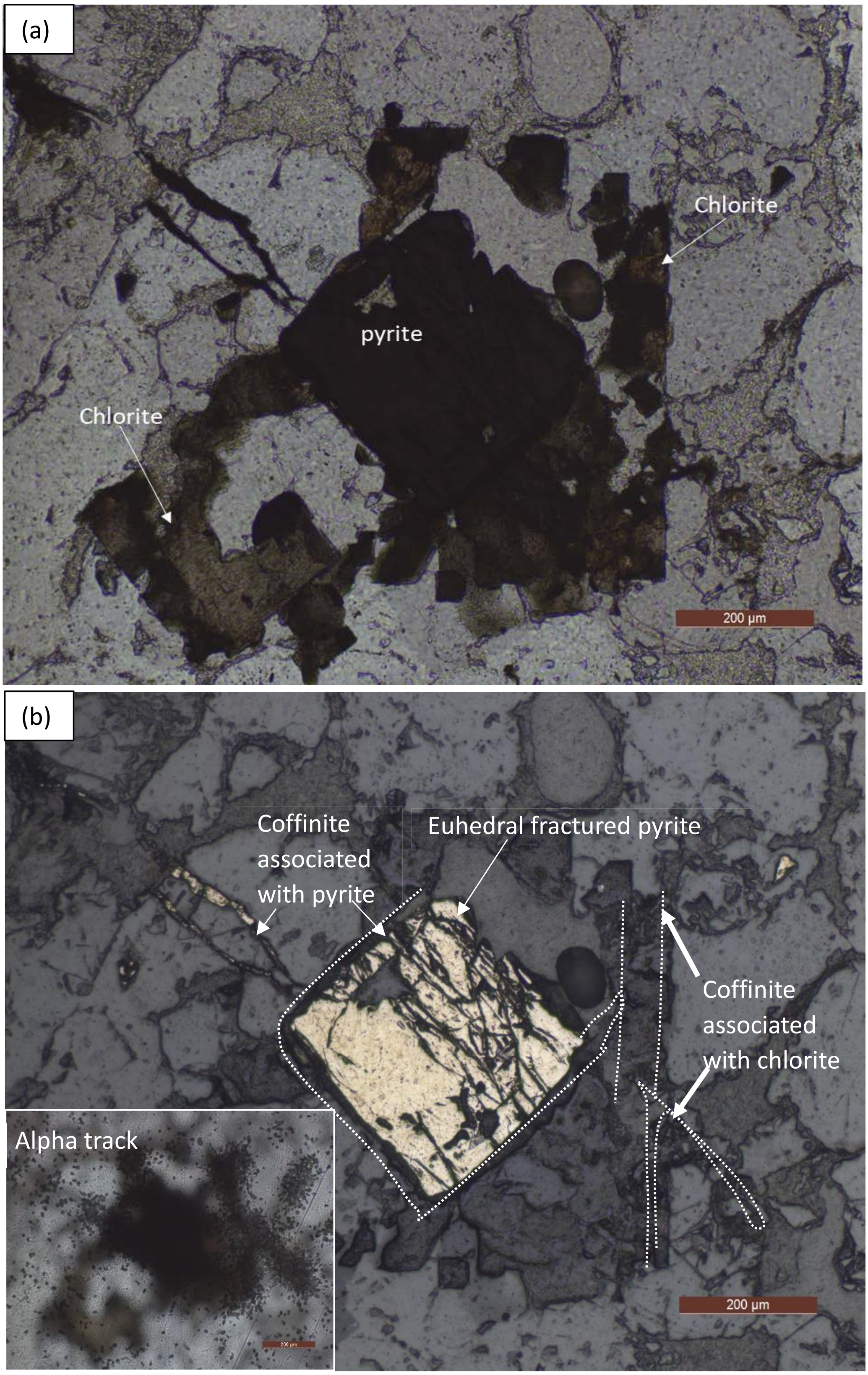

Figure. 4.12 Microphotographs of Banganapalle quartzite showing, (a) Chlorite associated with pyrite (opaque) TL,1N &(b) Coffinite rimming pyrite crystal along associated with pyrite along the vein and associated with chlorite along the fractures

## 4.3 ALTERATION FEATURES:

Hydrothermal alteration is a process which involves mineralogical, textural and chemical changes resulting from interaction of hot aqueous fluids with the rocks through which they pass under evolving physico-chemical conditions (Pirajno1992).

To characterize different types of alterations, present in the study area, surface and subsurface samples have been studied. A total of two types of alteration have been identified through petrographic study as well as megascopic study of cores. Following two types of alterations has been observed.

1) Chloritisation

2) Sericitisation

### 4.3.1 Chloritisation

It is a transformation accompanied by crystallization of secondary chlorite group minerals at the expense of other, mainly mafic minerals (biotite in case of Sarangapalli area). From thin section studies, it has been observed that chlorite is of two types on the basis of its mode of occurrence, as mentioned below:

1) Chlorite present as vein/veinlets, form random network and occur as fine mass occupying intergranular spaces (In both the studied rocks, basement granite and Banganapalle Quartzite).

2) Chlorite formed by alteration of biotite and occurring in patches as pseudomorph flakes (In both the studied rocks, basement granite and Banganapalle Quartzite).

Coffinite also shows association with chlorite in Banganapalle quartzite (subfeldspathic arenite).

### 4.3.2 Sericitisation

Sericite is fine grained mica, produced by alteration of feldspar. Sericitic alteration is due to destabilisation of feldspar in the presence of H+, OH-, K & S to form quartz, white mica, pyrite and some chalcopyrite (Pirajno, 1992). In this process Na, K, Ti, Fe and Mg are leached out.

Basic equation for the single reaction of sericite formation is as follows:

$$3KAlSi_3O_8 + 2H^+ = KA_{l3}Si_3O_{10}(OH)_2 + 6SiO_2 + 2K^+$$ (Korzhinskiy, 1980)

Sericitisation of feldspars is present in majority of the samples. The feldspar grains are sericitized with inclusion of fine specks of white mica. Plagioclase shows variable degree of sericitisation which is very high near the unconformity contact and dies out slowly at 3-4 m above and below it. Due to very high degree of alteration, in some cases, entire plagioclase grain has been sericitised leaving behind the sericite matrix. Besides occurring as alteration product of feldspar, sericite also occurs along the fractures which could have been formed by alteration of pulverized quartz-feldspar grains generated due to brittle deformation in the area.

# CHAPTER-5

# XRD ANALYSIS

X-ray diffraction technique is most widely used for the identification of unknown crystalline materials (e.g. **minerals**, inorganic compounds). XRD analysis carried out to identify the mineral phases which can not be identified under petromineralogical studies e.g., secondary uraniferous phases (if any).

**Sample description**

Four representative mineralized core samples of Basement granite (n=2) and Banganapalle quartzite (n=2) were set for X-ray diffraction studies at XRD laboratory, AMD, Hyderabad X-ray diffraction studies.

**Method of investigation**

Radioactive sample were first examined under the ultraviolet lamp. Fluorescent minerals at place were scrapped with the help of knife/blade. Subsequentially the radioactive sample were crushed to minus 80 mesh. These were then taken up for sequentially heavy liquid separation using bromoform (specific gravity, SG 2.88), methylene iodide (SG, 3.31), and Clerici solution (SG, 4.20). The Clerici heavy (CH) fraction were further subjected to the magnetic separation using a Frantz isodynamic magnetic separator at different amperes.

The X ray diffraction (XRD) study was carried out in a Siemens D-500 diffractometer. The accelerating voltage was maintained at 35 kV and the tube current at 20mA. CuKα radiation (1.5418Å), monochromatized using curved graphite monochromatized, was used for diffraction. For identification, a scanning speed of 0.03-degree 2θ/second, over a long angular range (4-90degree 2θ), with a sampling time of 2 second was selected. The respective 2θ value of the reflection and the value of their interplanar spacing were obtained directly by using

Wassermann ADM software. Mineral identification was done from the powder diffraction data so obtained by comparing the same with the international center for Diffraction Data card. And the crystallographic parameter, viz., unit cell dimension ($a_o$) and the unit cell volume (V), of uraninite ($UO_2$) were determined. From the unit cell dimension ($a_o$), the stoichiometric deviation of the oxygen content (x) in the formula unit (OCIFU) of uraninite ($UO_{2+x}$), was also calculated.

## 5.1 ANALYTICAL RESULS AND INTERPRATATION

The following results are obtained from XRD studies (also tabulated in Table 5.1):

**Rock forming mineral**: Biotite, muscovite, quartz, microcline, albite and chlorite are the major rock forming phases identified which is substantiated with petromineralogical studies. Chlorite is hydrothermally derived to the system and also as alteration product of biotite as indicated by petromineralogical studies.

**Rare-Earth Bearing Minerals:** Monazite and zircon are REE bearing minerals occur in Banganapalle quartzite.

**Uranium bearing minerals**: Uraninite and coffinite are the primary uranium phases, were identified through XRD.

**Ore mineral:** Other than radioactive phases (uraninite and coffinite) pyrite, pyrrhotite, hematite and galena are the ore phases identified.

**Mineralogical Crystallography:** The unit cell dimension ($a_0$) of the investigated uraninite is: $a_0$ (Å)= 5.4221±0.0010, and V (Å$^3$) =159.40 with $UO_{2.44}$ ($FUO_2$). It is also apparent that with increasing in oxidation grade, there is a concomitant decrease in unit cell dimension and formational temperature. Fritsche and Dahlkamp, 2001 proposed a plot on the basis of unit cell parameter ($a_{0,}$ Å) of uraninite and oxidation grade to infer the source of uraninite by examining uranium oxides from pegmatitic, metamorphic and metasomatic uranium occurrences with the objective to check for differences in their physico-chemical properties and, to be applied as an exploration tool. The plot suggests its derivation from granite related (hydrothermal) vein type mineralization (Figure.5.1).

**Temperature -oxidation grade-unit-cell**: The unit-cell dimension appears to be a function of formational temperature i.e. the higher the temperature the larger the $a_o$ and the lower the oxidation grade. The Uraninite shows broad and low intensity reflection. The unit cell parameter and the high non-stoichmetry indicates a low temperature origin.

**Table 5.1 XRD result of radioactive samples from Sarangapalli area**

| **Sl. No.** | **Sample No.** | **Lithounit** | **Atomic minerals** | **Other ore minerals** | **Rock forming minerals** |
|---|---|---|---|---|---|
| 1. | BH/19-/120.88 | Granite | Coffinite and rutile.<br>Unit cell parameter of coffinite is $a_0$ = 6.9639 ± 0.0079 Å, $c_0$ = 6.2504 ± 0.0248 Å and V = 303.129 $Å^3$. | Pyrite, Hematite and Galena. | Chlorite, quartz, albite, biotite, muscovite and microcline. |
| 2. | BH 26-B1/23 | Granite | Uraninite, coffinite and rutile.<br>Unit cell parameter of coffinite is $a_0$ = 6.9538 ± 0.0026 Å, $c_0$ = 6.2548 ± 0.0023 Å and V = 302.45 $Å^3$.<br>Unit cell parameter of uraninite is $a_0$ = 5.4221 ± 0.0010 Å and V = 159.40 $Å^3$ Oxygen in FU = $UO_{2.44}$. | Galena. | Quartz, chlorite, albite and microcline. |
| 3. | BH/12-/189.41 | Banganapalle Quartzite | Monazite, rutile and zircon. | Pyrite and pyrrhotite. | Biotite, quartz and accessory albite |
| 4. | BH/21-/154.41 | Banganapalle Quartzite | Rutile and zircon. | Pyrite and galena. | Quartz, biotite, chlorite and microcline. |

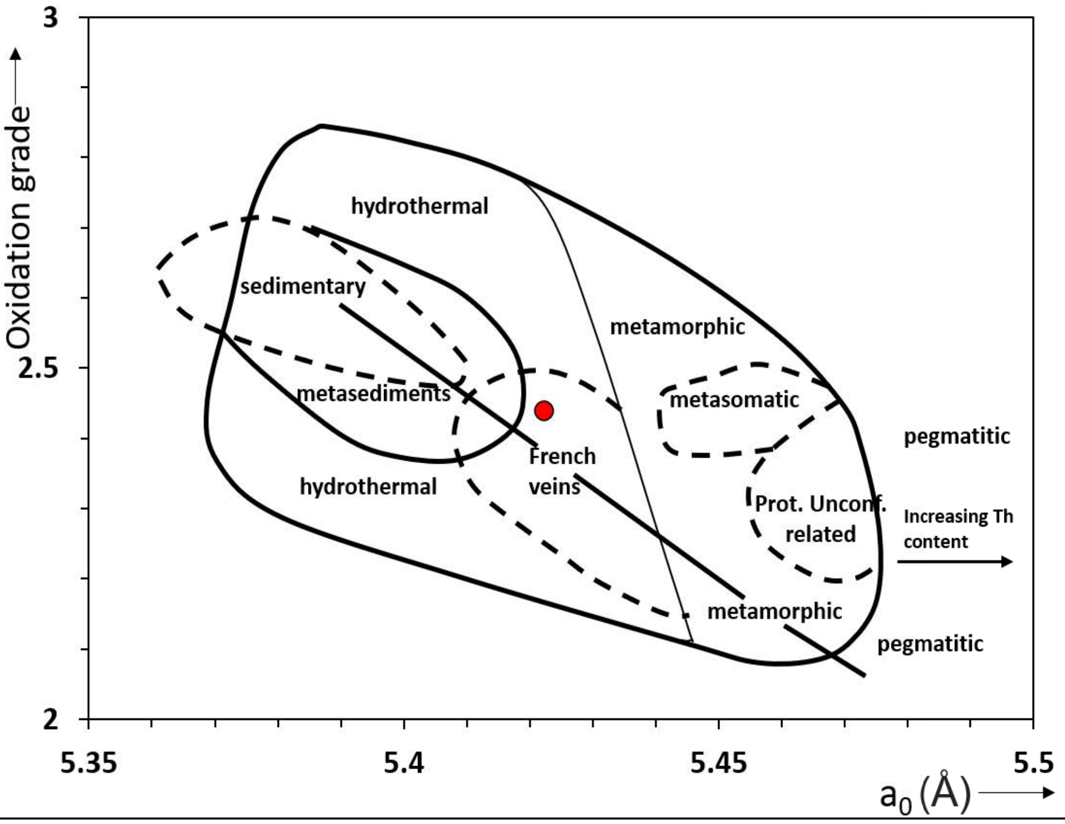

Figure 5.1 Oxidation grade versus unit-cell dimension for uranium oxides, and their attribution to genetic fields; hydrothermal = vein type, french veins = granite related vein-type mineralization (after Fritsche and Dahlkamp, 2001).

# CHAPTER 6

# MINERAL CHEMISTRY

Mineral chemistry of selected minerals (radioactive, sulphides and some silicates) of host rock for uranium mineralization has been carried out after petromineralogical studies for understanding of geochemical processes responsible for mineralisation and its relationship with other ore and gangue minerals in Sarangapalli area. Electron Probe Micro Analyser (EPMA) Model 'Cameca SX-100' has been used for analysis. EPMA is a fully qualitative and quantitative method of non-destructive elemental analysis of micron-sized volumes at the surface of materials, with sensitivity at the level of ppm. It is the most precise and accurate micro-analysis technique available and all elements from B to U and above can be analysed. This instrument is equipped with a complete kit of built-in microscopy tools that allow simultaneous X-ray (WDS), SEM and BSE imaging, plus sophisticated visible light optics; they provide very flexible sample inspection with image magnification ranging from 40 to 400,000 µm.

## 6.1 COFFINITIZED URANINITE

### Rock type: granite

Coffinitized uraninite (~60 micron) surrounded by coffinite is observed rimming the sericitic mass (Figure.6.1a). This situation suggesting coffinitization of pre-existing uraninite grain from its margin. Coffinitization in uranium deposits occurs through dissolution of $UO_2$ (often forming hexavalent uranium intermediates) followed by reaction with silica-rich fluids in reducing environment (Guo et al., 2015). Coffinitization is indicating relatively reduced and silica rich, low temperature and pressure environment in the system (Wang and Xu,1999, Min et al., 2005, Yuan et al., 2019). The analysis of such grains (n=3) indicates very high $UO_2$ (79.33 - 80.70 wt%; avg. 80.03 wt%), high CaO (3.09 - 3.27 wt%; avg. 3.18 wt%), moderate

$SiO_2$ (6.12 - 8.42 wt%; avg. 7.09 wt%), $RE_2O_3$ (2.70 - 3.37 wt%; avg. 3.03 wt%), FeO (1.23 - 1.41 wt%; 1.31 wt%). The grains contain variable and low PbO (0.47 - 1.49 wt%) and negligible $ThO_2$ (<0.01 - 0.09 wt%). Mineral chemistry of coffinitized uraninite is given in table 6.2. Since coffinitized uraninite is rimming sericite indicating sericitization prior to coffinitized uranite.

## 6.2 COFFINITE:

### Rock Type: Granite

Coffinite as anhedral aggregates along the weak plane (fractures) is associated with barite, Ba-Al silicate, pyrite and galena. Pb-S complex and galena is observed in the margin of coffinite which may be indicating radiogenic Pb derived galena. Mineral chemistry of coffinite indicates variable and high $UO_2$ (55.09 - 75.25; Avg. 64.26 wt%), $RE_2O_3$ (2.04 - 6.64 wt%; Avg. 4.90 wt%), CaO (1.02 - 2.69 wt%) with highly variable $Y_2O_3$ (<0.01 - 4.35) and $Al_2O_3$ (0.51 - 4.35 wt%). $SiO_2$ is present in coffinite in variable degree, ranging from 9.28 - 26.69 wt%. The amount of Th in the samples studied is either very low or below the detection limit of EPMA. Further, these grains show widely varied $ZrO_2$ (<0.01 - 2.25 wt%), with very negligible to low PbO (<0.01 - 0.82wt%). It is found that $SiO_2$ shows negative correlation with $UO_2$ in the studied coffinite grains (Figure. 6.2). The coffinite grains analysed very low PbO indicates its loss and degree of alteration. As Pb has a different valence and ionic radius than U, Pb would tend to leave the uraninite crystal structure during alteration events and will be replaced by other cations, mostly Si, Ca, and Fe (Janeczek & Ewing, 1992, Alexandre & Kyser, 2005). Pb released during coffinitization precipitates as Pb-S complex and galena (Figure. 6.1a). The analytical results are given in table 6.3.

**Textural relationship with associated minerals:** In Figure 6.1a, coffinite is fractured and this fracture is filled with sericite suggesting sericite is post-coffinite. Coffinite is partially or perfectly rimming the pyrite shows pyrite is pre-coffinite (Figure. 6.1a & 6.1d). Coffinite as a vein (40µm) along the fracture is partially rimmed by galena shows galena is post-coffinite (Figure. 6.1b). Presence of coffinite (15µm) inside the fracture within barite (Figure. 6.1c) and along the grain boundary of barite (Figure. 6.1d) shows that barite is also pre-coffinite. Similarly, pyrite rimmed by barite (Figure. 6.1) suggests its pre-barite origin. Ba-Al silicate is partially rimming barite is intimately associated with coffinite showing its post-barite and pre- to syn-coffinite origin (Figure. 6.1d).

**Rock type: Subfeldspathic arenite (Banganapalle quartzite)**

Coffinite occur along the weak planes (fractures and grain boundaries of framework minerals) is closely associated with pyrite, chlorite and sericite in sub-feldspathic arenite. Two types of contacts viz. undulated contact of quartz with coffinite (high brightness) /or U-Si-complex and even contact of coffinite with quartz clast are observed in BSE image (Figure. 6.1f). Such textural features suggest that the formation of coffinite in the studied arenite sample involved detritus quartz as well as silica rich mineralizing solution. Mineral chemistry of coffinite (n=14) indicate variable and high $UO_2$ (50.47 - 67.52 wt%), $SiO_2$ (19.31- 34.12 wt%) and $Al_2O_3$ (1.59 - 6.29 wt%) content (Table 6.4). The coffinite grains also indicate very low concentration of PbO (0.08-2.81 wt%), with moderate $RE_2O_3$ (2.53 - 5.16 wt%) and negligible $ThO_2$ (<0.01 - 0.20 wt.%). $SiO_2$ shows negative correlation with $UO_2$ in the studied coffinite grains (Figure. 6.2) similarly as coffinite in granite.

**Textural relationship with associated minerals:** Three stage of pyrite is noted; pre-, syn- and post mineralization. Pyrite is partially rimming coffinite (Figure. 6.1e&f) and indicating, its post coffinite nature. Coffinite partially encircling pyrite and also found along the fractures in pyrite shows pyrite metallogeny is pre to coffinite mineralization (Figure. 6.1f). Pyrite vein along with coffinite shows their syngenetic origin (Figure. 6.1g). Occurrence of coffinite along the grain boundary and inside the fractures of chlorite suggesting chloritization prior to formation of coffinite (Figure. 6.1g&h). Sericite is rimming coffinite and also found along the fracture in pyrite suggesting its post coffinite origin (Figure. 6.1f).

## 6.3 PYRITE:

### Rock Type: Granite

Six points were analysed in three grains (100-200µm) of pyrite in altered granite. BSE image of the grains (Figure. 6.1a&d) shows compositional homogeneity, that is in turn reflected in the data (Table-6.5) indicating restricted compositional variation of Fe (45.42 - 46.39 wt.%; Avg. 45.82 wt.%) and S (52.03 - 52.64 wt.%; Avg. 52.36 wt.%). Pyrite is associated with coffinite, baryte and sericite.

### Rock Type: Subfeldspathic arenite

Pyrite was also observed in subfeldspathic arenite as discrete grains and associated with coffinite, chlorite and sericite. The grains (150 - 220 µm) vary in shape from irregular to cubic, besides this it also occurs as fracture filling vein (Figure. 6.1f & g). Analytical data of 7 points analysed in three grains indicated Fe (44.39 - 46.95 wt.%; Avg. 45.68 wt.%) and S (50.64 - 53.48 wt.%; Avg. 52.52 wt.%). Analytical data is given in the Table-6.6.

## 6.4 GALENA

### Rock Type: Altered granite

Galena is found in association with coffinite (Figure. 6.1b & i). Mineral composition of one grain of galena (125µm; Figure. 6.1i) adjacent to coffinite in altered granite sample is given in Table 6.6. The data (n=4) indicate restricted composition with average 13.35 wt.% S and 84.52 wt.% Pb. Further, coffinite margins also show presence of very fine-grained galena (6.1b).

Lead released during coffinitization might have precipitated as galena in the margin of coffinite, which is indicated by BSE image (Figure. 6.1b). Two such grains along the boundary of coffinite gave low analytical total due to their very small grain size (Figure. 6.1b). Semiquantitative data of such galena grains show 45 & 66 wt% PbO and 8-10 wt% S (table 6.7).

## 6.5 BARYTE

### Rock Type: Altered granite

Baryte occurs as subhedral to anhedral grains along the fractures ranging in size from 10-60 micron within granite. Mineral chemistry of three grains in the studied sample is shown in the Table 6.7. Average composition of baryte grains based on the analyses of 9 points in three grains is, BaO: 65.79 wt%, and $SO_3$: 28.88 % (Table-6.8). At places Ba is replaced by Sr due to which SrO content in some grains are elevated up to 2.26 wt%. Analytical data is given in table 6.7.

## 6.6 Ba-Al SILICATE:

### Rock Type: Altered granite

The Ba rich silicate phase (Figure. 6.1c) in the studied altered granite sample was identified/ recognised with the aid of BSE imaging facilities during EPMA analysis. Such phase occurs as a partially surrounded rim along the baryte. EPMA analysis indicated very high BaO (Av. 20.86 wt%), $Al_2O_3$ (av.15.41 wt%) and $SiO_2$ (Av. 48.44 wt%) with low analytical total (85.57-92.23 wt%) (Table-6.7). The analysis resembles a mineral named Harmotome ($BaAl_2Si_6O_6$. 6H2O) or unnamed hydrous barium silicate ($BaAl_2Si_2O_8$.4H2O) (Maria et al, 2001; web mineral page). Such phases after undergoing essential dehydration reactions form celsian ($BaAl_2Si_2O_8$ (Matsubara, 1985; Jakobsen, 1990). Mineral chemistry of the studied hydrated Ba

-Al silicate grains along with harmotome (source web mineral) and celsian (after moro et al. 2001) is given in Table-6.9.

## 6.7 CHLORITE

### Rock Type: Subfeldspathic arenite

Two phases of chlorite have been identified, one as alteration product of biotite and another along fissures appears like vein chlorite (Wu et al., 2019). Chlorite is found to be closely associated with coffinite. Analysis of chlorite (2 grains, chlorite 1 and chlorite 2) which is in vein form, is closely associated with coffinite has been carried out. Mineral chemistry of chlorite is calculated on anhydrous basis assuming 28 oxygen atoms per unit cell (Yavuz et al.,2015). Chemical analysis of chlorite (Table 6.10) indicated presence of variable MgO (3.62 - 9.88 wt.%), FeOt (30.14 - 41.17 wt.%), $SiO_2$ (22.87 - 25.17 wt.%) and $Al_2O_3$ (18.16 - 19.88 wt.%). The FeO/MgO ratio shows a significant variation within a range of 3.18 to 11.34. The mixed layer structure, inclusion and complex symbiosis of minerals can lead to errors in EPMA data of chlorite.

Foster (1962) proposed ($Na_2O + K_2O + CaO$) < 0.5% as a criterion to judge whether chlorite is contaminated or not. In the present analyses, ($Na_2O + K_2O + CaO$), also called as Xc parameter, ranges between 0.01 to 0.09%. Xc signifies empirical quantification of the proportion of smectite layers in the structure of chlorites. The quantification of Xc being well within the limits (<0.5%) indicate pure chlorite.

The chlorite is rich in Al (VI) i.e. octahedral Al as shown in Figure 6.3a (Zou et al., 2018). The chlorites fall within Type I, trioctahedral (i.e., Mg+Fe > Al(iv)) category of two-level classification scheme given by Zane and Weiss (1998) taking into account the Mg, Fe and Al (apfu) contents on Al (IV)–Mg–$Fe^{2+}$ triangular plot (Figure 6.3b). Within the Type I, all the point analysis fall within field of Fe-chlorite, compositionally towards chamosite (Figure 6.3b).

Chlorites are classified as Di- trioctahedral-Mg amesite on the xMg vs. $^{VI}R^{3+}$ diagram reflected in Figure 6.3c (Plissart et al., 2009). Classification diagram of Hey (1954) shows that the plots are mainly spread in the fields of diabantite (Ch1), pycnochlorite (Ch2) and brunsvagite (Ch3). Chlorite 1 in vicinity daphnite area and chlorite 2 in vicinity of ripidolite area (Figure 6.3d).

The non-stoichiometric behaviour of chlorite makes it potentially attractive geothermometer as chlorite composition records invaluable information about the physicochemical condition prevailing during its formation (Caritat et al.,1993). Chlorite (n=10) temperature of formation has been calculated by using different geothermometers. Cathelineau (1988) proposed that $^{IV}Al$ in chlorite is a function of temperature which has general applicability in diagenetic, hydrothermal and metamorphic settings. **a)** Average temperature of formation of chlorite by using Zang and Fyfe (1995) geothermometer vide equation, $TZF_{95\text{-}Al}{}^{IV}(^{0}C) = 106.2*\{(Al^{IV}{}_{028})-0.88*(Fe/(Fe+Mg)-0.34)\} +17.5$ is 249.6$^{0}$C (229.5$^{0}$C -264.5$^{0}$C). b). The average temperature of formation of chlorite by using Xie et al., 1997 geothermometer vide equation, $TX_{97\text{-}Al}{}^{IV}(^{0}C) =160.99*\{(Al^{IV}{}_{028})-1.33*(Fe/(Fe+Mg)-0.31)\}-61.92$ (if $Fe/(Fe+Mg) >0.31$) is 255$^{0}$C (215.6$^{0}$C -283.3$^{0}$C). c). The average temperature of formation of chlorite by using El-Sharkawy (2000) geothermometer vide equation, $TES_{00\text{-}Al}{}^{IV}(^{0}C) =106.2*\{(Al^{IV}{}_{028})-0.48*(Fe/(Fe+Mg)-0.163)\} +17.5$ is 231.8$^{0}$C (216.8$^{0}$C - 243.14$^{0}$C). Average temperature of chlorite (245$^{0}$C) indicating towards epithermal stage of hydrothermal alteration.

### 6.8 SERICITE

Two stage of sericitization is identified one is prior to uraninite formation and other one is post coffinitization associated with pyrite. Sericite mass is found to surround pyrite in both granite (Figure 6.1a & b) and subfeldspathic arenite (Figure 6.1f) from Sarangapalli area. Four points analysed from the sericite in subfeldspathic arenite indicates, highly variable composition [46.74 - 53.93 wt.% SiO2; 28.66 - 32.00 wt.% $Al_2O_3$; 2.31 - 9.45 wt.% FeO, 4.16 - 4.09 $K_2O$

and 1.57- 2.67 wt.% MgO]. On the other hand, sericite from altered granite indicate restricted compositional range [$SiO_2$ (51.30 - 52.94 wt.%), $Al_2O_3$ (30.44 - 32.08 wt.%), FeO (2.90 - 3.58 wt.%), MgO (1.29 - 1.95 wt.%) and variable $K_2O$ (2.22 - 8.67 wt.%)]. Mineral chemistry of sericite in basement granite and Banganapalle quartzite is given in Table 6.11 and Table 6.12 respectively showing similar composition of sericite in both the lithounit suggesting post sedimentation (Banganapalle sediments) alteration product.

### 6.9 Mineral paragenetic sequence

Paragenetic sequence i.e. sequential order of mineral deposition in an ore deposit is an important concept in deciphering the detailed geologic history of ore deposits. The sequence is worked out through detailed microscopic studies in polished thin section, BSE image studies as well as macroscopic field relations. Paragenetic sequence of radioactive, non-radioactive ore and rock forming minerals which are derived from hydrothermal solution have been established is tabulated below:

Table 6.1 Paragenetic sequence of radioactive and non-radioactive ore and rock forming minerals.

| | Pre-ore stage | Ore stage | Post-ore stage |
|---|---|---|---|
| Barite | ▬ | | |
| Pyrite | ▬ | ▬ | ▬ |
| Uraninite | | ▬ | |
| Coffinite | | ▬ | |
| Harmotome | | ▬ | |
| Galena | | | ▬ |
| Chlorite | ▬ | ▬ | |
| Sericite | ▬ | | ▬ |

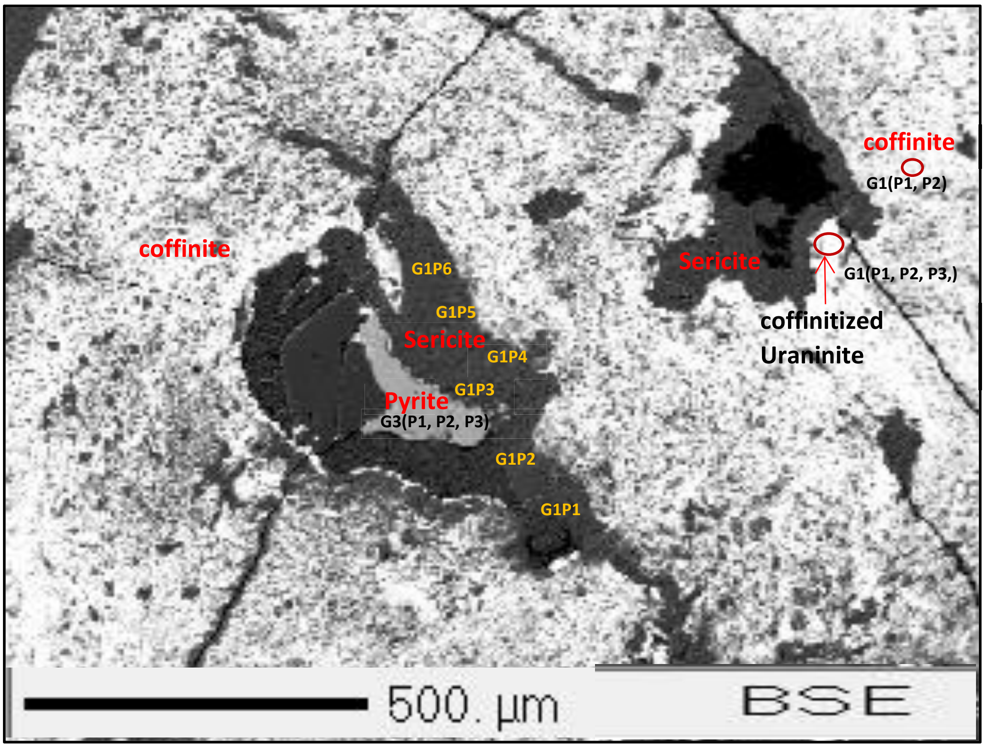

Figure.6.1a BSE image of coffinite and coffinitized uraninite associated with pyrite and sericite. as weak plane filling and along contact of pyrite, sericite and quartz in altered granite.

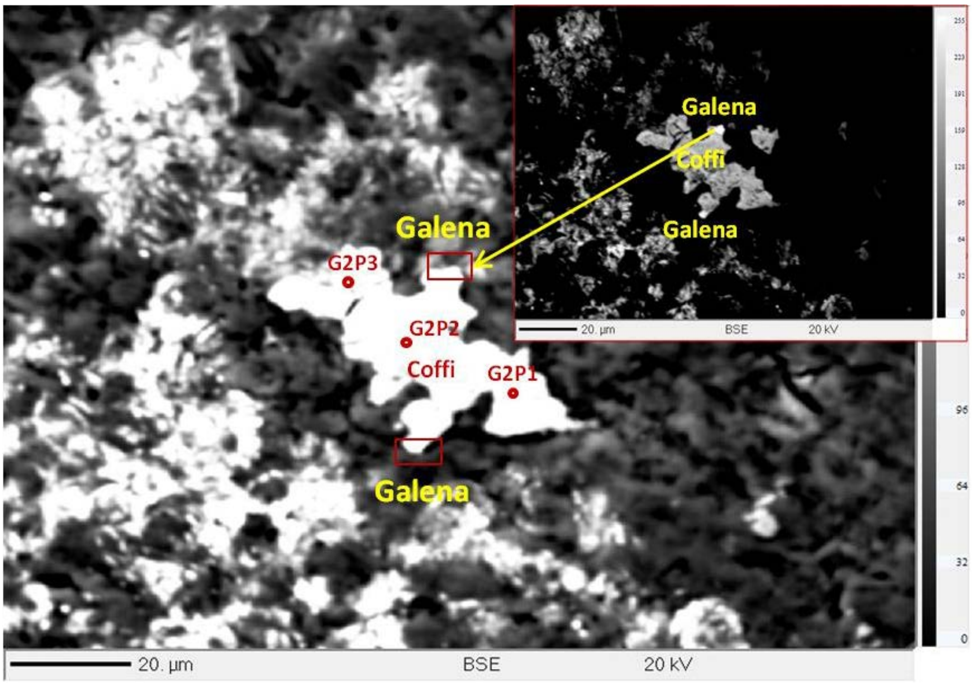

Figure. 6.1b BSE image showing occurrence of coffinite (40 micron) with irregular shaped in an assemblage of sericite, galena in the margin of coffinite (Inset). [Altered granite].

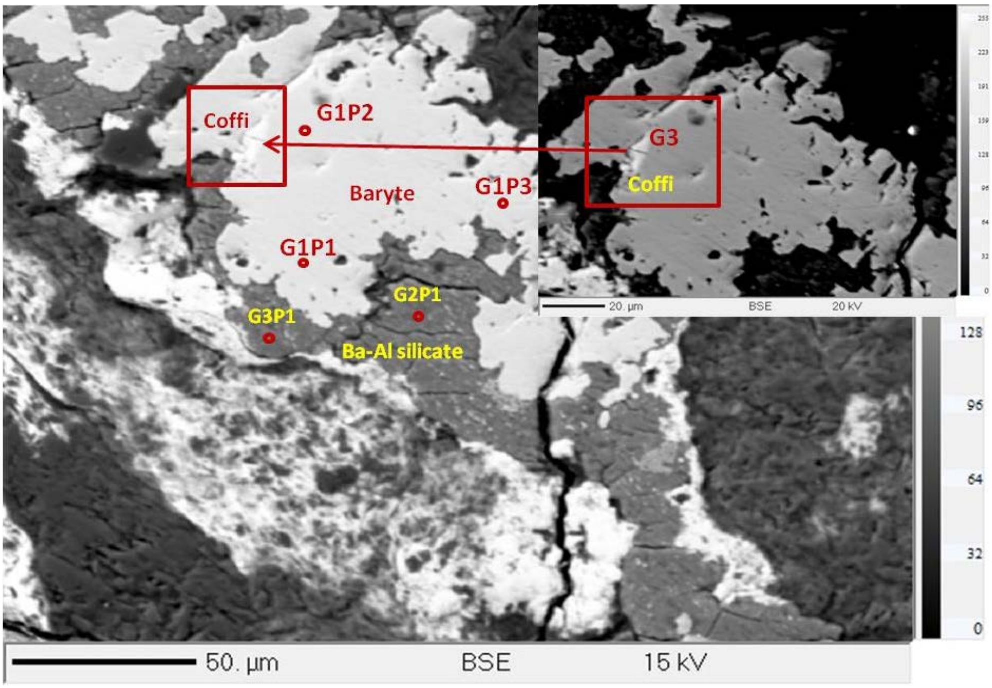

Figure. 6.1c BSE image showing occurrence of coffinite (15 micron) along fracture of baryte (60 micron). Ba-Al silicate phase partially surround the baryte in altered granite.

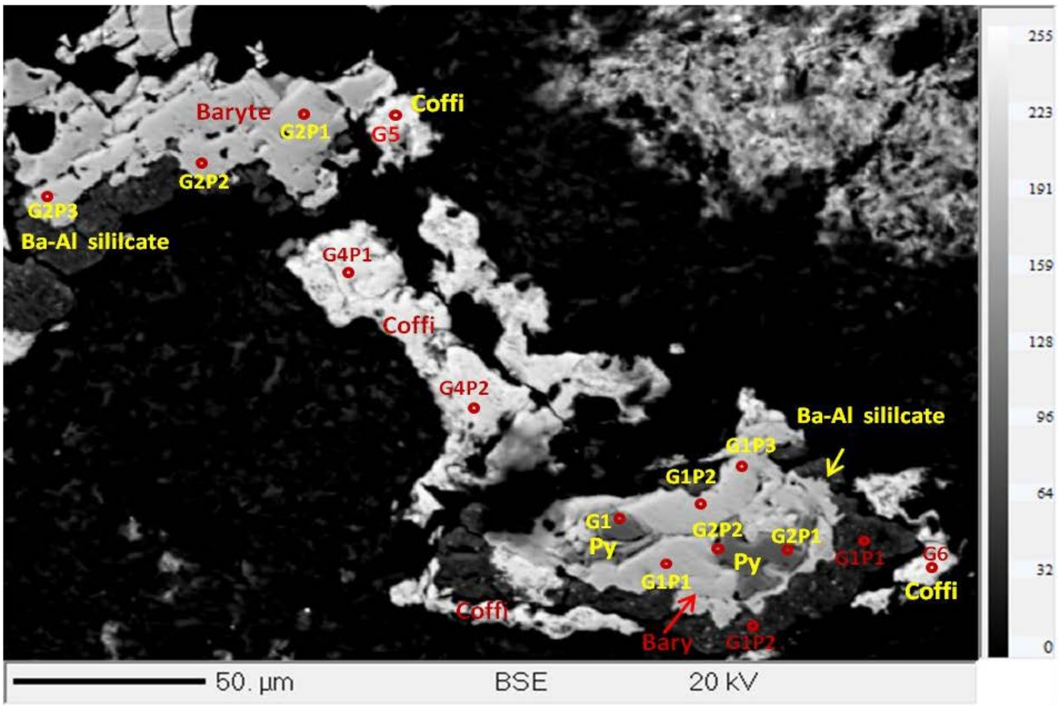

Figure. 6.1d BSE image shows occurrence of coffinite as a vein and along the periphery of Ba-Al silicate in altered granite.

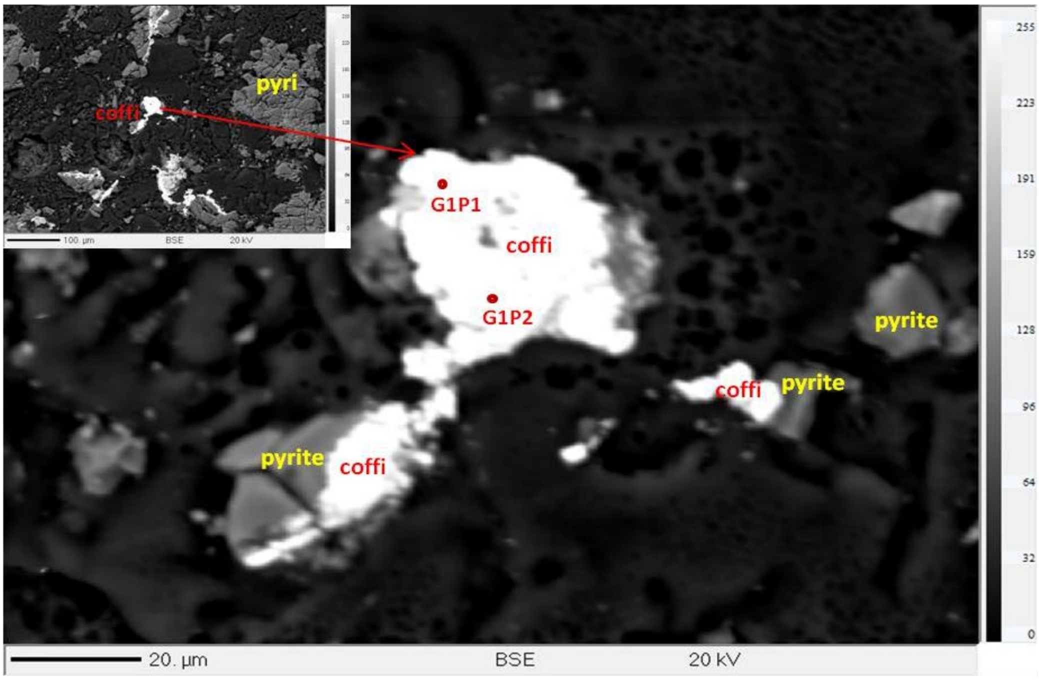

Figure. 6.1e BSE image shows coffinite is intimately associated with pyrite along the grain boundary and fracture in Sub feldspathic arenite.

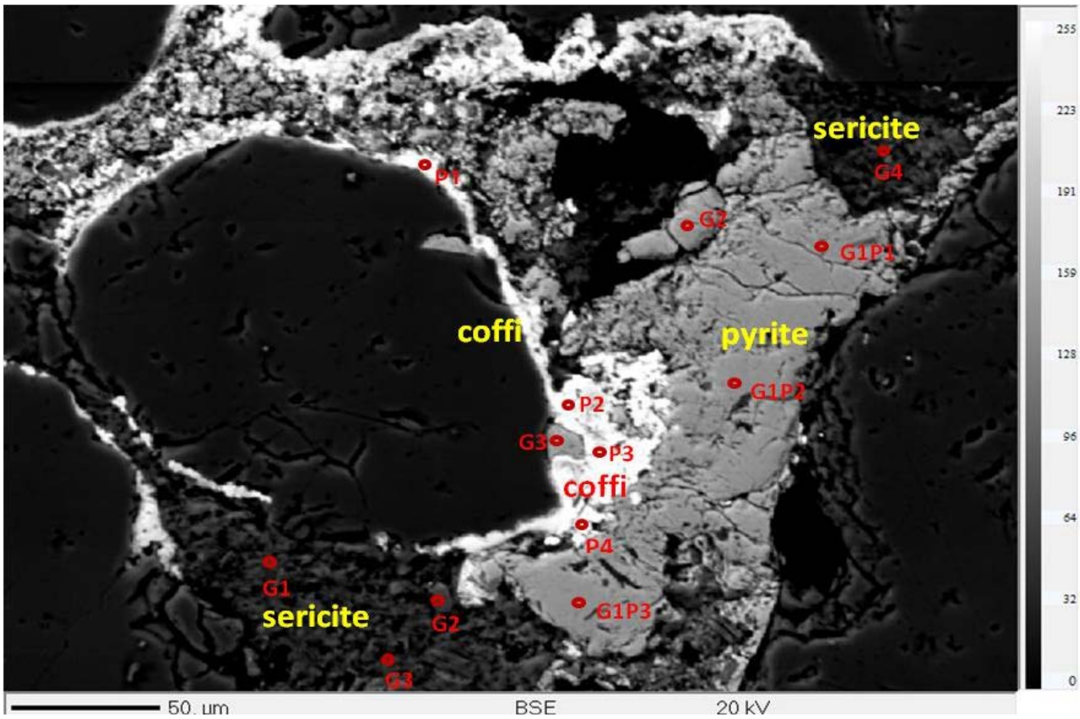

Figure. 6. BSE image showing coffinite along the grain boundary of quartz clast. Coffinite closely associated with pyrite and filling up interstitial spaces of quartz clast in sub feldspathic arenite.

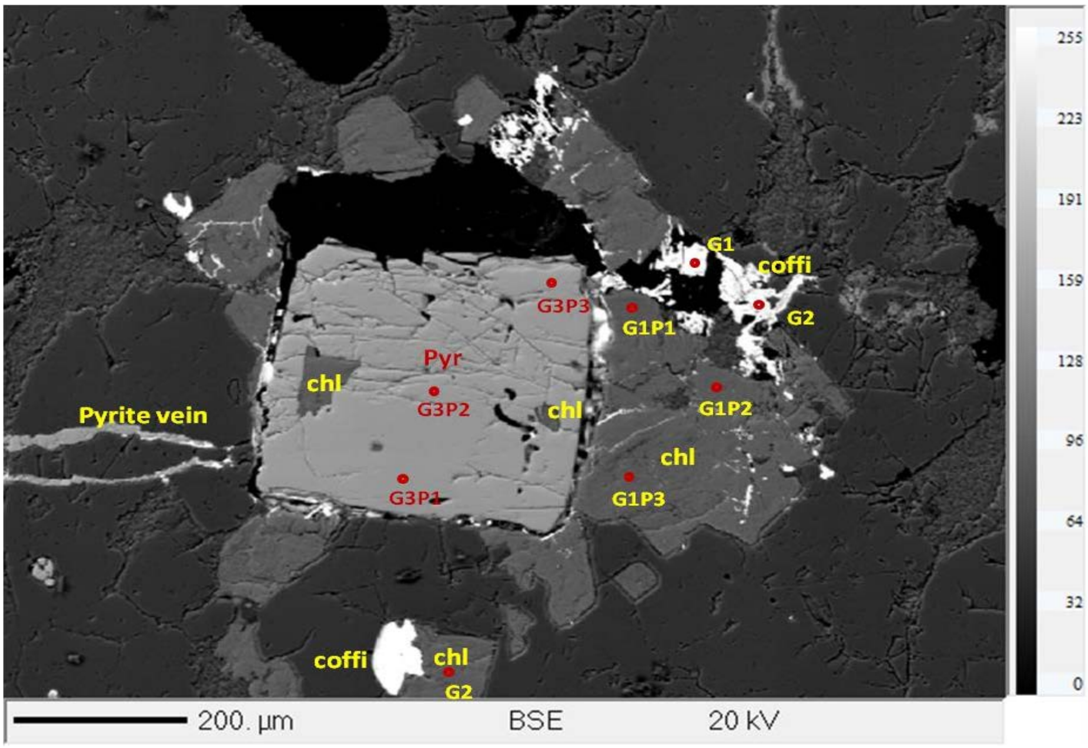

Figure.6.1g Coffinite is found along periphery of cubic pyrite and intimately associated with chlorite, pyrite-coffinite vein and coffinite along the grain boundary and fractures of chlorite in sub feldspathic arenite.

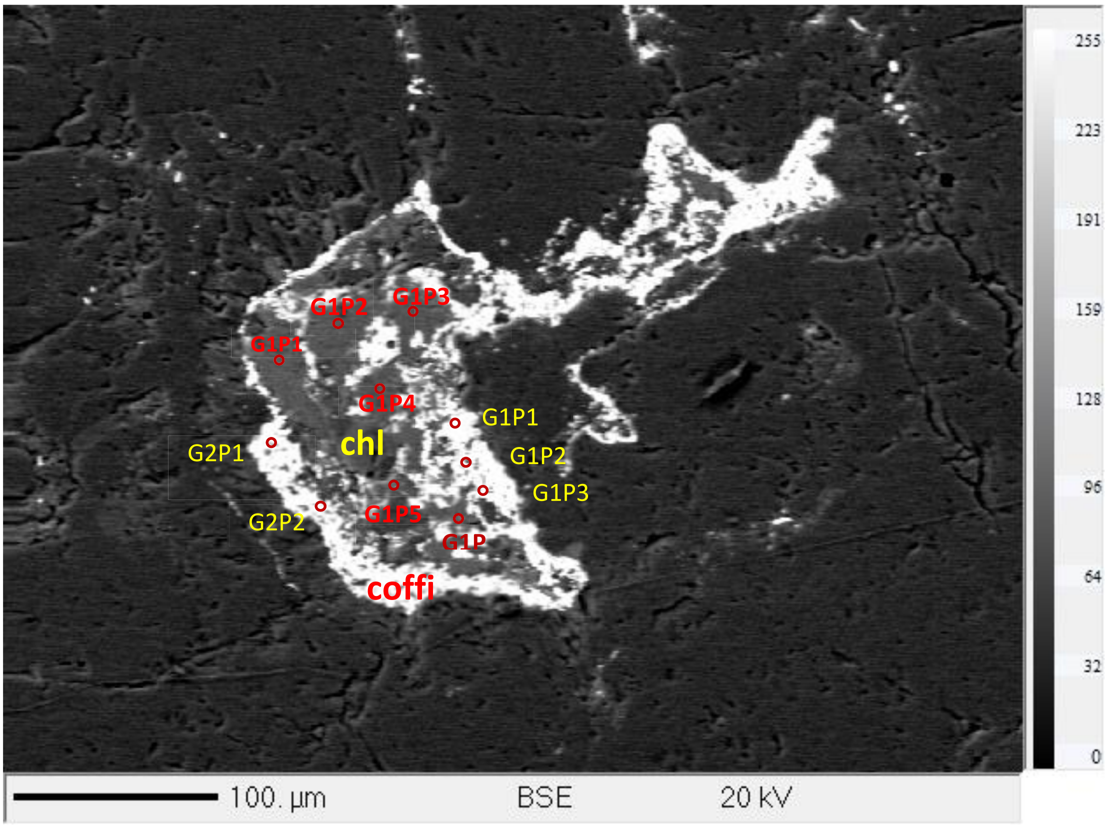

Figure.6.1h BSE image shows occurrence of coffinite encircling chlorite grain and also found filling the weak plane within chlorite in sub feldspathic arenite.

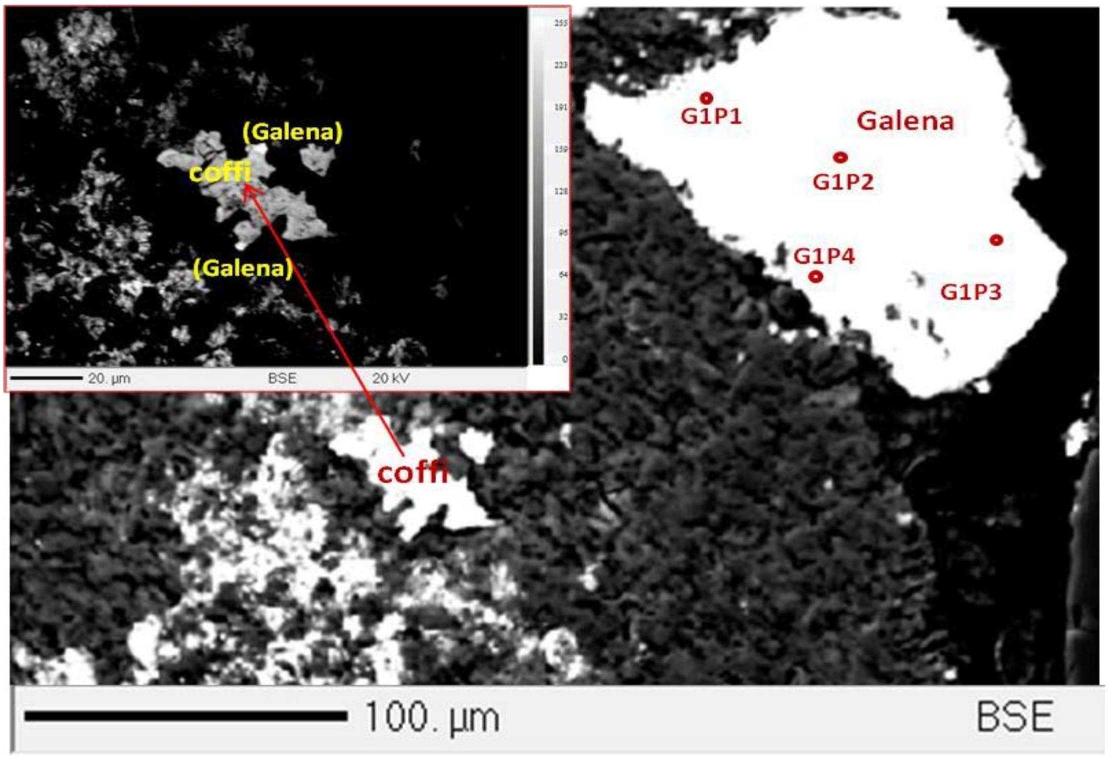

Figure.6.1i BSE image shows occurrence of galena besides coffinite in altered granite.

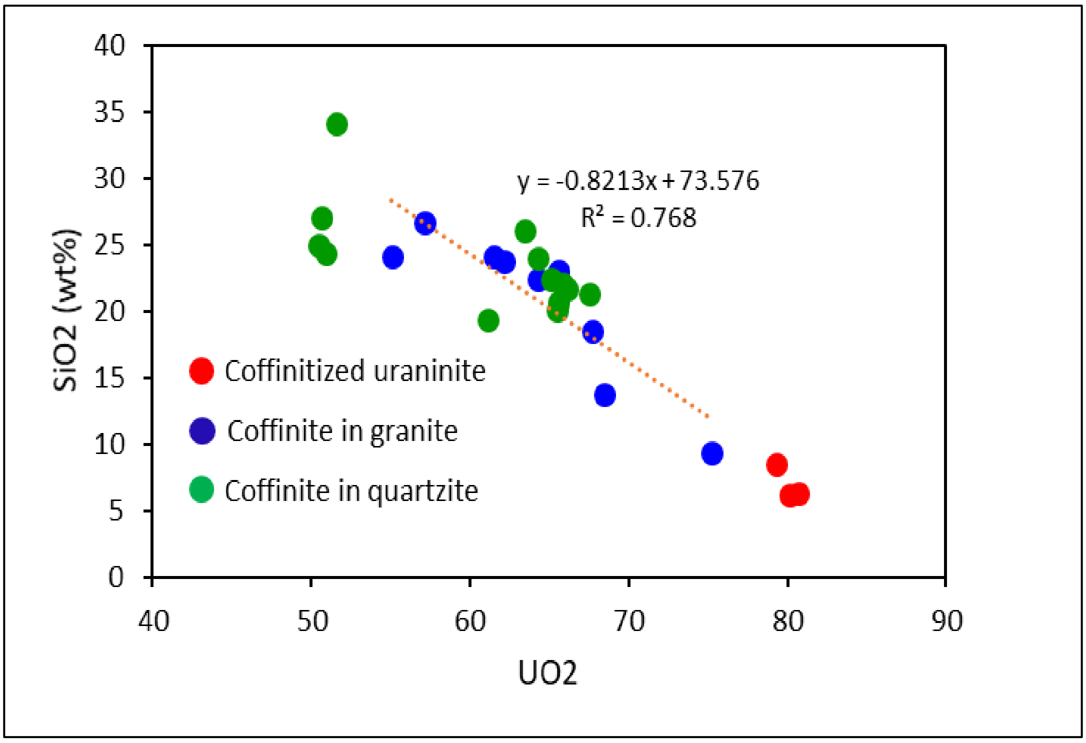

Figure.6.2 $SiO_2$(wt%) vs. $UO_2$(wt%) plot showing negative correlation.

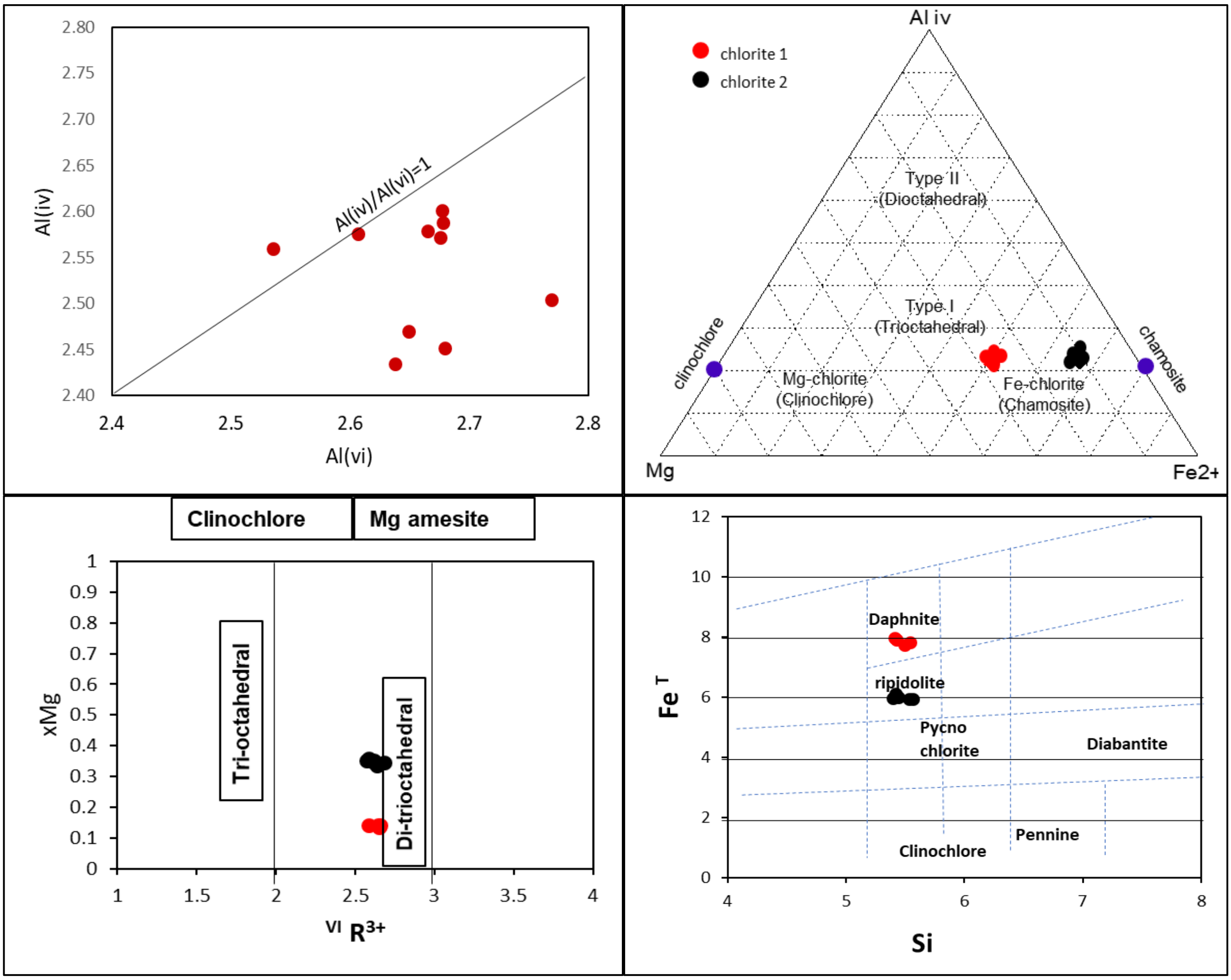

Figure. 6.3 (a) Al (IV) vs. Al (VI) diagram of chlorite after Zou et al., (2018). (b) Al-Mg-Fe Ternary diagram for classification of chlorite after Zane and Weiss (1998). (c) xMg vs. ${}^{VI}R^{3+}$ diagram after Plissart et al., (2009). And (d) FeT vs. Si classification diagram of chlorite after Hey (1954).

Table 6.2 Mineral chemistry of coffinitized uraninite in granite

| Oxide | Point analysis | | |
|---|---|---|---|
| Wt% | G1P1 | G1P2 | G1P4 |
| $Na_2O$ | 0.21 | 0.24 | 0.25 |
| $K_2O$ | 0.39 | 0.46 | 0.30 |
| CaO | 3.19 | 3.27 | 3.09 |
| MnO | 0.33 | 0.39 | 0.39 |
| FeO | 1.23 | 1.41 | 1.25 |
| PbO | 0.74 | 1.49 | 0.47 |
| $Al_2O_3$ | 1.10 | 1.96 | 0.77 |
| $Y_2O_3$ | 0.23 | 0.11 | 0.26 |
| $La_2O_3$ | 0.16 | 0.11 | 0.10 |
| $Ce_2O_3$ | 1.33 | 1.12 | 1.22 |
| $Pr_2O_3$ | 0.53 | 0.57 | 0.61 |
| $Nd_2O_3$ | 0.76 | 0.58 | 0.80 |
| $Sm_2O_3$ | 0.14 | 0.14 | 0.09 |
| $Eu_2O_3$ | 0.00 | 0.00 | 0.00 |
| $Gd_2O_3$ | 0.23 | 0.05 | 0.08 |
| $Tb_2O_3$ | 0.00 | 0.00 | 0.02 |
| $Dy_2O_3$ | 0.09 | 0.00 | 0.01 |
| $Ho_2O_3$ | 0.00 | 0.06 | 0.00 |
| $Er_2O_3$ | 0.07 | 0.01 | 0.06 |
| $Tm_2O_3$ | 0.02 | 0.00 | 0.00 |
| $Yb_2O_3$ | 0.04 | 0.07 | 0.03 |
| $Lu_2O_3$ | 0.00 | 0.00 | 0.00 |
| $SiO_2$ | 6.34 | 8.42 | 6.12 |
| $TiO_2$ | 1.30 | 1.16 | 1.19 |
| $ZrO_2$ | 0.33 | 0.31 | 0.35 |
| $HfO_2$ | 0.04 | 0.01 | 0.01 |
| $ThO_2$ | 0.00 | 0.09 | 0.03 |
| $UO_2$ | 80.70 | 79.33 | 80.10 |
| $P_2O_5$ | 0.00 | 0.00 | 0.00 |
| Total | 99.49 | 101.64 | 97.78 |
| $RE_2O_3$ | 3.37 | 2.70 | 3.01 |

Table 6.3 Mineral chemistry of coffinite in granite along with statistical evaluation of oxides.

| Oxide | Point analysis | | | | | | | | | | n=10 | |
|---|---|---|---|---|---|---|---|---|---|---|---|---|
| wt% | G1P1 | G1 P2 | G2P1 | G2P2 | G2P3 | G3 | G4P1 | G4P2 | G5 | G6 | Min | Max |
| $Na_2O$ | 0.27 | 0.23 | <0.01 | 0.24 | 0.12 | 0.08 | 0.04 | 0.06 | 0.13 | 0.01 | <0.01 | 0.27 |
| $K_2O$ | 1.01 | 0.71 | 0.68 | 0.51 | 0.58 | 0.27 | 0.41 | 0.35 | 0.46 | 0.32 | 0.27 | 1.01 |
| CaO | 2.69 | 2.39 | 1.02 | 1.13 | 1.46 | 2.05 | 2.17 | 1.48 | 1.96 | 1.60 | 1.02 | 2.69 |
| MnO | 0.35 | 0.01 | <0.01 | <0.01 | 0.06 | 0.05 | 0.09 | 0.00 | 0.08 | 0.00 | <0.01 | 0.35 |
| FeO | 2.06 | 0.01 | 0.83 | 0.37 | 0.40 | 0.12 | 0.42 | 0.34 | 0.48 | 0.68 | 0.01 | 2.06 |
| PbO | 0.62 | 0.82 | <0.01 | 0.46 | 0.43 | <0.01 | 0.07 | 0.02 | <0.01 | 0.14 | <0.01 | 0.82 |
| $Al_2O_3$ | 4.35 | 2.38 | 3.07 | 1.09 | 0.51 | 2.41 | 1.67 | 2.00 | 2.16 | 2.65 | 0.51 | 4.35 |
| $Y_2O_3$ | <0.01 | 0.19 | 3.31 | 2.14 | 0.81 | 4.35 | 2.39 | 3.94 | 2.31 | 3.05 | <0.01 | 4.35 |
| $La_2O_3$ | 0.14 | 0.15 | 0.12 | 0.14 | 0.04 | 0.01 | 0.12 | 0.08 | 0.09 | 0.17 | 0.01 | 0.17 |
| $Ce_2O_3$ | 1.02 | 1.60 | 1.18 | 1.29 | 1.00 | 1.50 | 1.10 | 0.83 | 1.22 | 1.05 | 0.83 | 1.60 |
| $Pr_2O_3$ | 0.45 | 0.09 | 0.45 | 0.76 | 0.57 | 0.58 | 0.53 | 0.63 | 0.68 | 0.56 | 0.09 | 0.76 |
| $Nd_2O_3$ | 0.48 | 0.03 | 1.86 | 1.64 | 0.77 | 1.05 | 1.13 | 1.25 | 1.26 | 1.26 | 0.03 | 1.86 |
| $Sm_2O_3$ | 0.09 | <0.01 | 0.65 | 0.44 | 0.19 | 0.44 | 0.44 | 0.61 | 0.44 | 0.50 | <0.01 | 0.65 |
| $Eu_2O_3$ | <0.01 | 0.01 | 0.18 | 0.14 | 0.10 | 0.14 | 0.13 | 0.06 | 0.10 | 0.16 | <0.01 | 0.18 |
| $Gd_2O_3$ | <0.01 | 0.00 | 0.80 | 0.64 | 0.25 | 1.20 | 0.72 | 1.16 | 0.73 | 0.85 | <0.01 | 1.20 |
| $Tb_2O_3$ | <0.01 | 0.01 | <0.01 | 0.01 | <0.01 | 0.27 | 0.16 | 0.22 | 0.09 | 0.11 | <0.01 | 0.27 |
| $Dy_2O_3$ | 0.06 | <0.01 | 0.41 | 0.36 | 0.11 | 0.76 | 0.43 | 0.72 | 0.39 | 0.59 | <0.01 | 0.76 |
| $Ho_2O_3$ | 0.15 | 0.01 | <0.01 | <0.01 | <0.01 | <0.01 | 0.14 | 0.08 | <0.01 | 0.01 | <0.01 | 0.15 |
| $Er_2O_3$ | <0.01 | 0.09 | 0.28 | 0.03 | 0.27 | 0.42 | 0.34 | 0.42 | 0.21 | 0.31 | <0.01 | 0.42 |
| $Tm_2O_3$ | <0.01 | <0.01 | <0.01 | 0.01 | 0.02 | <0.01 | <0.01 | <0.01 | <0.01 | 0.00 | <0.01 | 0.02 |
| $Yb_2O_3$ | 0.07 | 0.03 | 0.09 | 0.09 | 0.01 | 0.13 | 0.12 | 0.20 | 0.14 | 0.22 | 0.01 | 0.22 |
| $Lu_2O_3$ | 0.06 | 0.02 | <0.01 | <0.01 | <0.01 | 0.13 | 0.05 | 0.04 | 0.05 | 0.09 | <0.01 | 0.13 |
| $SiO_2$ | 13.71 | 9.28 | 24.09 | 22.49 | 23.02 | 26.69 | 18.49 | 24.10 | 22.32 | 23.78 | 9.28 | 26.69 |
| $TiO_2$ | 0.86 | 0.96 | 0.12 | 0.07 | 0.20 | 0.03 | 0.00 | <0.01 | 0.00 | 0.00 | <0.01 | 0.96 |
| $ZrO_2$ | 0.24 | 0.88 | <0.01 | 0.16 | 2.25 | <0.01 | <0.01 | <0.01 | <0.01 | <0.01 | <0.01 | 2.25 |
| $HfO_2$ | <0.01 | 0.07 | 0.07 | <0.01 | <0.01 | <0.01 | 0.09 | <0.01 | 0.13 | <0.01 | <0.01 | 0.13 |
| $ThO_2$ | 0.04 | 0.25 | <0.01 | <0.01 | 0.10 | <0.01 | 0.06 | <0.01 | 0.01 | <0.01 | <0.01 | 0.25 |
| $UO_2$ | 68.45 | 75.25 | 55.09 | 65.54 | 65.57 | 57.13 | 67.69 | 61.53 | 64.28 | 62.12 | 55.09 | 75.25 |
| $P_2O_5$ | <0.01 | 0.03 | 1.14 | 1.15 | 1.09 | 1.00 | 0.39 | 0.68 | 0.48 | 0.61 | <0.01 | 1.15 |
| Total | 97.15 | 95.49 | 95.45 | 100.91 | 99.92 | 100.81 | 99.37 | 100.77 | 100.18 | 100.81 | | |
| $RE_2O_3$ | 2.51 | 2.04 | 6.02 | 5.55 | 3.31 | 6.64 | 5.40 | 6.28 | 5.39 | 5.87 | 2.04 | 6.64 |

Table 6.4 Mineral chemistry of coffinite in subfeldspathic arenite along with statistical evaluation of oxides.

| Oxide | Point analysis | | | | | | | | | | | | | n=14 | |
|---|---|---|---|---|---|---|---|---|---|---|---|---|---|---|---|
| wt% | G1P1 | G1P2 | P1 | P2 | P3 | P4 | G1 | G2 | G1P1 | G1P2 | G1P3 | G2P1 | G2P2 | min | max |
| $Na_2O$ | 0.13 | 0.08 | 0.02 | 0.21 | 0.05 | 0.26 | 0.36 | 0.40 | 0.00 | 0.07 | 0.13 | 0.11 | 0.10 | 0.00 | 0.40 |
| $K_2O$ | 0.49 | 0.50 | 1.03 | 2.10 | 0.52 | 1.51 | 0.32 | 0.64 | 0.22 | 0.24 | 0.31 | 0.26 | 0.29 | 0.22 | 2.10 |
| CaO | 0.82 | 1.59 | 1.12 | 0.93 | 0.96 | 0.87 | 1.22 | 0.96 | 1.25 | 1.22 | 1.24 | 0.93 | 1.11 | 0.82 | 1.59 |
| MnO | 0.00 | 0.00 | 0.02 | 0.07 | 0.00 | 0.01 | 0.00 | 0.00 | 0.00 | 0.00 | 0.05 | 0.00 | 0.03 | 0.00 | 0.07 |
| FeO | 0.00 | 0.03 | 1.28 | 3.04 | 0.94 | 5.78 | 0.19 | 0.54 | 0.79 | 0.86 | 1.33 | 0.76 | 3.08 | 0.00 | 5.78 |
| PbO | 0.08 | 0.42 | 0.11 | 0.14 | 0.17 | 0.20 | 0.15 | 2.81 | 1.67 | 1.42 | 1.30 | 2.95 | 1.11 | 0.08 | 2.95 |
| $Al_2O_3$ | 2.24 | 2.09 | 3.19 | 6.29 | 2.38 | 5.95 | 1.59 | 2.81 | 0.63 | 0.56 | 0.93 | 0.89 | 2.74 | 0.56 | 6.29 |
| $Y_2O_3$ | 2.44 | 2.01 | 0.84 | 1.58 | 1.50 | 1.50 | 1.76 | 2.00 | 1.99 | 2.20 | 2.11 | 1.72 | 1.63 | 0.84 | 2.44 |
| $La_2O_3$ | 0.20 | 0.24 | 0.26 | 0.20 | 0.29 | 0.18 | 0.23 | 0.20 | 0.00 | 0.00 | 0.00 | 0.00 | 0.00 | 0.00 | 0.29 |
| $Ce_2O_3$ | 0.80 | 0.93 | 0.97 | 0.90 | 0.91 | 0.77 | 0.98 | 0.90 | 1.03 | 0.94 | 0.83 | 0.83 | 0.80 | 0.77 | 1.03 |
| $Pr_2O_3$ | 0.60 | 0.46 | 0.53 | 0.40 | 0.44 | 0.47 | 0.71 | 0.58 | 0.51 | 0.44 | 0.26 | 0.11 | 0.51 | 0.11 | 0.71 |
| $Nd_2O_3$ | 0.74 | 0.58 | 0.59 | 0.47 | 0.81 | 0.54 | 1.35 | 1.28 | 0.02 | 0.15 | 0.20 | 0.14 | 0.03 | 0.02 | 1.35 |
| $Sm_2O_3$ | 0.24 | 0.19 | 0.21 | 0.23 | 0.21 | 0.20 | 0.53 | 0.35 | 0.01 | 0.04 | 0.11 | 0.04 | 0.00 | 0.00 | 0.53 |
| $Eu_2O_3$ | 0.13 | 0.06 | 0.12 | 0.06 | 0.06 | 0.04 | 0.21 | 0.14 | 0.07 | 0.00 | 0.00 | 0.02 | 0.04 | 0.00 | 0.21 |
| $Gd_2O_3$ | 0.49 | 0.61 | 0.20 | 0.00 | 0.38 | 0.00 | 0.64 | 0.46 | 0.09 | 0.37 | 0.28 | 0.28 | 0.05 | 0.00 | 0.64 |
| $Tb_2O_3$ | 0.04 | 0.00 | 0.00 | 0.00 | 0.00 | 0.00 | 0.09 | 0.02 | 0.00 | 0.00 | 0.00 | 0.01 | 0.00 | 0.00 | 0.09 |
| $Dy_2O_3$ | 0.26 | 0.18 | 0.16 | 0.05 | 0.13 | 0.00 | 0.16 | 0.04 | 0.24 | 0.16 | 0.12 | 0.17 | 0.09 | 0.00 | 0.26 |
| $Ho_2O_3$ | 0.00 | 0.00 | 0.03 | 0.02 | 0.00 | 0.00 | 0.06 | 0.00 | 0.03 | 0.00 | 0.08 | 0.06 | 0.00 | 0.00 | 0.08 |
| $Er_2O_3$ | 0.13 | 0.09 | 0.04 | 0.15 | 0.29 | 0.07 | 0.15 | 0.16 | 0.31 | 0.19 | 0.03 | 0.06 | 0.26 | 0.03 | 0.31 |
| $Tm_2O_3$ | 0.01 | 0.05 | 0.00 | 0.00 | 0.00 | 0.00 | 0.00 | 0.04 | 0.00 | 0.00 | 0.00 | 0.00 | 0.00 | 0.00 | 0.05 |
| $Yb_2O_3$ | 0.05 | 0.05 | 0.09 | 0.03 | 0.08 | 0.06 | 0.00 | 0.00 | 0.09 | 0.10 | 0.19 | 0.05 | 0.00 | 0.00 | 0.19 |
| $Lu_2O_3$ | 0.05 | 0.08 | 0.00 | 0.02 | 0.07 | 0.00 | 0.07 | 0.00 | 0.01 | 0.00 | 0.00 | 0.01 | 0.03 | 0.00 | 0.08 |
| $SiO_2$ | 26.02 | 21.98 | 19.31 | 24.96 | 23.99 | 24.37 | 21.35 | 34.12 | 20.12 | 20.68 | 21.67 | 26.96 | 22.40 | 19.31 | 34.12 |
| $TiO_2$ | 0.20 | 0.26 | 0.58 | 0.20 | 0.70 | 0.35 | 0.41 | 0.20 | 0.05 | 0.10 | 0.05 | 0.16 | 0.03 | 0.03 | 0.70 |
| $ZrO_2$ | 0.00 | 0.13 | 0.11 | 0.02 | 0.86 | 0.24 | 0.00 | 0.00 | 0.42 | 0.30 | 0.19 | 0.34 | 0.14 | 0.00 | 0.86 |
| $HfO_2$ | 0.00 | 0.00 | 0.00 | 0.00 | 0.00 | 0.02 | 0.00 | 0.10 | 0.00 | 0.00 | 0.30 | 0.07 | 0.07 | 0.00 | 0.30 |
| $ThO_2$ | 0.00 | 0.16 | 0.06 | 0.03 | 0.20 | 0.05 | 0.00 | 0.00 | 0.00 | 0.00 | 0.00 | 0.00 | 0.01 | 0.00 | 0.20 |
| $UO_2$ | 63.43 | 65.84 | 61.10 | 50.47 | 64.31 | 50.89 | 67.52 | 51.58 | 65.50 | 65.61 | 66.15 | 50.62 | 65.12 | 50.47 | 67.52 |
| $P_2O_5$ | 0.39 | 0.38 | 0.12 | 0.21 | 0.31 | 0.19 | 0.28 | 0.25 | 0.46 | 0.52 | 0.63 | 0.37 | 0.34 | 0.12 | 0.63 |
| Total | 100.12 | 99.22 | 93.86 | 94.16 | 101.09 | 101.86 | 100.50 | 100.50 | 98.38 | 98.75 | 100.71 | 90.66 | 103.05 | 90.66 | 103.05 |
| RE2O3 | 3.721 | 3.503 | 3.2 | 2.536 | 3.651 | 2.329 | 5.159 | 4.158 | 2.40 | 2.39 | 2.10 | 1.77 | 1.79 | 1.77 | 5.16 |

Table 6.5 Mineral chemistry of pyrite in granite along with statistical evaluation of elements.

| Element | Point analysis | | | | | | n=6 | |
|---|---|---|---|---|---|---|---|---|
| wt.% | G1 | G2P1 | G2P2 | G3P1 | G3P2 | G3P3 | Min | Max |
| S | 52.63 | 52.16 | 52.10 | 52.03 | 52.64 | 52.62 | 52.03 | 52.64 |
| Fe | 45.42 | 45.80 | 45.79 | 46.39 | 45.99 | 45.54 | 45.42 | 46.39 |
| Co | 0.03 | 0.02 | 0.07 | 0.03 | <0.01 | <0.01 | 0.02 | 0.07 |
| Ni | 0.03 | 0.02 | <0.01 | <0.01 | <0.01 | <0.01 | 0.02 | 0.03 |
| Cu | 0.03 | 0.02 | <0.01 | <0.01 | <0.01 | <0.01 | 0.02 | 0.03 |
| Zn | <0.01 | 0.00 | 0.04 | 0.01 | 0.04 | <0.01 | <0.01 | 0.04 |
| As | 0.05 | 0.05 | 0.05 | 0.05 | 0.04 | 0.05 | 0.04 | 0.05 |
| Se | 0.02 | 0.00 | 0.02 | 0.01 | 0.03 | <0.01 | <0.01 | 0.03 |
| Mo | 0.72 | 0.93 | 0.93 | 0.75 | 0.80 | 0.82 | 0.72 | 0.93 |
| Ag | 0.06 | 0.04 | 0.02 | <0.01 | 0.07 | 0.06 | 0.02 | 0.07 |
| Au | 0.00 | 0.00 | <0.01 | <0.01 | <0.01 | 0.00 | <0.01 | <0.01 |
| Pb | 0.18 | 0.06 | 0.13 | 0.05 | 0.03 | 0.30 | 0.03 | 0.30 |
| Bi | 0.17 | 0.23 | 0.14 | 0.19 | 0.16 | 0.13 | 0.13 | 0.23 |
| Total | 99.32 | 99.32 | 99.30 | 99.51 | 99.78 | 99.52 | 99.30 | 99.78 |

Table 6.6 Mineral chemistry of pyrite in subfeldspathic arenite along with statistical evaluation of elements.

| Element | Point analysis | | | | | | | n=7 | |
|---|---|---|---|---|---|---|---|---|---|
| wt.% | G1P1 | G1P2 | G1P3 | G2 | G3P1 | G3P2 | G3P3 | Min | Max |
| S | 52.79 | 52.03 | 50.64 | 53.48 | 52.84 | 53.01 | 52.84 | 50.64 | 52.79 |
| Fe | 44.39 | 45.44 | 44.85 | 45.00 | 46.55 | 46.95 | 46.61 | 44.39 | 45.82 |
| Co | 0.03 | 0.01 | 0.02 | <0.01 | 0.01 | 0.03 | 0.02 | 0.01 | 0.04 |
| Ni | 0.01 | 0.03 | 0.01 | 0.02 | 0.09 | 0.09 | 0.00 | 0.01 | 0.03 |
| Cu | 0.05 | 0.01 | 0.03 | 0.01 | 0.02 | 0.01 | 0.00 | 0.01 | 0.05 |
| Zn | <0.01 | 0.02 | 0.02 | <0.01 | 0.07 | 0.00 | 0.00 | 0.02 | 0.02 |
| As | <0.01 | 0.02 | 0.01 | 0.02 | 0.06 | 0.09 | 0.02 | 0.01 | 0.05 |
| Se | 0.01 | <0.01 | 0.01 | <0.01 | 0.03 | <0.01 | 0.04 | <0.01 | 0.02 |
| Mo | 0.89 | 0.79 | 0.73 | 0.83 | 0.75 | 0.78 | 0.86 | 0.73 | 0.89 |
| Ag | <0.01 | 0.04 | 0.00 | 0.02 | <0.01 | 0.00 | 0.01 | 0.00 | 0.05 |
| Au | <0.01 | 0.00 | 0.00 | 0.00 | 0.10 | 0.15 | <0.01 | <0.01 | <0.01 |
| Pb | 0.24 | 0.16 | 0.14 | 0.19 | 0.22 | 0.19 | 0.22 | 0.12 | 0.24 |
| Bi | 0.14 | 0.15 | 0.13 | 0.07 | 0.17 | 0.24 | 0.16 | 0.13 | 0.17 |
| Total | 98.58 | 98.82 | 96.62 | 99.69 | 100.89 | 101.55 | 100.93 | 96.62 | 99.46 |

Table 6.7 Mineral chemistry of galena in granite along with statistical evaluation of elements.

| element | Point analysis | | | | n=6 | |
|---|---|---|---|---|---|---|
| wt % | G1P1 | G1P2 | G1P3 | G1P4 | Min | Max |
| S | 13.28 | 13.33 | 13.56 | 13.22 | 13.22 | 13.56 |
| Fe | 0.05 | 0.02 | 0.02 | 0.01 | 0.01 | 0.05 |
| Co | 0.02 | <0.01 | <0.01 | <0.01 | 0.02 | 0.02 |
| Ni | 0.02 | 0.05 | <0.01 | <0.01 | 0.02 | 0.05 |
| Cu | 0.07 | 0.01 | 0.01 | 0.01 | 0.01 | 0.07 |
| Zn | <0.01 | 0.03 | <0.01 | <0.01 | 0.03 | 0.03 |
| As | <0.01 | 0.03 | <0.01 | <0.01 | 0.03 | 0.03 |
| Mo | 0.16 | 0.16 | 0.29 | 0.20 | 0.16 | 0.29 |
| Ag | <0.01 | <0.01 | <0.01 | 0.08 | 0.08 | 0.08 |
| Cd | <0.01 | <0.01 | 0.05 | <0.01 | 0.05 | 0.05 |
| Au | <0.01 | <0.01 | <0.01 | <0.01 | 0.00 | 0.00 |
| Pb | 84.44 | 84.64 | 84.47 | 84.53 | 84.44 | 84.64 |
| Se | <0.01 | 0.02 | 0.01 | <0.01 | <0.01 | 0.02 |
| Bi | 0.33 | 0.33 | 0.34 | 0.15 | 0.15 | 0.34 |
| Total | 98.36 | 98.74 | 98.75 | 98.21 | 98.21 | 98.75 |

Table 6.8 Mineral chemistry of baryte in granite along with statistical evaluation of elements.

| oxide | Point analysis | | | | | | | | | n=9 | |
|---|---|---|---|---|---|---|---|---|---|---|---|
| wt % | G1P1 | G1P2 | G1P3 | G2P1 | G2P2 | G2P3 | G3P1 | G3P2 | G3P3 | Min | Max |
| CaO | <0.01 | <0.01 | <0.01 | 0.01 | 0.03 | 0.01 | <0.01 | <0.01 | 0.013 | <0.01 | 0.03 |
| SO3 | 28.2 | 28.4 | 28.6 | 27.8 | 28.8 | 29.3 | 29.6 | 30.0 | 29.2 | 27.8 | 30.0 |
| FeO | 0.21 | 0.13 | 0.09 | 0.04 | 0.10 | 0.06 | <0.01 | 0.096 | <0.01 | <0.01 | 0.21 |
| BaO | 68.06 | 65.69 | 65.85 | 67.39 | 64.15 | 66.49 | 69.09 | 63.95 | 61.43 | 61.43 | 69.09 |
| MnO | <0.01 | 0.021 | <0.01 | <0.01 | <0.01 | <0.01 | <0.01 | <0.01 | <0.01 | <0.01 | 0.02 |
| SrO | 0.19 | 0.30 | 0.52 | 0.03 | 0.47 | 0.16 | 0.18 | 0.39 | 2.26 | 0.03 | 2.26 |
| PbO | <0.01 | 0.014 | 0.017 | <0.01 | 0.042 | 0.037 | <0.01 | 0.169 | 0.155 | <0.01 | 0.17 |
| Total | 96.62 | 94.55 | 95.11 | 95.30 | 93.58 | 96.03 | 98.91 | 94.62 | 93.04 | 93.04 | 98.91 |

Table 6.9 Statistical evaluation of mineral chemistry of Ba-Al silicate along with chemistry of Harmotome and celsian.

| oxides | n=4 | | Harmotome | Celsian |
|---|---|---|---|---|
| wt % | Min | Max | | |
| $Na_2O$ | 0.05 | 0.18 | 0.88 | 0.18 |
| $K_2O$ | 0.14 | 0.38 | 0.67 | 0.18 |
| CaO | 0.59 | 0.78 | NA | 0.08 |
| FeO | 1.59 | 4.43 | - | - |
| BaO | 17.71 | 24.33 | 17.41 | 41.39 |
| $Al_2O_3$ | 14.48 | 16.37 | 14.46 | 24.67 |
| $SiO_2$ | 47.81 | 49.58 | 51.14 | 32.06 |

Table 6.10 Mineral chemistry of chlorite

| oxides | Point analysis | | | | | | | | | |
|---|---|---|---|---|---|---|---|---|---|---|
| wt % | G1P1 | G1P2 | G1P3 | G2 | G1P1 | G1P2 | G1P3 | G1P4 | G1P5 | G1P6 |
| $Na_2O$ | <0.01 | 0.01 | 0.01 | 0.01 | 0.05 | 0.02 | <0.01 | 0.02 | <0.01 | 0.02 |
| $K_2O$ | <0.01 | 0.00 | 0.01 | 0.01 | 0.02 | 0.02 | 0.04 | 0.05 | 0.02 | 0.01 |
| MgO | 3.77 | 3.73 | 3.62 | 3.84 | 9.20 | 9.88 | 9.61 | 9.45 | 9.75 | 9.47 |
| CaO | <0.01 | <0.01 | <0.01 | <0.01 | <0.01 | 0.03 | 0.01 | 0.03 | <0.01 | 0.03 |
| MnO | 0.03 | 0.10 | 0.06 | 0.13 | 0.07 | 0.00 | 0.07 | 0.11 | <0.01 | 0.08 |
| FeO | 40.36 | 40.56 | 41.04 | 41.17 | 32.47 | 32.52 | 32.00 | 31.78 | 32.10 | 30.14 |
| $Al_2O_3$ | 19.48 | 19.09 | 19.23 | 19.15 | 19.72 | 19.83 | 19.54 | 19.88 | 19.42 | 18.16 |
| $Cr_2O_3$ | <0.01 | <0.01 | <0.01 | 0.00 | 0.07 | <0.01 | 0.03 | 0.07 | 0.01 | <0.01 |
| $SiO_2$ | 24.00 | 23.31 | 23.33 | 24.47 | 24.06 | 24.49 | 24.96 | 24.01 | 25.17 | 22.87 |
| $TiO_2$ | 0.05 | 0.08 | 0.06 | 0.06 | 0.03 | 0.17 | 0.21 | 0.16 | 0.15 | 0.22 |
| Total | 87.76 | 86.90 | 87.50 | 88.85 | 85.75 | 87.03 | 86.60 | 85.79 | 86.75 | 81.04 |
| Si | 5.496 | 5.429 | 5.412 | 5.548 | 5.421 | 5.424 | 5.531 | 5.399 | 5.565 | 5.440 |
| Al iv | 2.504 | 2.571 | 2.588 | 2.452 | 2.579 | 2.576 | 2.469 | 2.601 | 2.435 | 2.560 |
| Al vi | 2.769 | 2.676 | 2.678 | 2.679 | 2.665 | 2.607 | 2.649 | 2.677 | 2.638 | 2.535 |
| Ti | 0.008 | 0.014 | 0.011 | 0.011 | 0.005 | 0.028 | 0.036 | 0.026 | 0.025 | 0.039 |
| Cr | 0.001 | 0.001 | 0.001 | 0.001 | 0.012 | 0.001 | 0.006 | 0.012 | 0.001 | 0.001 |
| Fe3+ | 0.154 | 0.072 | 0.060 | 0.136 | 0.048 | 0.042 | 0.137 | 0.069 | 0.137 | 0.024 |
| Fe2+ | 7.575 | 7.826 | 7.904 | 7.671 | 6.070 | 5.981 | 5.793 | 5.908 | 5.798 | 5.973 |
| Mn | 0.005 | 0.019 | 0.012 | 0.025 | 0.014 | 0.000 | 0.013 | 0.020 | 0.001 | 0.015 |
| Mg | 1.287 | 1.296 | 1.252 | 1.299 | 3.089 | 3.261 | 3.175 | 3.169 | 3.215 | 3.357 |
| Ca | 0.001 | 0.001 | 0.001 | 0.001 | 0.001 | 0.007 | 0.003 | 0.007 | 0.001 | 0.008 |
| Na | 0.004 | 0.006 | 0.005 | 0.005 | 0.042 | 0.020 | 0.004 | 0.014 | 0.004 | 0.018 |
| K | 0.003 | 0.000 | 0.005 | 0.005 | 0.013 | 0.010 | 0.021 | 0.026 | 0.014 | 0.006 |
| OH* | 16 | 16 | 16 | 16 | 16 | 16 | 16 | 16 | 16 | 16 |
| Fe/Fe+Mg | 0.857 | 0.859 | 0.864 | 0.857 | 0.665 | 0.649 | 0.651 | 0.654 | 0.649 | 0.641 |

Table 6. 11 Mineral chemistry of sericite along with statistical evaluation of oxides in granite

| Oxide | B-487-SGP-21-155.5_Alt Granite | | | | | n=5 | |
|---|---|---|---|---|---|---|---|
| wt.% | G1P1 | G1P2 | G1P3 | G1P4 | G1P5 | Min | Max |
| $Na_2O$ | 0.06 | 0.02 | 0.06 | 0.02 | 0.06 | 0.02 | 0.06 |
| $K_2O$ | 3.02 | 8.67 | 2.43 | 7.81 | 2.22 | 2.22 | 8.67 |
| MgO | 1.73 | 1.81 | 1.68 | 1.95 | 1.29 | 1.29 | 1.95 |
| CaO | 0.10 | 0.13 | 0.09 | 0.14 | 0.22 | 0.09 | 0.22 |
| MnO | <0.01 | 0.06 | <0.01 | 0.06 | 0.02 | <0.01 | 0.06 |
| FeO | 3.05 | 3.40 | 2.90 | 3.58 | 3.57 | 2.90 | 3.58 |
| BaO | 0.61 | 0.60 | 0.64 | 0.58 | 1.22 | 0.58 | 1.22 |
| $Al_2O_3$ | 31.96 | 31.77 | 32.08 | 31.31 | 30.44 | 30.44 | 32.08 |
| $Cr_2O_3$ | <0.01 | 0.03 | 0.02 | 0.02 | <0.01 | <0.01 | 0.03 |
| $SiO_2$ | 52.93 | 51.30 | 52.91 | 52.94 | 51.90 | 51.30 | 52.94 |
| $TiO_2$ | 0.05 | 0.17 | 0.10 | 0.02 | 0.08 | 0.02 | 0.17 |
| F | 0.18 | 0.26 | 0.27 | 0.27 | 0.22 | 0.18 | 0.27 |
| Total | 93.81 | 98.22 | 93.23 | 98.74 | 91.25 | 91.25 | 98.74 |

Table 6. 12 Mineral chemistry of sericite along with statistical evaluation of oxides in Subfeldspathic arenite

| Oxide | B-486-SGP-21-154.4-Subfelds arenite | | | | n=4 | |
|---|---|---|---|---|---|---|
| wt.% | G1 | G2 | G3 | G4 | Min | Max |
| $Na_2O$ | 0.10 | 0.07 | 0.08 | 0.13 | 0.07 | 0.13 |
| $K_2O$ | 4.23 | 6.56 | 4.16 | 7.09 | 4.16 | 7.09 |
| MgO | 1.57 | 1.94 | 1.60 | 2.67 | 1.57 | 2.67 |
| CaO | 0.15 | 0.22 | 0.14 | 0.09 | 0.09 | 0.22 |
| MnO | 0.03 | 0.09 | 0.07 | 0.05 | 0.03 | 0.09 |
| FeO | 2.52 | 2.74 | 2.31 | 9.45 | 2.31 | 9.45 |
| BaO | 0.68 | 1.00 | 0.67 | 0.45 | 0.45 | 1.00 |
| $Al_2O_3$ | 31.06 | 32.00 | 30.57 | 28.66 | 28.66 | 32.00 |
| $Cr_2O_3$ | 0.04 | 0.00 | 0.00 | 0.01 | <0.01 | 0.04 |
| $SiO_2$ | 52.14 | 53.93 | 50.63 | 46.74 | 46.74 | 53.93 |
| $TiO_2$ | 0.09 | 0.07 | 0.17 | 0.20 | 0.07 | 0.20 |
| F | 0.15 | 0.14 | 0.21 | 0.15 | 0.14 | 0.21 |
| Total | 92.78 | 98.76 | 90.65 | 95.74 | 90.65 | 98.76 |

# CHAPTER 7

# GEOCHEMISTRY

## ANALYTICAL TECHNIQUES

A total of 91 samples have been analysed for major and minor and trace elements by WDXRF technique (50 Banganapalle quartzite and 35 basement granite). This includes radioactive Banganapalle quartzite (n=34), non-radioactive Banganapalle quartzite (n=16), radioactive basement granite (n=17) and non-radioactive basement granite (n=18) collected from borehole core and 6 representative, non-radioactive grab samples of Banganapalle quartzite collected from surface outcrops. These fresh core and grab samples of each weighing nearly 0.5-1 kg hammered to blocks and then to chips of 1" size by using jaw crusher. These chips then grounded to fine powder of 75µ size (ASTM -200 #) by using pulverizing disc mill which ensures the homogeneity of the samples. 1gm of such representative powdered sample after multiple coning and quartering has been pelletized using boric acid to circular discs of 41mm size. International standard reference materials are used for calibrations. The analytical precision (RSD) and accuracy are estimated ±5% for major elements, minor elements and trace elements (>30ppm) and ±10% for (<30) trace elements (Singh et al., 2017).

Wet chemical methods were used for the quantification of REE of 9 representative granite samples. About 1g of -200# size fine powdered sample is taken for analysis after doing and quartering for homogenization and representativeness. The samples are digested in acid media 1:1 HF- $HNO_3$ to remove the silicate phases till complete dissolutions of solid phase. The separated solution is analysed in Inductive Couple Plasma-Optical Emission Spectrometer for rare earth elements. The analytical precision and accuracy are estimated ±2-5% for major elements with >0.5% concentration and < ± 10% for trace and rare earth elements (Vimal et al., 2012).

## 7.1 GEOCHEMISTRY OF BASEMENT GRANITE

Igneous rocks have been named on the basis of mineral content, texture and composition. The formation of minerals is controlled by the composition of magma and physical-chemical condition present during the time of crystallization of the magma. Many classification schemes have been proposed for igneous rocks. Classifications based on mineralogy and texture provides important information about the origin and history of the rock. In the present study for the classification of granitoid, the whole rock geochemistry (both major and trace element data) was used. The chemical composition of granitoid rocks are generally controlled by the composition of the source rock, pressure, temperature, and degree of partial melting. Nature and extent of subsequent assimilation and differentiation processes also affect the chemistry. Hybrid composition may also result by mixing of two different parent magmas. To fulfil the objectives of present study, representative discrimination diagrams were used, are discussed below.

### 7.1.1 Geochemical characters of Basement granite:

**Major Oxides**

The granite samples show wide variation in $SiO_2$ (64.39-80.79%. avg. 72.30%), $Al_2O_3$ (11.50-19.30%, avg. 13.07), $K_2O$ (2.69-9.25%; avg. 5.99%), $Na_2O$ (0.24-4.78%; avg. 2.14%), low CaO (0.01-1.42%; avg. 0.23%), moderately high MgO (0.10-2.39%; avg. 0.93%), FeOt (1.32-7.26%; avg 3.42%), $TiO_2$ (0.01-0.47%; avg. 0.16%), and $P_2O_5$ (0.01-0.29%; avg. 0.06%). High Ba content (avg. 891ppm; 286-2128ppm) in the basement rock is attributed to presence of Baryte and Ba-Al silicate veins supported by EPMA studies. The total alkali content of these granites varies from 6.19-10.66% with an overall predominance of $K_2O$ over $Na_2O$ yet they show clear dominance over calcium evident from high alkali to lime ratio (5.26-300.23; avg. 70.85) suggesting the low calcic nature of the granite. Statistical evaluation of major, minor and trace element data is given in table 7.1. This granite shows similar major oxide concentrations with that of the basement granites of Koppunuru area (Singh et al., 2013) indicate the similarity in chemical characteristics of these two units. In order to understand the variation pattern of different elements with respect to differentiation Harker's Variation Plot (Harker, 1909) for major oxides (wt.%) has been used. The $TiO_2$, $Al_2O_3$, FeOt, MgO and $P_2O_5$ show a strong depletion with differentiation whereas $K_2O$, $Na_2O$ and CaO show over all negative trends. The negative correlations of these elements indicate early fractionation of plagioclases and mica and resistates (Figure.7.1).

### 7.1.2 Classification and magmatic affinity

The granite of the study area is typically exhibiting its distribution in the granite field in ($Na_2O$+$K_2O$) vs. Silica ($SiO_2$) (TAS) wt.% diagram as defined by Middlemost (1994) (Figure.7.2a). The alumina saturated nature of these granites is apparent from the A/CNK [molar Al2O3/ (CaO+$Na_2O$ +$K_2O$); Clarke, 1981] values ranging from 1.05-2.12 (avg. 1.51). The dominant peraluminous behaviour of these granites is ascertained by the presence of normative corundum in all samples; with volume percentage ranging from 0.086%-9.60%, avg. 4.89% and also corroborated with petrological studies as most of the samples has biotite >5% total bulk. This behaviour is further confirmed by alumina saturation diagram (A/CNK vs. A/NK) proposed by Shand (1943); discriminates between metaluminous, peralkaline and peraluminous compositions. The analysed values of granitoids are plotted in this diagram and they are fall in the peraluminous field (Figure. 7.2b) with Alumina Saturation Index 1.05-2.12 (avg. 1.51). In terms of the #Fe (Fe number; #Fe= FeOt/FeOt +MgO) this granite is magnesian (#Fe-0.47-0.86, avg. 0.70) (Frost et al., 2001) (Figure.7.2c) and predominantly fall in alkali-calcic to alkali field in MALI vs. SiO2 diagram (Frost et al., 2001) (Figure.7.2d). The high alkali nature of this granite is indicating to addition of K from outside the system. Pearce et al, (1984) used combinations of trace elements such as Nb vs Y and Rb vs (Y+Nb) to distinguish the tectonic settings of granitoids, almost all the samples of the area plot in syncollisional tectonic settings (Rb vs Y+Nb) while volcanic arc + syncollisional in (Nb vs Y) plot (Figure.7.2e.).

This granitoid shows normal (moderately) differentiated trend when plotted in Rb-Ba-Sr diagram (El Bouseily and El Sokkary (1975) which is in accordance with high Rb/Sr ratio (Figure.7.2f).

The predominance of Rb over Sr (avg. Rb/Sr ratio-20.75), relatively low CaO and Sr, high $SiO_2$, $K_2O$, $Al_2O_3$ and Rb, high average differentiation index (88.73), normative corundum (CIPW) >1% (avg.4.89) and syn-collisional tectonic settings indicate their S-type signature.

### 7.1.3 REE Distribution

The basement granite of Sarangapalli-Madinapadu area exhibit moderate to high REE distribution pattern (avg. ΣREE: 256 ppm) when compare to Clarke's value (Clarke, 1924). These granites have indicated predominance of LREE over HREE (LREE/ HREE: 3.40–45.82), which is also corroborated by chondrite normalised REE pattern (after, Boynton, 1984) (Figure.7.3). Furthermore, these granitoids are characterized by strong fractionation of the LREE from the HREE, as displayed by the high chondrite normalized ratios of $(La/Lu)_N$ and $(Ce/Yb)_N$ ranging from 6.61 to 358 and 2.15 to 68.98 respectively (Table 7.4). This can be attributed to the presence of allanite and apatite (confirmed by petrographic studies) as accessory phases in felsic liquids causing depletion in the HREE. The relative distribution of LREEs and HREEs has been attributed to magmatic differentiation (Cuney and Friedrich,1987). Besides, pronounced fractionation within LREE attributed by $(La/Sm)_N$ ratios of 1.21–8.68, chondrite normalized plot area shows moderately sloping LREE and HREE pattern with strong negative Eu anomaly (Figure.7.3). Negative Eu anomaly ($Eu/Eu^* = 0.217$-0.53), suggesting removal of plagioclase during fractional crystallization (Neiva, 1992; Chappel et al., 1987). There is not much difference observed in REE pattern of mineralized and non-mineralized portions of basement granite of Sarangapalli area (Figure.7.3).

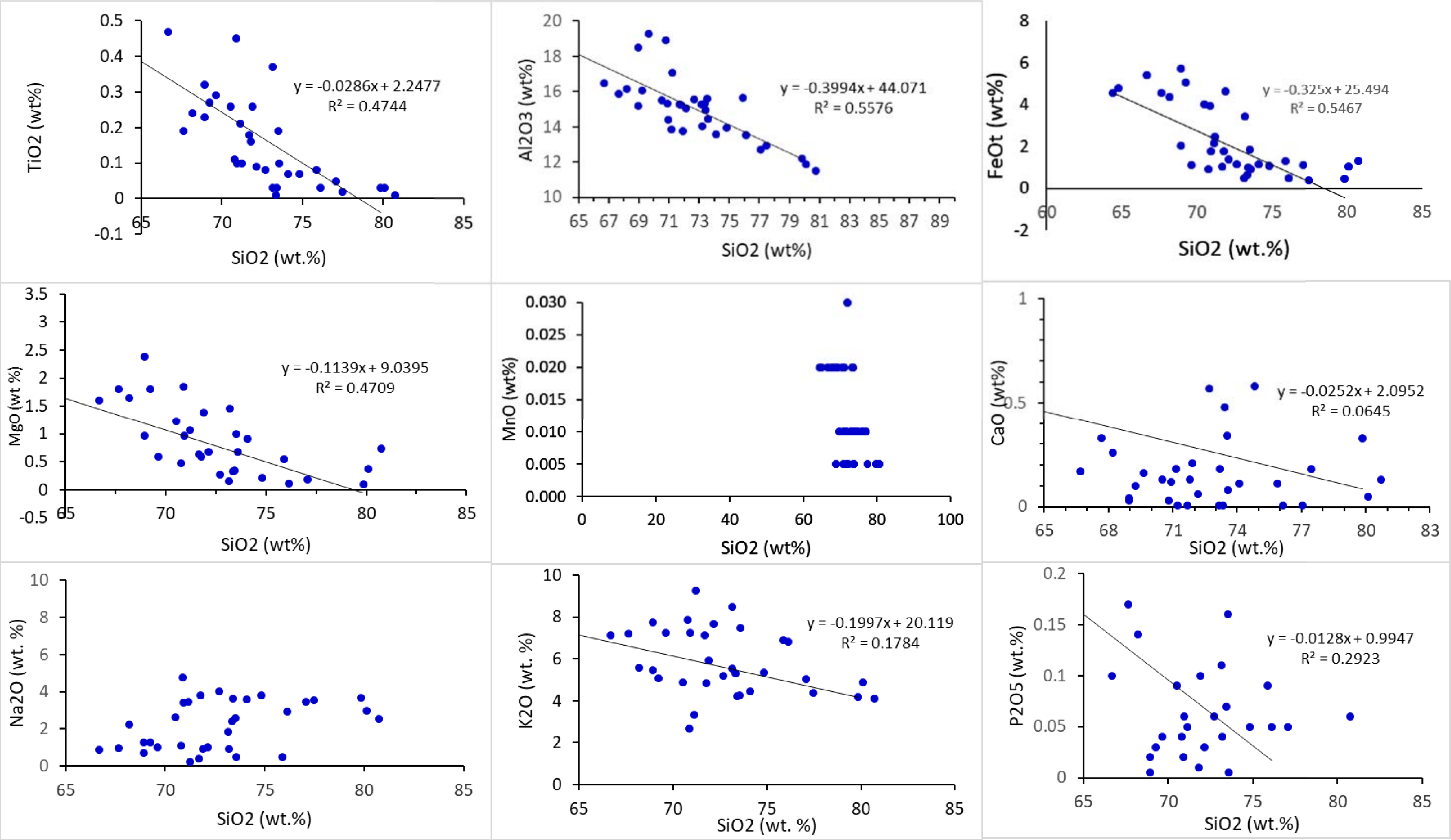

Figure.7.1 Harker's variation diagram (Harker, 1909) for major oxides (wt%) for granite of study area.

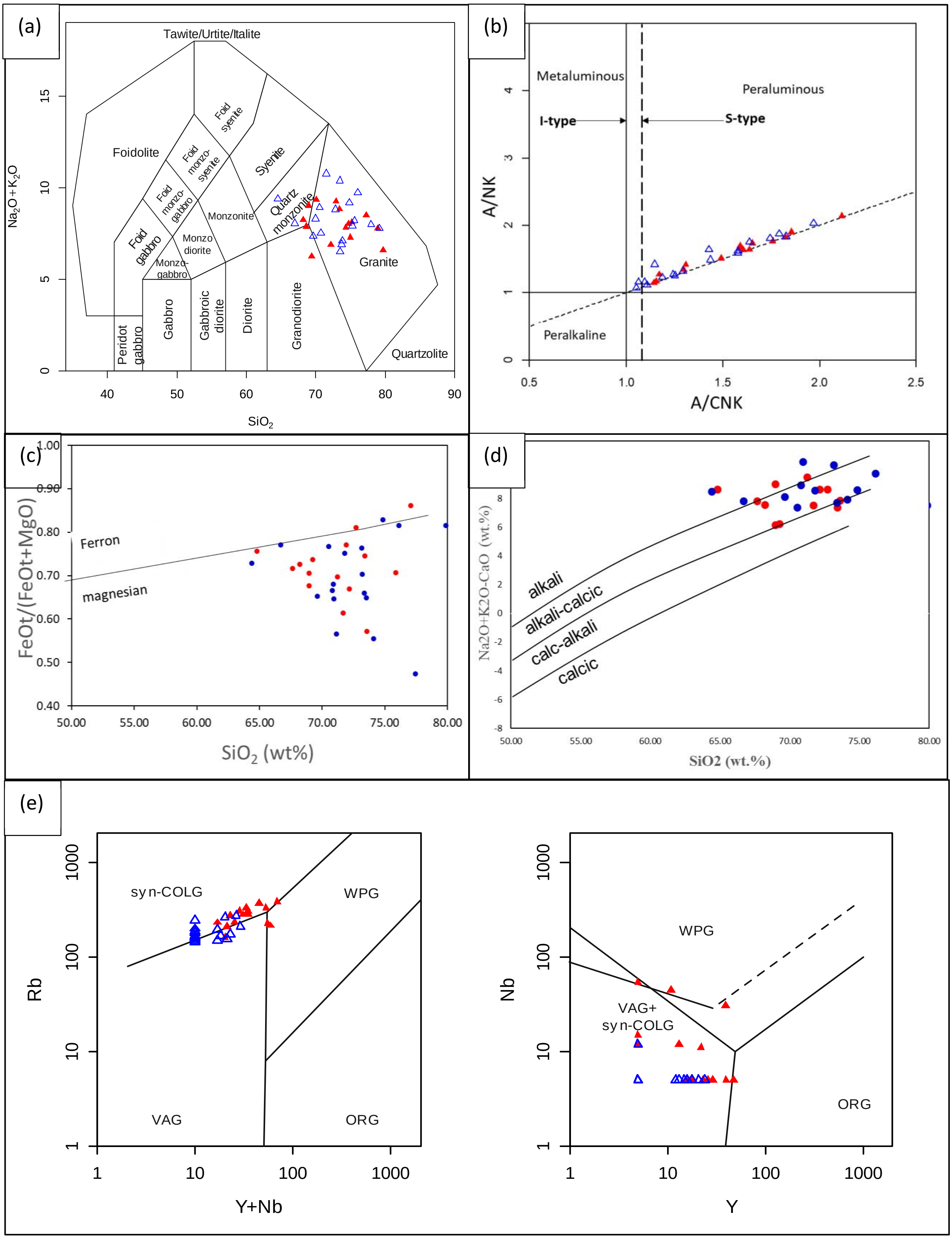

Figure.7.2 Classification of granite (a) Total alkali vs. Silica classification of granites of study area (after Middlemost, 1994). (b) A/NK vs. A/CNK plot for granites of study area (after Shand, 1943, fields after Maniar and Piccoli, 1989, and I type –S type boundary after Chappell and White, 1992). (c) #Fe vs. SiO2 plot for granites of study area (after Frost et al., 2001). (d) MALI vs. SiO2 plot for granites of study area (after Frost et al., 2001). (e) Rb- Y+ Nb & Nb-Y tectonic discrimination diagram for granites of study area (Pearce et al., 1984). Red colour, mineralized granite, blue colour, non-mineralized granite.

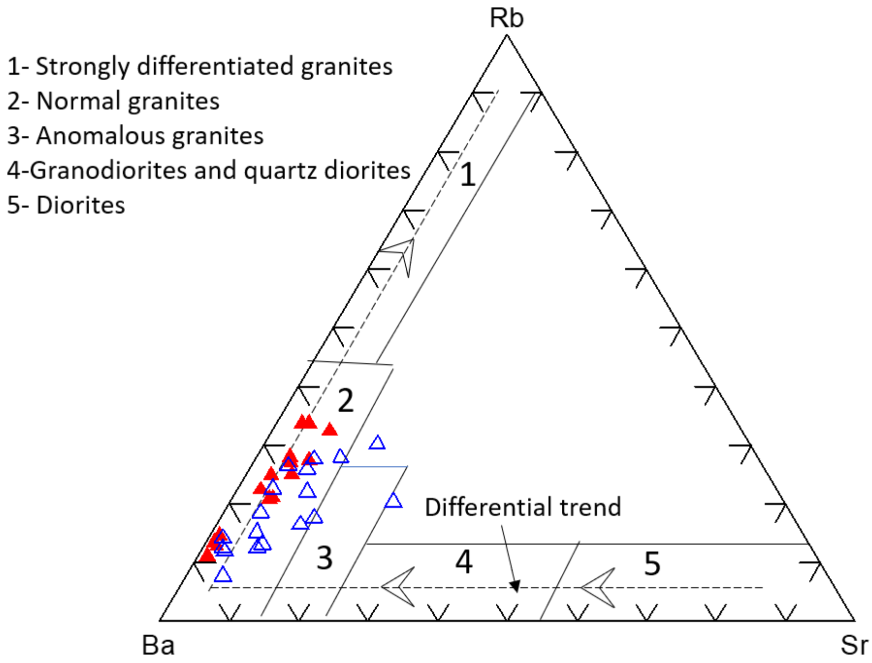

Figure.7.2 (f) Rb-Ba-Sr ternary plot for granites of study area (after El Bouseily and El Sokkary.,1975). Red colour, mineralized granite, blue colour, non-mineralized granite.

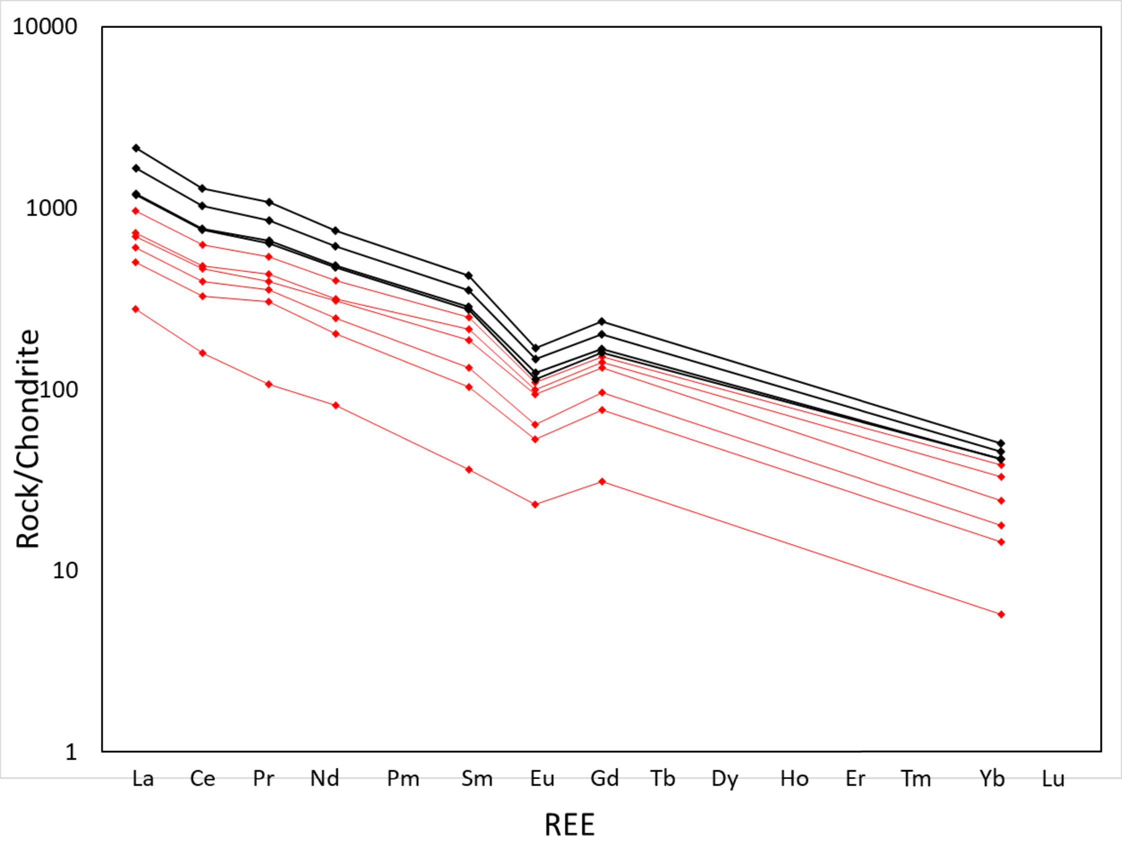

Figure.7.3 REE pattern normalised to Boynton, 1984 for the granite of Sarangapalli area (red: Uraniferous granite, black: non- uraniferous granite)

Table 7.1. Statistical evaluation and comparison of major, minor oxides (wt. %) and trace (ppm) elements of basement granite (n=35).

| Major oxides (wt. %) | Minimum | Maximum | Mean |
|---|---|---|---|
| **$SiO_2$** | 64.39 | 80.73 | 72.30 |
| **$TiO_2$** | 0.01 | 0.47 | 0.16 |
| **$Al_2O_3$** | 11.50 | 19.30 | 15.15 |
| **$Fe_2O_3$(t)** | 0.43 | 6.36 | 2.52 |
| **MgO** | 0.10 | 2.39 | 0.93 |
| **MnO** | 0.01 | 0.07 | 0.01 |
| **CaO** | 0.01 | 1.42 | 0.23 |
| **$Na_2O$** | 0.24 | 4.78 | 2.14 |
| **$K_2O$** | 2.69 | 9.25 | 5.99 |
| **$P_2O_5$** | 0.01 | 0.29 | 0.06 |
| **$K_2O/Na_2O$** | 0.56 | 38.54 | 6.03 |
| **Molar A/NK** | 1.07 | 2.57 | 1.59 |
| **Molar A/NCK** | 1.05 | 2.12 | 1.51 |
| **Agpiatic Index** | 0.39 | .0.94 | 22.97 |
| **Diff. Index** | 78.65 | 97.88 | 88.73 |
| **(%) Norm. Corundum** | 0.86 | 9.60 | 4.89 |
| **Cr** | 18 | 166 | 75 |
| **Ni** | 5 | 55 | 21 |
| **Cu** | 5s | 16 | 6 |
| **Zn** | 5 | 59 | 22 |
| **Ga** | 5 | 19 | 14 |
| **Rb** | 141 | 378 | 224 |
| **Sr** | 23 | 176 | 63 |
| **Y** | 5 | 64 | 16 |
| **Zr** | 30 | 232 | 107 |
| **Nb** | 5 | 54 | 9 |
| **Pb** | 22 | 325 | 95 |
| **Ba** | 286 | 2128 | 891 |
| **Ce** | 5 | 542 | 80 |
| **Th#** | 5 | 61 | 26 |
| **U#** | 5 | 2700 | 355 |
| **K/Rb** | 174.68 | 460.65 | 273.07 |
| **Rb/Sr** | 0.88 | 12.38 | 4.67 |
| **Ba/Sr** | 2.40 | 78.21 | 20.75 |
| **Rb/Ba** | 0.09 | 0.57 | 0.31 |

Table 7.2 Geochemical data of major, minor (in %) and trace elements (in ppm) of basement granite (mineralized).

| major oxides (%) | BH-9a | BH-9b | BH-9c | BH-9d | BH-12a | BH-14a | BH-16a | BH-16b | BH-16c | BH-16d | BH-17a | BH-19b | BH-21a | BH-21b | BH-21c | BH-21d | BH-21e |
|---|---|---|---|---|---|---|---|---|---|---|---|---|---|---|---|---|---|
| $SiO_2$ | 71.91 | 68.94 | 67.65 | 68.20 | 71.68 | 71.23 | 72.15 | 75.89 | 68.94 | 73.58 | 80.73 | 80.11 | 72.69 | 77.06 | 73.42 | 69.24 | 64.81 |
| $TiO_2$ | 0.26 | 0.23 | 0.19 | 0.24 | 0.18 | 0.10 | 0.09 | 0.08 | 0.32 | 0.10 | 0.01 | 0.03 | 0.08 | 0.05 | 0.03 | 0.27 | 0.16 |
| $Al2O_3$ | 13.75 | 15.17 | 15.87 | 16.17 | 15.29 | 17.05 | 15.03 | 15.66 | 18.50 | 14.46 | 11.50 | 11.89 | 15.55 | 12.71 | 14.97 | 16.07 | 17.52 |
| $Fe2O_3$ | 5.17 | 6.36 | 5.05 | 4.86 | 1.13 | 2.74 | 1.53 | 1.47 | 2.26 | 1.01 | 1.46 | 1.14 | 1.28 | 1.24 | 1.11 | 5.62 | 5.33 |
| MgO | 1.38 | 2.39 | 1.80 | 1.65 | 0.64 | 1.07 | 0.68 | 0.55 | 0.97 | 0.68 | 0.74 | 0.37 | 0.27 | 0.18 | 0.34 | 1.80 | 1.55 |
| MnO | 0.03 | 0.02 | 0.02 | 0.02 | 0.01 | 0.01 | 0.01 | 0.01 | 0.01 | 0.01 | 0.01 | 0.01 | 0.01 | 0.01 | 0.01 | 0.02 | 0.02 |
| CaO | 0.21 | 0.04 | 0.33 | 0.26 | 0.01 | 0.01 | 0.06 | 0.11 | 0.03 | 0.08 | 0.13 | 0.05 | 0.57 | 0.01 | 0.48 | 0.10 | 0.46 |
| $Na_2O$ | 0.93 | 0.71 | 0.97 | 2.25 | 0.40 | 0.24 | 1.01 | 0.48 | 1.27 | 0.48 | 2.53 | 2.99 | 4.03 | 3.45 | 3.65 | 1.28 | 0.47 |
| $K_2O$ | 5.92 | 5.48 | 7.19 | 5.56 | 7.13 | 9.25 | 7.67 | 6.89 | 7.74 | 7.46 | 4.12 | 4.89 | 5.18 | 5.02 | 4.22 | 5.06 | 8.61 |
| $P_2O_5$ | 0.10 | 0.02 | 0.17 | 0.14 | 0.01 | 0.01 | 0.03 | 0.09 | 0.01 | 0.01 | 0.06 | 0.01 | 0.06 | 0.05 | 0.07 | 0.03 | 0.28 |
| $K_2O/Na_2O$ | 6.37 | 7.72 | 7.41 | 2.47 | 17.83 | 38.54 | 7.59 | 14.35 | 6.09 | 15.54 | 1.63 | 1.64 | 1.29 | 1.46 | 1.16 | 3.95 | 18.32 |
| Molar A/NK | 1.73 | 2.14 | 1.69 | 1.66 | 1.83 | 1.64 | 1.51 | 1.90 | 1.77 | 1.63 | 1.33 | 1.16 | 1.27 | 1.42 | 2.57 | 2.12 | 1.74 |
| Molar A/NCK | 1.65 | 2.12 | 1.59 | 1.59 | 1.82 | 1.64 | 1.49 | 1.85 | 1.76 | 1.60 | 1.30 | 1.15 | 1.17 | 1.31 | 1.60 | 2.07 | 1.60 |
| Agpiatic Index | 0.58 | 0.47 | 0.59 | 0.60 | 0.55 | 0.61 | 0.66 | 0.53 | 0.57 | 0.61 | 0.75 | 0.86 | 0.79 | 0.71 | 0.39 | 0.47 | 0.58 |
| Diff. Index | 84.48 | 78.65 | 82.29 | 83.12 | 86.64 | 89.54 | 89.75 | 90.70 | 86.93 | 89.22 | 94.80 | 97.57 | 92.69 | 96.38 | 90.53 | 80.36 | 81.48 |
| (%) Norm. Corundum | 5.60 | 8.04 | 6.30 | 6.31 | 6.91 | 6.64 | 5.03 | 7.41 | 7.99 | 5.46 | 2.79 | 1.60 | 2.42 | 1.60 | 3.69 | 8.38 | 7.26 |
| **Trace element (ppm)** | | | | | | | | | | | | | | | | | |
| Cr | 120 | 122 | 121 | 114 | 65 | 96 | 166 | 122 | 95 | 105 | 125 | 87 | 115 | 155 | 151 | 79 | 99 |
| Ni | 55 | 22 | 33 | 30 | 5 | 12 | 5 | 44 | 22 | 10 | 16 | 5 | 28 | 53 | 28 | 23 | 31 |
| Cu | <10 | <10 | <10 | <10 | <10 | <10 | <10 | <10 | <10 | <10 | <10 | <10 | <10 | <10 | <10 | 13 | 16 |
| Zn | 50 | 40 | 41 | 47 | <10 | <10 | <10 | 21 | <10 | <10 | <10 | <10 | 24 | 24 | 21 | 42 | 31 |
| Ga | 16 | 15 | 15 | 16 | 14 | 16 | 12 | 15 | 17 | 13 | 14 | 13 | 14 | 14 | 16 | 18 | 19 |
| Rb | 297 | 276 | 275 | 207 | 306 | 363 | 322 | 269 | 322 | 378 | 228 | 234 | 227 | 211 | 161 | - | - |
| Sr | 24 | 23 | 29 | 29 | 51 | 49 | 82 | 75 | 46 | 39 | 34 | 45 | 59 | 54 | 44 | 25 | 50 |
| Y | 29 | 29 | 26 | 16 | 23 | 40 | 48 | 18 | 22 | 39 | 5 | 13 | 11 | <10 | <10 | <10 | 64 |
| Zr | 122 | 115 | 116 | 114 | 159 | 80 | 70 | 53 | 144 | 146 | 54 | 68 | 89 | 62 | 57 | 135 | 95 |
| Nb | <10 | <10 | <10 | <10 | <10 | <10 | <10 | <10 | 11 | 30 | 12 | 12 | 44 | 54 | 15 | <10 | <10 |
| Pb | 106 | 102 | 94 | 52 | 112 | 182 | 127 | 89 | 123 | 82 | 126 | 123 | 106 | 161 | 82 | 325 | 323 |
| Ba | 1877 | 1578 | 2128 | 1373 | 732 | 659 | 587 | 631 | 920 | 700 | 753 | 579 | 620 | 743 | 555 | 1349 | 945 |
| Ce | 133 | 82 | 50 | 126 | 105 | <10 | <10 | <10 | 139 | 45 | <10 | 47 | 33 | <10 | <10 | 123 | 15 |
| Th | 40 | 38 | 18 | 36 | 59 | <10 | <10 | <10 | 37 | 28 | <10 | 20 | 18 | <10 | <10 | 29 | <10 |
| U | 656 | 623 | 284 | 108 | 147 | 979 | 593 | 49 | 195 | 879 | 520 | 775 | 537 | 560 | 163 | 2700 | 2200 |
| K/Rb | 199.33 | 198.55 | 261.45 | 268.59 | 233.01 | 254.82 | 238.20 | 256.13 | 240.37 | 197.35 | 180.70 | 208.97 | 228.19 | 237.91 | 262.11 | - | - |
| Rb/Sr | 12.38 | 12.00 | 9.48 | 7.14 | 6.00 | 7.41 | 3.93 | 3.59 | 7.00 | 9.69 | 6.71 | 5.20 | 3.85 | 3.91 | 3.66 | - | - |
| Ba/Sr | 78.21 | 68.61 | 73.38 | 47.34 | 14.35 | 13.45 | 7.16 | 8.41 | 20.00 | 17.95 | 22.15 | 12.87 | 10.51 | 13.76 | 12.61 | 53.96 | 18.90 |
| Rb/Ba | 0.16 | 0.17 | 0.13 | 0.15 | 0.42 | 0.55 | 0.55 | 0.43 | 0.35 | 0.54 | 0.30 | 0.40 | 0.37 | 0.28 | 0.29 | - | - |
| FeOt+MgO+MnO+TiO2 | 6.84 | 9.00 | 7.06 | 6.77 | 1.96 | 3.92 | 2.31 | 2.11 | 3.56 | 1.80 | 2.22 | 1.55 | 1.64 | 1.48 | 1.49 | 7.71 | 7.06 |

Table 7.3 Geochemical data of major, minor (in %) and trace elements (in ppm) of basement granite (non-mineralized).

| major oxides (%) | BH-1a | BH-9e | BH-9f | BH-9g | BH-12b | BH-12c | BH-12d | BH-14b | BH-14c | BH-14d | BH-17b | BH-16a | BH-19c | BH-21f | BH-21g | BH-22a | BH-23a | BH-24b |
|---|---|---|---|---|---|---|---|---|---|---|---|---|---|---|---|---|---|---|
| $SiO_2$ | 77.5 | 71.15 | 73.53 | 70.93 | 70.79 | 69.63 | 73.35 | 66.68 | 64.39 | 73.18 | 71.79 | 73.14 | 70.52 | 76.13 | 74.83 | 70.88 | 74.10 | 79.85 |
| $TiO_2$ | 0.02 | 0.21 | 0.19 | 0.10 | 0.11 | 0.29 | 0.01 | 0.47 | 0.31 | 0.37 | 0.16 | 0.03 | 0.26 | 0.03 | 0.07 | 0.45 | 0.07 | 0.03 |
| $Al_2O_3$ | 12.9 | 13.87 | 15.58 | 14.40 | 18.91 | 19.30 | 15.32 | 16.48 | 17.77 | 14.04 | 15.23 | 15.29 | 15.52 | 13.51 | 13.95 | 15.31 | 13.58 | 12.20 |
| $Fe_2O_3$ | 0.43 | 2.39 | 2.05 | 1.95 | 1.04 | 1.23 | 0.71 | 6.01 | 5.06 | 3.84 | 1.98 | 0.54 | 4.48 | 0.54 | 1.18 | 4.38 | 1.26 | 0.49 |
| MgO | 0.43 | 1.65 | 1.00 | 0.96 | 0.47 | 0.59 | 0.33 | 1.61 | 1.70 | 1.46 | 0.59 | 0.15 | 1.22 | 0.11 | 0.22 | 1.85 | 0.91 | 0.10 |
| MnO | 0.01 | 0.02 | 0.02 | 0.01 | 0.01 | 0.01 | 0.01 | 0.02 | 0.02 | 0.02 | 0.01 | 0.01 | 0.02 | 0.01 | 0.01 | 0.07 | 0.01 | 0.01 |
| CaO | 0.18 | 0.18 | 0.34 | 0.12 | 0.03 | 0.16 | 0.01 | 0.17 | 0.88 | 0.18 | 0.13 | 0.01 | 0.13 | 0.01 | 0.58 | 1.42 | 0.11 | 0.33 |
| $Na_2O$ | 3.55 | 3.47 | 2.59 | 3.43 | 1.09 | 1.01 | 2.39 | 0.86 | 1.28 | 0.91 | 3.82 | 1.83 | 2.62 | 2.92 | 3.81 | 4.78 | 3.58 | 3.67 |
| $K_2O$ | 4.36 | 3.35 | 4.28 | 7.23 | 7.86 | 7.25 | 5.32 | 7.14 | 8.08 | 5.55 | 4.85 | 8.49 | 4.88 | 6.81 | 5.36 | 2.69 | 4.46 | 4.17 |
| $P_2O_5$ | 0.01 | 0.05 | 0.16 | 0.06 | 0.04 | 0.04 | 0.01 | 0.10 | 0.29 | 0.04 | 0.01 | 0.11 | 0.09 | 0.05 | 0.05 | 0.02 | 0.01 | 0.01 |
| $K_2O/Na_2O$ | 1.23 | 0.97 | 1.65 | 2.11 | 7.21 | 7.18 | 2.23 | 8.30 | 6.31 | 6.10 | 1.27 | 4.64 | 1.86 | 2.33 | 1.41 | 0.56 | 1.25 | 1.14 |
| Molar A/NK | 1.22 | 1.49 | 1.75 | 1.07 | 1.84 | 2.03 | 1.58 | 1.80 | 1.64 | 1.87 | 1.32 | 1.25 | 1.62 | 1.11 | 1.16 | 1.42 | 1.27 | 1.16 |
| Molar A/NCK | 1.19 | 1.44 | 1.64 | 1.05 | 1.83 | 1.97 | 1.58 | 1.74 | 1.43 | 1.79 | 1.29 | 1.25 | 1.58 | 1.11 | 1.06 | 1.15 | 1.24 | 1.09 |
| Agpiatic Index | 0.82 | 0.67 | 0.57 | 0.94 | 0.54 | 0.49 | 0.63 | 0.55 | 0.61 | 0.53 | 0.76 | 0.80 | 0.62 | 0.90 | 0.87 | 0.70 | 0.79 | 0.86 |
| Diff. Index | 94.9 | 84.61 | 87.54 | 93.55 | 89.35 | 86.30 | 90.27 | 81.35 | 81.01 | 84.70 | 90.87 | 95.45 | 85.78 | 97.88 | 94.65 | 83.39 | 91.29 | 97.41 |
| (%) Norm. Corundum | 2.04 | 4.33 | 6.45 | 0.86 | 8.61 | 9.60 | 5.63 | 7.27 | 6.01 | 6.30 | 3.48 | 3.09 | 5.91 | 1.34 | 0.95 | 2.00 | 2.68 | 1.06 |
| Trace element (ppm) | | | | | | | | | | | | | | | | | | |
| Cr | 37 | 43 | 41 | 44 | 41 | 52 | 33 | 18 | 38 | 29 | 42 | 45 | 45 | 38 | 28 | 50 | 41 | 35 |
| Ni | <10 | <10 | 22 | 29 | 24.00 | 22 | <10 | 21 | 17 | 35 | <10 | 34 | <10 | 29 | 26 | 10 | <10 | <10 |
| Cu | <10 | <10 | <10 | <10 | <10 | <10 | <10 | <10 | <10 | <10 | <10 | <10 | <10 | <10 | <10 | <10 | <10 | <10 |
| Zn | <10 | <10 | 26 | 20 | 30 | 29 | <10 | 48 | 43 | 43 | 5 | 12 | <10 | 16 | 21 | 59 | <10 | <10 |
| Ga | <10 | 15 | 17 | 14 | 16 | 17 | 13 | 13 | 13 | 14 | 14 | 11 | <10 | 13 | 14 | 15 | 14 | 13 |
| Rb | 187 | 141 | 150 | 180 | 264 | 273 | 196 | 155 | 206 | 170 | 163 | 238 | 168 | 190 | 149 | 154 | 160 | 162 |
| Sr | 126 | 86 | 94 | 75 | 57 | 53 | 62 | 34 | 58 | 24 | 124 | 72 | 48 | 82 | 68 | 176 | 116 | 86 |
| Y | <10 | <10 | 12 | <10 | 15 | 21 | <10 | 16 | 24 | 18 | 13 | <10 | <10 | <10 | <10 | <10 | <10 | <10 |
| Zr | 78 | 121 | 140 | 41 | 99 | 150 | 62 | 216 | 232 | 229 | 113 | 30 | 113 | 64 | 75 | 116 | 143 | 58 |
| Nb | <10 | <10 | <10 | <10 | <10 | <10 | <10 | <10 | <10 | <10 | <10 | <10 | <10 | 12 | <10 | <10 | <10 | 5 |
| Pb | 35 | 40 | 67 | 53 | 110 | 55 | 55 | 27 | 32 | 22 | 51 | 70 | 25 | 102 | 126 | 32 | 42 | 68 |
| Ba | 2084 | 833 | 952 | 928 | 841 | 701 | 495 | 1039 | 1462 | 998 | 638 | 548 | 691 | 408 | 455 | 423 | 691 | 286 |
| Ce | 38 | 127 | 68 | <10 | 21 | 28 | 50 | 432 | 542 | 130 | 80 | 12 | 97 | <10 | 39 | 58 | 71 | 64 |
| Th | 40 | 45 | 26 | <10 | 29 | 13 | 43 | 43 | 39 | 61 | 38 | <10 | 44 | <10 | 17 | 26 | 47 | 32 |
| U | 35 | 38 | 41 | <10 | 21 | 48 | 25 | 16 | <10 | 16 | 15 | <10 | 25 | 96 | 11 | 17 | 10 | 28 |
| K/Rb | 233 | 237.5 | 285.3 | 401.6 | 297.7 | 265.5 | 271.4 | 460.6 | 392.2 | 326.4 | 297.5 | 356. | 290.4 | 358.4 | 359.7 | 174.6 | 278.7 | 257.4 |
| Rb/Sr | 1.48 | 1.64 | 1.60 | 2.40 | 4.63 | 5.15 | 3.16 | 4.56 | 3.55 | 7.08 | 1.31 | 3.31 | 3.50 | 2.32 | 2.19 | 0.88 | 1.38 | 1.88 |
| Ba/Sr | 16.5 | 9.69 | 10.13 | 12.37 | 14.75 | 13.23 | 7.98 | 30.56 | 25.21 | 41.58 | 5.15 | 7.61 | 14.40 | 4.98 | 6.69 | 2.40 | 5.96 | 3.33 |
| Rb/Ba | 0.09 | 0.17 | 0.16 | 0.19 | 0.31 | 0.39 | 0.40 | 0.15 | 0.14 | 0.17 | 0.26 | 0.43 | 0.24 | 0.47 | 0.33 | 0.36 | 0.23 | 0.57 |
| FeOt+MgO+MnO+TiO2 | 0.89 | 4.27 | 3.26 | 3.02 | 1.63 | 2.12 | 1.06 | 8.11 | 7.09 | 5.69 | 2.74 | 0.73 | 5.98 | 0.69 | 1.48 | 6.75 | 2.25 | 0.63 |

Table 7.4 Geochemical data REE, of Granite and their statistical evaluation

| | **Radioactive samples** | | | | | | **Non-radioactive samples** | | | | **Statistical evaluation** | | |
|---|---|---|---|---|---|---|---|---|---|---|---|---|---|
| **REE** | **BH-17a** | **BH-14a** | **BH-21b** | **BH-19a** | **BH-16b** | **BH-12a** | **BH-17b** | **BH-21f** | **BH-14d** | **BH-14c** | **Avg.** | **min** | **max** |
| **La** | 86 | 70 | 31 | 28 | 10 | 73 | 69 | 5 | 145 | 143 | 66 | 5 | 145 |
| **Ce** | 128 | 137 | 54 | 53 | 15 | 120 | 107 | 8 | 206 | 213 | 104.1 | 8 | 213 |
| **Pr** | 13 | 24 | <10 | <10 | <10 | 13 | 12 | <5 | 27 | 24 | 18.83 | 12 | 27 |
| **Nd** | 49 | 72 | 27 | 37 | <10 | 49 | 43 | 7 | 79 | 82 | 49.44 | 7 | 82 |
| **Sm** | 7 | 13 | <10 | 11 | <10 | <10 | <10 | <5 | 14 | 13 | 11.6 | 7 | 14 |
| **Eu** | 1.7 | 4.4 | 0.8 | 3.5 | 1.4 | 1.3 | 1 | 0.7 | 1.7 | 1.7 | 1.82 | 0.7 | 4.4 |
| **Gd** | 8 | 12 | 5 | 9 | <5 | <5 | <5 | <3 | 9 | 9 | - | - | 9 |
| **Tb** | <3 | 12 | <3 | <3 | <3 | <3 | <3 | <3 | <3 | <3 | - | - | 12 |
| **Dy** | 3 | 6 | <3 | 6 | <3 | <3 | <3 | <3 | 4 | 3 | - | - | 6 |
| **Ho** | <3 | <3 | <3 | <3 | <3 | <3 | <3 | <3 | <3 | <3 | - | - | - |
| **Er** | <3 | 7 | <3 | <3 | <3 | <3 | <3 | <3 | <3 | <3 | - | - | 7 |
| **Tm** | <3 | <3 | <3 | <3 | <3 | <3 | <3 | <3 | <3 | <3 | - | - | - |
| **Yb** | 1.2 | 1.8 | 0.7 | 1.4 | 1.8 | 1.1 | 0.6 | <0.5 | 1.1 | 0.8 | - | - | 1.8 |
| **Lu** | 0.6 | 1.1 | <0.5 | <0.5 | <0.5 | <0.5 | <0.5 | <0.5 | 0.7 | 0.8 | - | - | 1.1 |
| **ΣREE** | 303.50 | 363.30 | 136.25 | 160.15 | 53.45 | 272.65 | 247.85 | 35.20 | 493.50 | 496.30 | 256.2 | 35.2 | 496.3 |
| **ΣLREE** | 292.70 | 292.70 | 127.80 | 148.00 | 43.90 | 263.80 | 239.50 | 27.20 | 481.70 | 485.70 | 240.3 | 27.2 | 485.7 |
| **ΣHREE** | 10.80 | 30.90 | 8.45 | 13.65 | 9.55 | 8.85 | 8.35 | 8.00 | 11.80 | 10.60 | 12.1 | 8 | 30.9 |
| **ΣLREE/ΣHREE** | 27.10 | 9.47 | 15.12 | 10.84 | 4.60 | 29.81 | 28.68 | 3.40 | 40.82 | 45.82 | 21.57 | 3.4 | 45.82 |
| **(La/Lu)N** | 14.89 | 6.61 | 107.33 | 72.71 | 20.77 | 168.50 | 358.35 | 51.94 | 18.57 | 21.52 | 84.12 | 6.61 | 358 |
| **(Ce/Yb)N** | 27.59 | 19.69 | 19.95 | 9.79 | 2.16 | 28.22 | 46.13 | 68.98 | 68.87 | 48.44 | 33.98 | 2.156 | 68.98 |
| **(La/Sm)N** | 7.73 | 3.39 | 3.55 | 1.60 | 1.21 | 6.75 | 8.68 | 1.37 | 6.92 | 6.51 | 4.771 | 1.21 | 8.68 |
| **(Gd/Lu)N** | 1.66 | 1.36 | 20.72 | 27.97 | 6.46 | 6.91 | 14.92 | 19.89 | 1.40 | 1.60 | 10.29 | 1.36 | 28 |
| **(Eu/Eu*)N** | 0.35 | 0.53 | 0.23 | 0.52 | 0.52 | 0.40 | 0.39 | 0.53 | 0.23 | 0.22 | 0.391 | 0.217 | 0.53 |

## 7.2 GEOCHEMISTRY OF BANGANAPALLE QUARTZITE:

Analytical results of mineralised Banganapalle Quartzite are given in Table-5 and non-mineralized Banganapalle Quartzite are given in Table-6 and statistical evaluation of both the lithounit is given in Table-7. Synthesis of analytical data of mineralized samples indicates $SiO_2$ (71.48–97.39%; av. 85.80%) which is commensurate by high $Al_2O_3$ (2.34-16.06%; av. 8.13), $K_2O$ (1.03-8.34%, av. 2.75), $Fe_2O_3$(t) (0.36–2.92%; av. 1.33%), variable MgO (<0.010–1.21%; av. 0.36%) and $Na_2O$ (0.26-1.47%; av. 0.60). This geochemical behaviour is due to chemically sub mature and altered subfeldspathic arenite which is substantiated by petromineralogical studies. The non-mineralized samples are chemically mature and unaltered, which is commensurate by restricted high $SiO_2$(89.58–99.36%; av. 94.95%) and relatively low $Al_2O_3$ (0.25-6.58%; av. 2.08), $K_2O$ (0.03-2.3%, av. 0.91), $Na_2O$ (<0.010-0.54%; av. 0.23), $Fe_2O_3$(t) (<0.01–1.44%; av. 0.56%) and MgO (<0.010–0.33%; av. 0.17%).

For geochemical characterization of Banganapalle Quartzite (both mineralized and non-mineralized), representative discrimination diagrams were used.

The Sand Class system, based on $SiO_2/Al_20_3$ and $Fe_20_3/ K_20$ ratios (After Herron, 1988), is a useful advance in geochemical sandstone classification schemes. The uraniferous Banganapalle Quartzite (mainly basal portion, above the unconformity) is classified as arkose to subarkose while non uraniferous Banganapalle Quartzite as subarkose to quartz arenite (Figure. 7.4a) which is also evidenced by petromineralogical studies. After plotting the data in the $Al_2O_3$% versus $TiO_2$% (Figure. 7.4b) bivariate discrimination diagram (McLennan et al.,1990) to assign the provenance, is seen that samples of the present study mostly plot in the granite field and few in the alkali granite field. Inferred source rocks for Banganapalle quartzite as revealed in Zr vs $TiO_2$ plot (Figure. 7.4c) is felsic in nature (after Hayashi et al., 1997). Another bivariate $TiO_2$% versus Ni (ppm) diagram (Figure. 7.4d) to evaluate source rock composition (Floyd et al., 1989) indicate sandstone are derived from acidic igneous rocks.

In the last few decades evolution of plate tectonic theory and detailed petrographic studies of sandstones from sedimentary sequences has led to the development of a number of detrital modal discriminants aimed at determination of tectonic setting of ancient basins (Crook 1974; Dickinson and Suczek, 1979). Such studies have been complemented by similar work on modern sediments of known plate tectonic setting (e.g. Valloni and Maynard, 1981; Yerino and Maynard, 1984), and characteristic modal compositions for sandstones of differing tectonic environments are now reasonably well established. Even though diagenesis may alter original chemistry, changes are themselves related to plate tectonic environment (Siever, 1979), and bulk composition should still reflect tectonic setting and so enable development of chemically-based discriminants to supplement the petrographic approach. Crook (1974) divided greywackes into three classes and assigned each to a major plate tectonic environment. Crook's groups are:

1) Quartz-poor greywackes, with <15% framework quartz, average 58% volatile-free $SiO_2$, and $K_20/Na_20<1$. They are of basic volcanic provenance in magmatic island arcs.

2) Quartz-intermediate; 15-65% quartz, average 68-74% SiO2, and $K_2O/Na_2O<l$. Provenance is mixed, and rocks of this class are typical of evolved active continental margins.

3) Quartz-rich; >65% quartz, average 89% $SiO_2$, and $K_2O/Na_2O>1$. They are deposited at passive continental margins and in plate interior.

According to crook theory these sandstones are deposited at passive continental margins and in plate interiors with average $SiO_2$= 90.4% and $K_2O/Na_2O$> 4.89.

Bivariant plot Fe2O3+MgO vs TiO2 (Bhatia MR, 1983) (Figure.7.4e) and $SiO_2$ vs $K_2O/Na_2O$ (Roser and Korsch, 1986) (Figure.7.4f) shows passive continental margin setting of the studied Quartzite with $K_2O/Na_2O>1$ and average $SiO_2$=87.8%. Therefore, these sediments derived from passive margin tectonic settings under semi-humid to semi-arid climatic conditions, SiO2 vs Al2O3+K2O+Na2O plot (After Suttner and Dutta, 1986) (Figure. 7.4g).

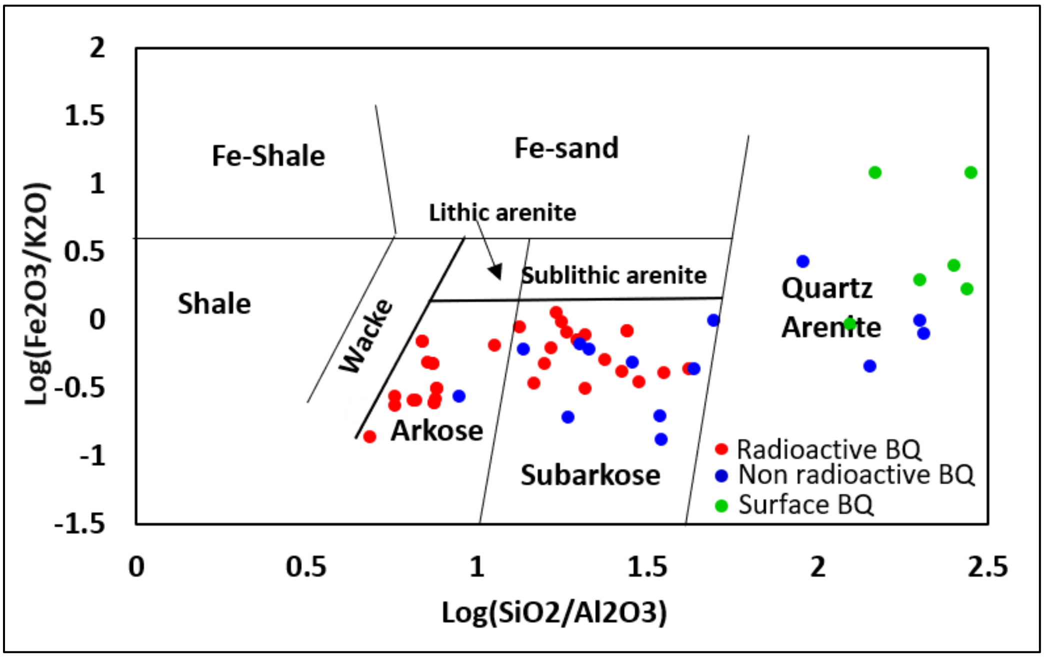

Figure. 7.4a. Log ($SiO_2/Al_2O_3$) vs Log ($Fe_2O_3/K_2O$) plot of sandstone classification Diagram (After Herron, 1988)

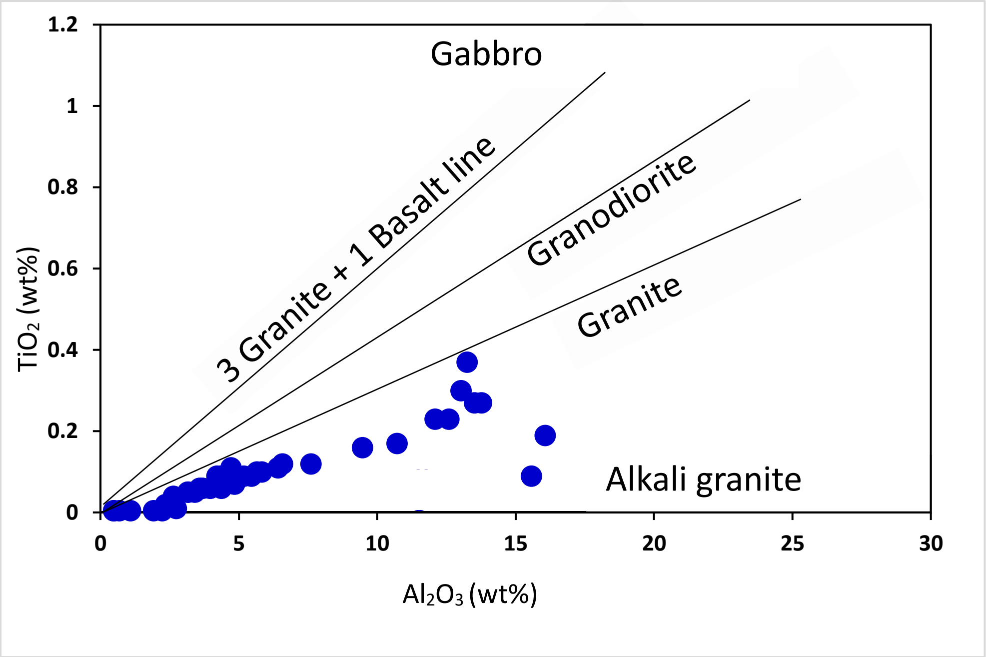

Figure. 7.4b. Provenance discrimination plot (after McLennan et al.,1979; Schieber, 1992)

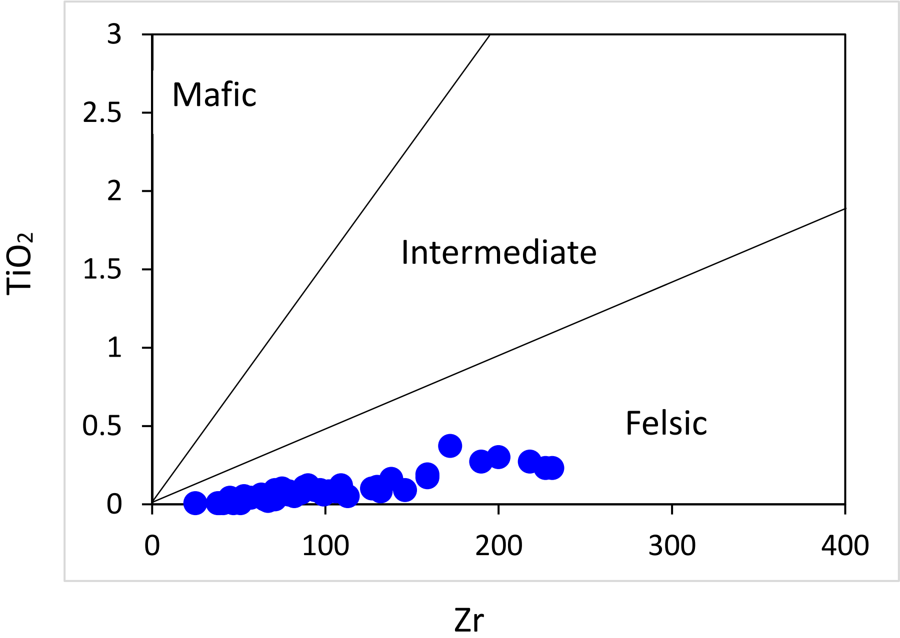

Figure. 7.4c Inferred source rocks in Zr vs. $TiO_2$ plot (after Hayashi et al., 1997)

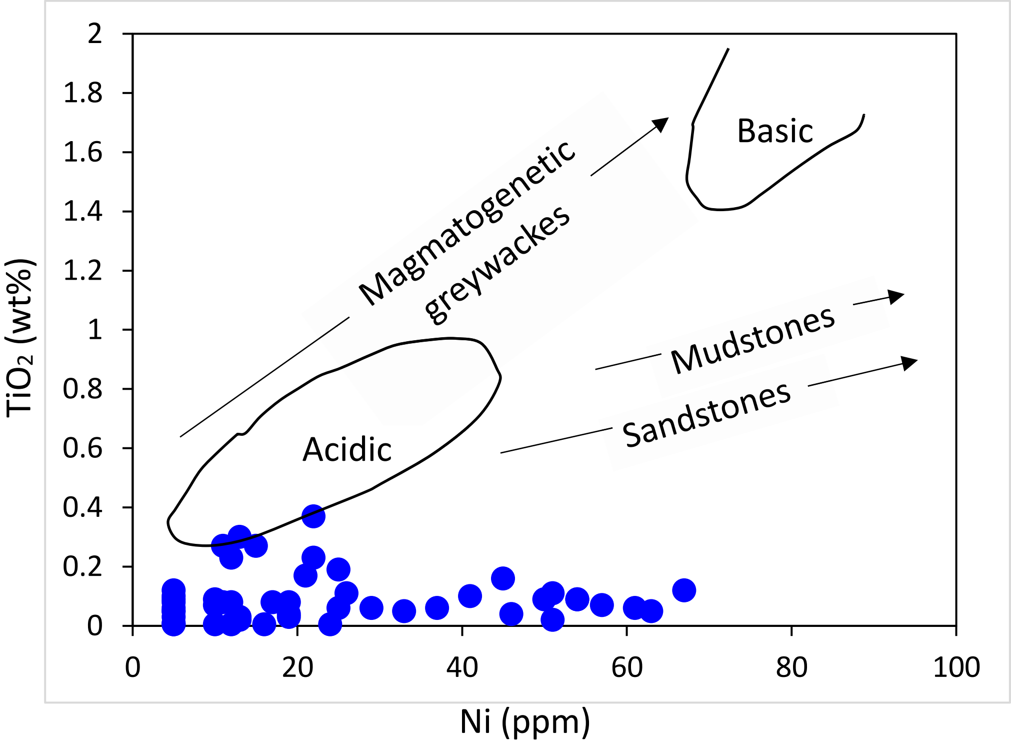

Figure. 7.4d $TiO_2$-Ni plot of the studied quartzites (after Floyd et al., 1989)

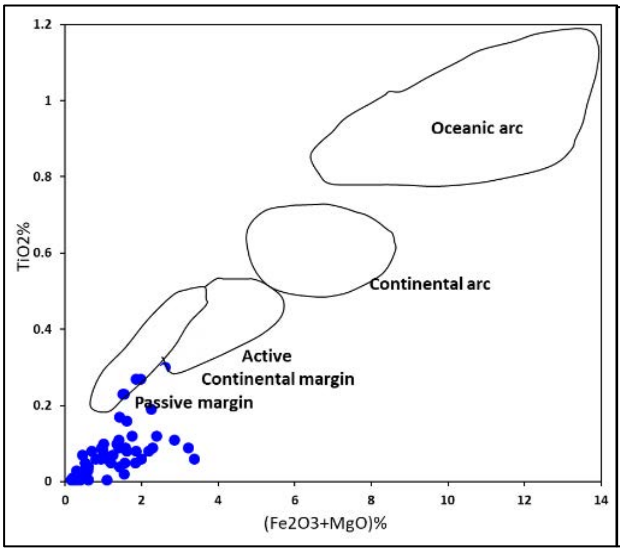

Figure.7.4e. $TiO_2$ vs $Fe_2O_3$+Mgo bivariate diagram for tectonic setting of deposition (Bhatia, M. R., 1983)

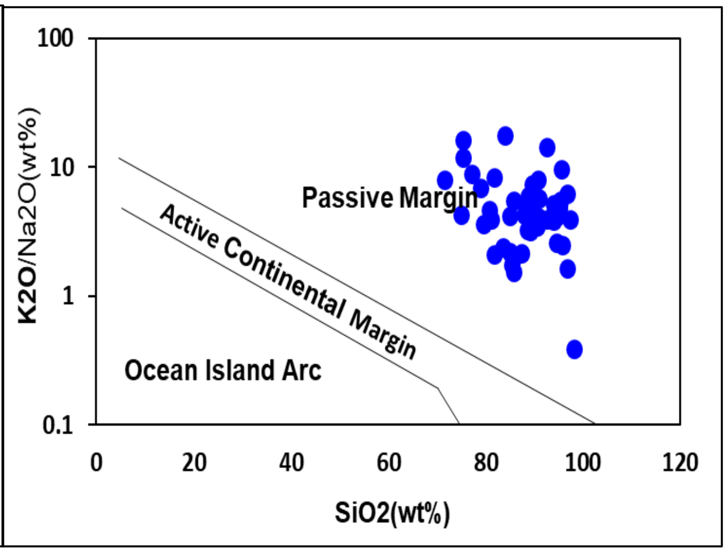

Figure.7.4f $SiO_2$ vs $K_2O/Na_2O$ plot shows passive continental margin setting of the studied Quartzite (after Roser and Korsch, 1986)

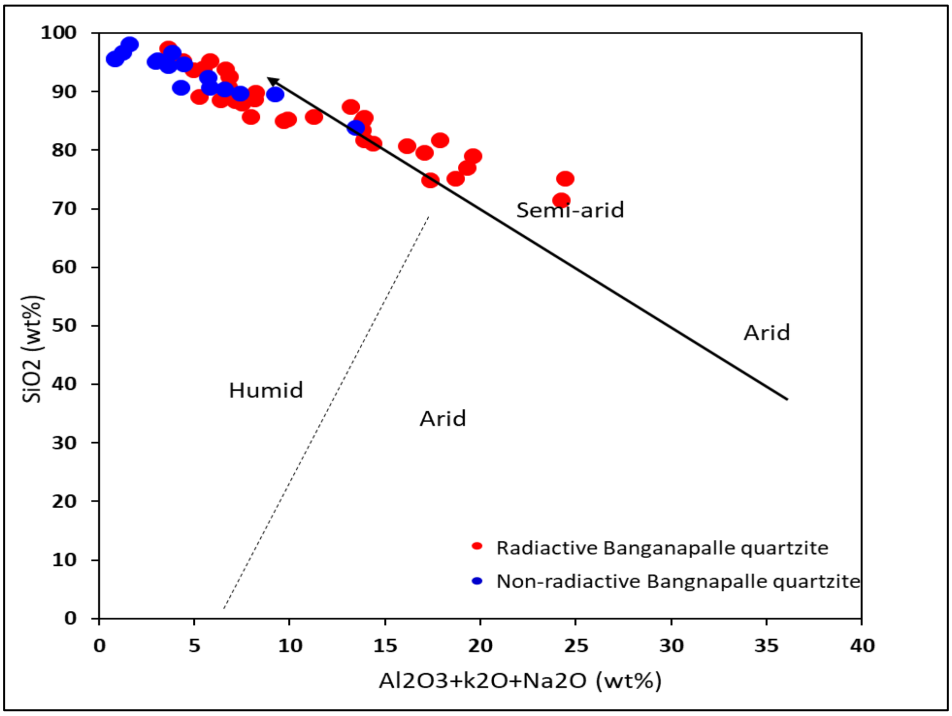

Figure. 7.4g $SiO_2$ vs $Al_2O_3$+$K_2O$+$Na_2O$ binary variation plot (After Suttner and Dutta, 1986) showing paleoweathering conditions of Banganapalle Quartzite.

Table 7.5 Geochemical data of major, minor (in %) and trace elements (in ppm) of Banganapalle Quartzite (mineralized).

| Sample | BH-9B | BH-9C | BH-12B | BH-12C | BH-12E | BH-12F | BH-12G | BH-14C | BH-14D | BH-14E | BH-14F | BH-14G | BH-14H | BH-16C | BH-16D | BH-16E | BH-17B |
|---|---|---|---|---|---|---|---|---|---|---|---|---|---|---|---|---|---|
| $SiO_2$ | 90.94 | 85.73 | 97.39 | 81.75 | 88.01 | 89.65 | 89.86 | 88.77 | 95.25 | 93.93 | 88.64 | 94.05 | 85.02 | 93.74 | 85.72 | 75.26 | 95.25 |
| $TiO_2$ | 0.06 | 0.12 | 0.02 | 0.23 | 0.09 | 0.08 | 0.09 | 0.1 | 0.03 | 0.06 | 0.09 | 0.05 | 0.11 | 0.05 | 0.08 | 0.09 | 0.06 |
| $Al_2O_3$ | 4.37 | 7.61 | 2.34 | 12.59 | 5.18 | 4.92 | 5.45 | 5.65 | 2.69 | 3.96 | 4.21 | 3.41 | 6.41 | 3.15 | 4.85 | 15.57 | 3.58 |
| $Fe_2O_3$ | 1.59 | 2.01 | 0.45 | 1.22 | 2.12 | 1.59 | 1.37 | 1.02 | 0.58 | 1.07 | 2.87 | 1.43 | 2.34 | 0.51 | 1.82 | 1.17 | 0.78 |
| MgO | 0.4 | 0.37 | <.01 | 0.28 | 0.15 | <.01 | 0.03 | 0.32 | <.01 | 0.02 | 0.35 | 0.12 | 0.5 | <.01 | 0.36 | 0.39 | <.01 |
| MnO | <0.01 | <.01 | <.01 | <.01 | 0.01 | <.01 | <.01 | 0.01 | <.01 | <.01 | 0.01 | <.01 | <.01 | <.01 | <.01 | <.01 | <.01 |
| CaO | 0.02 | <.01 | <.01 | 0.01 | 0.15 | <.01 | <.01 | 0.21 | 0.01 | <.01 | 0.24 | 0.03 | 0.1 | <.01 | <.01 | <.01 | <.01 |
| $Na_2O$ | 0.36 | 0.56 | 0.26 | 0.56 | 0.44 | 0.49 | 0.52 | 0.36 | 0.29 | 0.55 | 0.34 | 0.33 | 0.62 | 0.35 | 1.22 | 0.51 | 0.38 |
| $K_2O$ | 2.06 | 3.09 | 1.03 | 4.7 | 1.87 | 1.97 | 2.21 | 2.14 | 1.4 | 2.11 | 1.84 | 1.72 | 2.62 | 1.46 | 1.88 | 8.34 | 1.87 |
| $P_2O_5$ | 0.03 | <.01 | <.01 | <.01 | 0.02 | <.01 | <.01 | 0.03 | <.01 | <.01 | 0.05 | <.01 | <.01 | <.01 | <.01 | <.01 | <.01 |
| $K_2O/Na_2O$ | 5.72 | 5.52 | 3.96 | 8.39 | 4.25 | 4.02 | 4.25 | 5.94 | 4.83 | 3.84 | 5.41 | 5.21 | 4.23 | 4.17 | 1.54 | 16.35 | 4.92 |
| Cr | 274 | 136 | 139 | 149 | 309 | 224 | 208 | 243 | 226 | 216 | 244 | 179 | 181 | 145 | 165 | 109 | 320 |
| Ni | 37 | <10 | 13 | 22 | 50 | 11 | 10 | 41 | <10 | 29 | 54 | 33 | 26 | <10 | 19 | <10 | 25 |
| Cu | <10 | <10 | <10 | <10 | <10 | <10 | 11 | <10 | <10 | <10 | 12 | 13 | <10 | <10 | <10 | <10 | <10 |
| Zn | 20 | <10 | <10 | <10 | 46 | 46 | 10 | 20 | 2824 | 59 | 87 | 87 | 31 | <10 | <10 | <10 | <10 |
| Ga | 11 | <10 | <10 | 12 | <10 | <10 | <10 | <10 | <10 | <10 | 14 | 15 | 10 | <10 | <10 | 12 | <10 |
| Rb | 100 | 151 | 96 | 291 | 98 | 120 | 159 | 114 | 114 | 127 | - | - | 141 | 94 | 118 | 351 | 117 |
| Sr | 11 | 15 | 10 | 30 | 12 | 16 | 17 | 15 | 18 | 20 | 16 | 17 | 22 | 15 | 18 | 57 | 16 |
| Y | <10 | <10 | <10 | 41 | <10 | <10 | <10 | <10 | <10 | <10 | <10 | 11 | <10 | <10 | <10 | 32 | <10 |
| Zr | 79 | 109 | 67 | 227 | 94 | 106 | 146 | 75 | 65 | 99 | 97 | 113 | 130 | 82 | 97 | 71 | 81 |
| Nb | <10 | 10 | 33 | 16 | <10 | 23 | 30 | <10 | 32 | 20 | <10 | <10 | 31 | 13 | 19 | 11 | 11 |
| Pb | 192 | 47 | 95 | 120 | 51 | 109 | 146 | 46 | 62 | 111 | 442 | 501 | 99 | 73 | 173 | 100 | 57 |
| Ba | 750 | 982 | 180 | 479 | 122 | 282 | 199 | 516 | 337 | 341 | 493 | 467 | 416 | 192 | 221 | 583 | 217 |
| Ce | 46 | <10 | <10 | 62 | 14 | <10 | 41 | <10 | <10 | <10 | 55 | 53 | 32 | 19 | 24 | 17 | <10 |
| Th | <10 | 12 | <10 | 17 | 11 | <10 | <10 | <10 | <10 | 11 | <10 | 10 | 12 | <10 | <10 | <10 | <10 |
| U | 95 | 130 | 350 | 1179 | 108 | 281 | 562 | 96 | 351 | 265 | 4300 | 4600 | 361 | 145 | 217 | 751 | 181 |

Continuation of table 6.5…………………

| | BH-17C | BH-17D | BH-17E | BH-19A | BH-19/B | BH-19C | BH-21C | BH-21D | BH-21E | BH-21F | BH-21G | BH-21H | BH-21I | BH-21J | BH-21K | BH-22A | BH-22B |
|---|---|---|---|---|---|---|---|---|---|---|---|---|---|---|---|---|---|
| $SiO_2$ | 88.48 | 85.27 | 77.07 | 79.6 | 79 | 80.77 | 83.48 | 81.83 | 85.05 | 92.6 | 74.99 | 85.67 | 87.45 | 81.16 | 89.19 | 75.25 | 71.48 |
| $TiO_2$ | 0.08 | 0.1 | 0.27 | 0.23 | 0.27 | 0.17 | 0.06 | 0.08 | 0.08 | 0.11 | 0.3 | 0.04 | 0.03 | 0.05 | 0.06 | 0.37 | 0.19 |
| $Al_2O_3$ | 4.28 | 5.82 | 13.51 | 12.09 | 13.77 | 10.71 | 11.69 | 11.76 | 11.48 | 4.72 | 13.02 | 11.47 | 11.51 | 11.79 | 3.69 | 13.24 | 16.06 |
| $Fe_2O_3$ | 0.69 | 0.89 | 1.42 | 1 | 1.19 | 1.17 | 0.72 | 1.57 | 0.75 | 1.22 | 1.84 | 0.4 | 0.36 | 1.41 | 2.92 | 2.09 | 1.49 |
| MgO | <.01 | 0.11 | 0.54 | 0.54 | 0.66 | 0.24 | 0.21 | 0.27 | 0.23 | 0.18 | 0.77 | 0.2 | 0.12 | 0.42 | 0.45 | 1.21 | 0.75 |
| MnO | <.01 | <.01 | <.01 | <.01 | <.01 | <.01 | <.01 | <.01 | <.01 | 0.01 | <.01 | <.01 | <.01 | <.01 | 0.01 | 0.01 | 0.01 |
| CaO | <.01 | <.01 | <.01 | 0.01 | 0.13 | 0.18 | 0.2 | 0.1 | <.01 | 0.15 | <.01 | <.01 | <10 | <10 | 0.13 | <.01 | 0.03 |
| $Na_2O$ | 0.66 | 1.47 | 0.59 | 1.07 | 0.73 | 0.95 | 0.62 | 0.68 | 0.72 | 0.43 | 0.82 | 0.82 | 0.53 | 0.51 | 0.37 | 0.42 | 0.91 |
| $K_2O$ | 2.17 | 2.58 | 5.19 | 3.88 | 5.07 | 4.45 | 1.48 | 1.44 | 1.57 | 1.69 | 3.52 | 1.61 | 1.13 | 2.03 | 1.19 | 5.02 | 7.24 |
| $P_2O_5$ | <.01 | <.01 | <.01 | <.01 | <.01 | <.01 | <.01 | <.01 | <.01 | 0.01 | <.01 | <.01 | <.01 | <.01 | 0.02 | <.01 | <.01 |
| $K_2O/Na_2O$ | 3.29 | 1.76 | 8.80 | 3.63 | 6.95 | 4.68 | 2.39 | 2.12 | 2.18 | 3.93 | 4.29 | 1.96 | 2.13 | 3.98 | 3.22 | 11.95 | 7.96 |
| Cr | 283 | 195 | 148 | 142 | 149 | 89 | 172 | 104 | 172 | 272 | 123 | 153 | 156 | 153 | 237 | 125 | 140 |
| Ni | 12 | <10 | 15 | 12 | 11 | 21 | <10 | 17 | <10 | 51 | 13 | 19 | 13 | <10 | 61 | 22 | 25 |
| Cu | <10 | <10 | <10 | <10 | <10 | <10 | <10 | 11 | <10 | <10 | <10 | <10 | <10 | <10 | <10 | 10 | <10 |
| Zn | <10 | <10 | <10 | <10 | <10 | <10 | <10 | <10 | <10 | 16 | <10 | <10 | <10 | <10 | 432 | 10 | <10 |
| Ga | <10 | <10 | 10 | 10 | 11 | <10 | <10 | <10 | <10 | <10 | 10 | <10 | <10 | <10 | 10 | 13 | 11 |
| Rb | 126 | 142 | 261 | 227 | 253 | 205 | 98 | 97 | 112 | 107 | 197 | 95 | 137 | 184 | 214 | 325 | 308 |
| Sr | 23 | 25 | 30 | 26 | 28 | 23 | 15 | 14 | 15 | 12 | 13 | 14 | 12 | 15 | 12 | 30 | 63 |
| Y | <10 | <10 | 21 | 20 | 17 | 10 | <10 | <10 | <10 | <10 | 11 | 10 | <10 | <10 | <10 | 29 | 22 |
| Zr | 132 | 127 | 218 | 231 | 190 | 159 | 63 | 79 | 102 | 88 | 200 | 45 | 65 | 67 | 73 | 172 | 159 |
| Nb | 21 | 25 | 33 | 19 | 13 | 11 | 13 | 12 | 14 | 13 | 16 | <10 | <10 | <10 | 109 | 13 | <10 |
| Pb | 64 | 67 | 89 | 69 | 111 | 62 | 65 | 79 | 51 | 55 | 61 | 42 | 110 | 209 | 287 | 45 | 53 |
| Ba | 283 | 272 | 534 | 440 | 529 | 498 | 705 | 111 | 517 | 552 | 1190 | 501 | 411 | 668 | 388 | 1238 | 1110 |
| Ce | 34 | 13 | 35 | <10 | 69 | <10 | <10 | 56 | <10 | 10 | <10 | <10 | <10 | <10 | 42 | 11 | 56 |
| Th | 13 | <10 | 23 | 19 | 18 | 22 | <10 | 10 | <10 | 10 | 22 | <10 | <10 | 376 | <10 | 31 | 46 |
| U | 298 | 282 | 382 | 240 | 154 | 155 | 122 | 150 | 161 | 136 | 236 | 63 | 726 | 814 | 1180 | 252 | 70 |

Table 7.6 Geochemical data of major, minor (in %) and trace elements (in ppm) of Banganapalle Quartzite (non-mineralized).

| | Banganapalle Quartzite (subsurface data) | | | | | | | | | | | | | | | | Banganapalle quartzite (surface samples) | | | | | |
|---|---|---|---|---|---|---|---|---|---|---|---|---|---|---|---|---|---|---|---|---|---|---|
| Sample | BH-1A | BH-9A | BH-12A | BH-12D | BH-14A | BH-14B | BH-16A | BH-16B | BH-17A | BH-19D | BH-21A | BH-21B | BH-22C | BH-23A | BH-24A | BH-25A | SPL-1 | SPL-2 | SPL-3 | SPL-4 | SPL-5 | SPL-6 |
| $SiO_2$ | 95.69 | 96.78 | 96.74 | 90.79 | 94.67 | 92.49 | 89.58 | 90.46 | 90.8 | 89.72 | 95.4 | 94.47 | 95.54 | 95.22 | 98.09 | 96.53 | 95.6 | 96.2 | 99 | 99.38 | 98.6 | 97.07 |
| $TiO_2$ | <.01 | <.01 | <.01 | 0.05 | 0.01 | 0.09 | 0.12 | 0.07 | 0.03 | 0.07 | 0.02 | 0.04 | <.01 | <.01 | <.01 | <.01 | <0.01 | <0.01 | <10 | <0.01 | <0.01 | <0.01 |
| $Al_2O_3$ | 0.47 | 2.23 | 0.68 | 3.17 | 2.74 | 4.33 | 6.58 | 4.54 | 2.65 | 4.84 | 2.43 | 2.63 | 0.48 | 1.92 | 1.09 | 2.18 | 0.25 | 0.32 | 0.32 | 0.8 | 0.36 | 0.66 |
| $Fe_2O_3$ | 0.2 | 0.6 | 0.15 | 1.04 | 0.18 | 0.79 | 1.41 | 1.07 | 0.29 | 0.43 | 1.44 | 1.2 | 0.29 | 0.87 | 0.38 | 0.23 | 0.34 | 0.35 | 0.15 | 0.25 | 0.29 | 0.3 |
| MgO | <.01 | <.01 | <.01 | 0.14 | <.01 | 0.16 | 0.33 | 0.17 | <.01 | 0.01 | 0.1 | 0.22 | <.01 | 0.21 | <.01 | <.01 | <0.01 | <0.01 | <0.01 | <0.01 | <0.01 | <0.01 |
| MnO | <.01 | <.01 | <.01 | 0.01 | <.01 | 0.01 | 0.01 | 0.01 | <.01 | <.01 | 0.01 | 0.01 | <.01 | <.01 | <.01 | <.01 | <0.01 | <0.01 | <0.01 | <0.01 | <0.01 | <0.01 |
| CaO | 0.12 | <.01 | <.01 | 0.14 | 0.01 | 0.12 | 0.21 | 0.15 | <.01 | <.01 | 0.005 | 0.01 | 0.74 | <.01 | <.01 | 0.55 | <0.01 | 0.06 | <0.01 | <0.0 | <0.01 | <0.01 |
| $Na_2O$ | 0.1 | 0.22 | 0.2 | 0.52 | 0.32 | 0.09 | 0.31 | 0.46 | 0.18 | 0.34 | 0.1 | 0.28 | 0.03 | 0.16 | 0.36 | 0.54 | 0.04 | <0.01 | <0.01 | 0.14 | <0.01 | 0.03 |
| $K_2O$ | 0.25 | 1.36 | 0.33 | 2.12 | 1.35 | 1.29 | 2.3 | 1.59 | 1.45 | 2.21 | 0.55 | 0.73 | 0.29 | 0.87 | 0.14 | 0.78 | 0.03 | <0.01 | 0.06 | 0.27 | 0.17 | <0.01 |
| $P_2O_5$ | <.01 | <.01 | <.01 | 0.03 | <.01 | 0.02 | 0.03 | 0.01 | <.01 | <.01 | 0.01 | 0.02 | <.01 | <.01 | <.01 | <.01 | <0.01 | 0.1 | <0.01 | <0.01 | <0.01 | <0.01 |
| $K_2O/Na_2O$ | 2.5 | 6.2 | 1.7 | 4.1 | 4.2 | 14.3 | 7.4 | 3.5 | 8.1 | 6.5 | 5.5 | 2.6 | 9.7 | 5.4 | 0.4 | 1.4 | 0.8 | | | 1.9 | | |
| Cr | 47 | 47 | 43 | 104 | 63 | 96 | 257 | 237 | 46 | 44 | 86 | 78 | 49 | 45 | 56 | 48 | 44 | 70 | 57 | 59 | 50 | 53 |
| Ni | 24 | <10 | <10 | 63 | <10 | 54 | 67 | 57 | 19 | 10 | 51 | 46 | 10 | 12 | 16 | <10 | 14 | 11 | 23 | 10 | <10 | 20 |
| Cu | <10 | <10 | <10 | 11 | <10 | <10 | <10 | <10 | <10 | <10 | 12 | <10 | <10 | <10 | <10 | <10 | <10 | <10 | <10 | <10 | <10 | <10 |
| Zn | <10 | <10 | <10 | 14 | <10 | 14 | 17 | 18 | <10 | <10 | 36 | 49 | <10 | <10 | <10 | <10 | <10 | <10 | <10 | <10 | <10 | <10 |
| Ga | <10 | <10 | <10 | <10 | <10 | <10 | 10 | <10 | <10 | <10 | <10 | <10 | <10 | <10 | <10 | <10 | <10 | <10 | <10 | <10 | <10 | <10 |
| Rb | 33 | 68 | 37 | 68 | 64 | 80 | 126 | 88 | 74 | 119 | 34 | 42 | 38 | 48 | 36 | 47 | 27 | 26 | 28 | 36 | 37 | 23 |
| Sr | 15 | 14 | <10 | <10 | 16 | <10 | 17 | 14 | 15 | 18 | <10 | <10 | 10 | 11 | <10 | 48 | <10 | 21 | <10 | <10 | <10 | <10 |
| Y | <10 | <10 | <10 | <10 | <10 | <10 | <10 | <10 | <10 | <10 | <10 | <10 | <10 | <10 | <10 | <10 | <10 | <10 | <10 | <10 | <10 | <10 |
| Zr | 39 | 51 | 38 | 53 | 49 | 76 | 90 | 86 | 71 | 100 | 47 | 57 | 41 | 47 | 25 | 51 | 38 | 46 | 51 | 42 | <10 | 48 |
| Nb | <10 | <10 | <10 | <10 | <10 | <10 | <10 | <10 | <10 | <10 | <10 | <10 | <10 | <10 | <10 | <10 | <10 | <10 | <10 | <10 | <10 | <10 |
| Pb | 16 | 33 | 20 | 49 | 14 | 27 | 31 | 63 | 24 | 31 | 20 | 24 | 16 | 17 | 21 | 15 | 23 | 13 | 13 | 17 | 15 | 11 |
| Ba | 2865 | 461 | 92 | 148 | 386 | 232 | 282 | 173 | 227 | 292 | 309 | 165 | 439 | 1213 | 184 | 2934 | 1038* | 872* | 262 | 228 | 980* | 179 |
| Ce | <10 | <10 | <10 | 13 | <10 | 26 | <10 | 19 | 15 | <10 | <10 | <10 | <10 | <10 | 17 | <10 | <10 | <10 | <10 | 26 | <10 | <10 |
| Th | <10 | 18 | <10 | <10 | <10 | <10 | <10 | 11 | <10 | 48 | <10 | <10 | 12 | <10 | 10 | <10 | <10 | <10 | <10 | <10 | <10 | <10 |
| U | <10 | 30 | <10 | 72 | <10 | 10 | 64 | 81 | 38 | 121 | <10 | <10 | 19 | <10 | 13 | <10 | <10 | <10 | <10 | <10 | 13 | <10 |

Table. 7.7 Statistical evaluation of major, minor and trace elements of Banganapalle Quartzite

| Oxides/trace elements | Mineralized Banganapalle quartzite | | | non-mineralized Banganapalle quartzite | | |
|---|---|---|---|---|---|---|
| | Avg. | min | max | Avg. | min | max |
| $SiO_2$ | 85.80 | 71.48 | 97.39 | 94.95 | 89.58 | 99.38 |
| $TiO_2$ | 0.11 | 0.02 | 0.37 | 0.06 | <0.01 | 0.12 |
| $Al_2O_3$ | 8.13 | 2.34 | 16.06 | 2.08 | 0.25 | 6.58 |
| $Fe_2O_3$ | 1.33 | 0.36 | 2.92 | 0.56 | <0.01 | 1.44 |
| MgO | 0.36 | <.01 | 1.21 | 0.17 | <0.01 | 0.33 |
| MnO | 0.01 | <.01 | 0.01 | 0.01 | <0.01 | 0.01 |
| CaO | 0.11 | <.01 | 0.24 | 0.19 | <0.01 | 0.74 |
| $Na_2O$ | 0.60 | 0.26 | 1.47 | 0.23 | <0.01 | 0.54 |
| $K_2O$ | 2.75 | 1.03 | 8.34 | 0.91 | 0.03 | 2.3 |
| $P_2O_5$ | 0.03 | <.01 | 0.05 | 0.03 | 0.01 | 0.1 |
| $K_2O/Na_2O$ | 4.93 | 1.54 | 16.35 | 4.78 | 0.4 | 14.3 |
| Cr | 184.71 | 89 | 320 | 76.32 | 43 | 257 |
| Ni | 25.46 | <10 | 61 | 29.82 | <10 | 67 |
| Cu | 11.40 | <10 | 13 | 11.50 | <10 | 12 |
| Zn | 283.69 | <10 | 2824 | 24.67 | <10 | 49 |
| Ga | 11.46 | <10 | 15 | 10.00 | <10 | 10 |
| Rb | 164.97 | 94 | 351 | 53.59 | 23 | 126 |
| Sr | 20.44 | 10 | 63 | 18.09 | <10 | 48 |
| Y | 20.36 | <10 | 41 | - | - | |
| Zr | 114.94 | 45 | 231 | 54.57 | 25 | 100 |
| Nb | 22.44 | <10 | 109 | - | - | - |
| Pb | 115.97 | 42 | 501 | 23.32 | 11 | 63 |
| Ba | 491.88 | 111 | 1238 | 582.68 | 92 | 2934 |
| Ce | 36.26 | <10 | 69 | 19.33 | <10 | 26 |
| Th | 39.00 | <10 | 376 | 19.80 | <10 | 48 |
| U | 570.38 | 63 | 4600 | 46.10 | <10 | 121 |

# CHAPTER 8

# DISCUSSION

The Srisailam and Palnad sub-basins of Cuddapah basin are known for hosting Proterozoic unconformity related uranium mineralization. Uranium mineralization in these sub-basins occurs close to the unconformity between the Closepet equivalent Paleoproterozoic granite (Pandey. et al., 1988) and overlying arenaceous sediments of Meso-Neoproterozoic age. The basement granitoids are profusely traversed by dolerite dykes exhibiting NNW-SSE, NW-SE, E-W and NNE-SSW trends they have possibly played vital role in increasing thermal gradient and release uranyl ions into the solutions with remobilisation along fractures. All these deposits are found in the vicinity of major structures (faults/ fractures) which could have provided the pathways for migration of hydrothermal fluids.

The Sarangapalli-Madinapadu area is located in Northern margin of Palnad sub-basin exposes lower formations of Kurnool group of sediments; Banganapalle Quartzite and Narji limestone non-conformably overlying basement granite intruded by basic dykes. Exposures of basement rocks are not present at the surface of Sarangapalli- Madinapadu area.

Subsurface exploration for uranium mineralization in Sarangapalli-Madinapadu area (T.S. No. 56P/10&14) was taken up by AMD after regional hydro geochemical survey was carried out in the area during F.S. 1997-98, indicated presence of significant hydro uranium anomaly (U = 7 to 45 ppb, n=5) in the vicinity of two major faults. Drilling has resulted in intercepting U-mineralization proximal to unconformity and correlatable over 2400m strike length.

Sarangapalli area was chosen for the present study to understand uranium mineralization in the area and also to extend the analogy to explore other areas of similar geological settings.

Detailed geological mapping to the west of Sarangapalli area is carried out to understand the structural framework of the area and its relationship with mineralization (if any).

The uppermost member of Banganapalle Quartzite (quartz arenite) is exposed as NE-SW trending hillock and Narji limestone is exposed to the East of Banganapalle Quartzite. Both the lithounit are intensely dissected by N-S, NE-SW, NW-SE and E-W fractures (in chronological order). The contact between these two formations is marked by a N25°E trending fault (extending~5 km), which entrained the Banganapalle quartzite above the Narji Limestone as evidenced by sudden termination of lithology, upliftment of Banganapalle Quartzite, linear contact as marked by alignment of drainage, intense fracturing and quartz veination along the fault zone. Shearing is also evidenced along the N25°E trending fault, where principal stresses analysed with the help of tension gashes indicates N-S compression and nearly E-W extension. Slickensides data reveals presence of NW-SE trending oblique slip, normal and dextral sense, cross fault displacing the earlier NE-SW trending major fault which is also supported by drainage, lineament on satellite imagery, development of ferricrete, intense fracturing and quartz veination along the fault zone and throw (up to 50m) recorded in borehole data. Quartz veination is mainly confined with NE-SW and NW-SE trending fractures. Integrated study with airborne geophysical data also supported the field observations.

Based on the detailed field observation, it is concluded that, geologically the area is influenced by deformation which is clearly manifested by presence of faults/fractures which might have provided channel-ways for migration of hydrothermal fluids.

Geophysical studies reveal negative EM responses in late channel (26) image in the vicinity of NNE-SSW trending faults, is due to alterations near the unconformity surface as observed from the borehole data which makes it the potential zone for uranium exploration.

Subsurface studies show that uranium mineralization is occurring in the vicinity of NNE-SSW trending fault and following the trend of fault as indicated by ore body configuration in isograd and isopach map and the later NW-SE trending fault is post mineralization displacing the earlier fault as well as the mineralization.

Detailed borehole studies reveal mineralization is along the unconformity contact and is hosted by basement granite, basic dyke (part of basement) and lower part of Banganapalle quartzite comprising basal conglomerate, pebbly-gritty quartzite and subfeldspathic arenite.

Since major part of mineralization is hosted by subfeldspathic arenite (lower part of Banganapalle Quartzite) and basement granite, their subsurface samples along with surface samples of Banganapalle quartzite were collected for laboratory investigations.

Megascopically, the granite as observed in borehole core exhibit medium to coarse grained, light to dark grey colored equigranular texture with sub-vertical to vertical fractures (brecciation at places) and some of these fractures are filled with quartz, pyrite and chlorite veins. Microscopically this granite corresponds to biotite-granite with hypidiomorphic equigranular texture and consists an assemblage of quartz, albite–oligoclase, orthoclase, microcline and biotite with accessory zircon, allanite, rutile, magnetite, hematite and anatase. Zircon and allanite are altered, and are potential source of uranium mineralisation.

Geochemically, basement granitoid of Sarangapalli area is dominantly peraluminous, moderately differentiated, alkali-calcic to alkali, magnesian series of granite belongs to syn-collisional tectonic settings. The predominance of Rb over Sr (avg. Rb/Sr ratio = 20.75), relatively low CaO and Sr, high $SiO_2$, $K_2O$, $Al_2O_3$ and Rb, high average differentiation index (88.73), normative corundum (CIPW) >1% (avg. 4.89) and syn-collisional tectonic settings indicate their S-type signature. These granites have indicated predominance of LREE over HREE, characterized by strong fractionation of the LREE from the HREE which is attributed to presence of allanite and apatite. Negative Eu anomaly (Eu/Eu* = 0.217 - 0.53), suggesting removal of plagioclase during fractional crystallization.

Uranium metallogeny at Sarangapalli area is attributed to the remobilisation of uranium from the fertile basement granite, which contains higher intrinsic uranium (Av. 25 ppm; n =18) with high U/Th ratio (0.12 - 19.2, Av. = 3.80; n =18) as compared to the average uranium and U/Th ratio of normal granite (U=4 ppm, U/Th = 0.25, Turekian, K.K and Wedephol, K.H. 1961).

Conglomerate is ~5-20 cm thick bed represented by polymictic, matrix supported unit subangular to sub-rounded pebbles of quartz, feldspar and quartzite with size varying from 0.5 to 2 cm.

The subfeldspathic arenite is nearly 4 to 5 meter-thick, medium to coarse grained, light grey colored, hard and compact, massive and contains clasts of quartz and feldspars. Under microscope, quartz with subordinate plagioclase, microcline, perthite, chert, biotite, muscovite, sericite are framework minerals and zircon, tourmaline, sphene are heavy mineral identified with sericite/clay matrix and feldspar content is ~15%. The grains are subrounded to well-rounded in nature. Geochemically, mineralized Banganapalle quartzite is classified as arkose to subarkose while non mineralized quartzites as subarkose to quartz arenite which is also substantiated by petromineralogical studies. Provenance studies indicates, these sediments are derived from felsic, granite to alkali granite, acidic igneous source and deposited in passive margin tectonic settings under semi-arid to semi-humid climatic conditions.

High barium content in studied lithounits is attributed to presence of barite and Ba-Al silicate veins which is substantiated by petromineralogical studies.

Both the lithounit are highly fractured specially near the mineralized zone and some of these fractures are filled with pyrite, quartz and chlorite veins indicating brittle deformation in the area which is also substantiated by field studies.

Detailed Field and petromineralogical studies show ample evidences of hydrothermal activity associated with uranium mineralisation as manifested by development of fracture filling veins (mm to m scale). These veins are mainly comprised of quartz, quartz-pyrite, chlorite and barite responsible for different phases of alteration.

Sericitization and chloritization are dominant alteration feature in the mineralized zone/ unconformity surface transgressing the lithological boundaries appears to have caused by invasion of hydrothermal solutions. Due to appreciable amount of sericitization the borehole core shows dull yellow coloration.

Mineralization is mainly observed along the weak planes (fracture). Uraninite and coffinite are the main primary radioactive phases identified closely associated with chlorite (both vein chlorite & alteration product of biotite) and pyrite. Coffinite is formed as alteration product of uraninite suggesting addition of silica in the system.

Close association of galena with coffinite suggesting Pb released during coffinitization is precipitated as galena.

Two phases of chlorite have been identified in both the lithounits, one as alteration product of biotite another along fissures appears like vein chlorite and both are associated with mineralization. Mineral chemistry shows it is Fe rich chlorite, chemically resembles the name Chamosite. The average temperature of formation of chlorite is $245^0$ C indicating epithermal stage of hydrothermal alteration. Close association of chlorite and pyrite with mineralization suggest that redox reaction involving Fe in chlorite and pyrite was responsible for uranium deposition in the area. Chloritization might also have facilitated mineralization through destabilizing the uranium in solution by lowering the pH.

Paragenetic sequence of hydrothermally derived minerals have been established. It shows initially fracturing and brecciation of host rock taken place then in first phase sericite and baryte with minor chlorite have formed prior to uranium mineralization. In ore stage uraninite formed and chloritization is continued from pre-ore stage followed by break down of baryte to Ba-Al silicate coupled with coffinitization of uraninite have taken place. In post ore stage formation of galena and second phase of sericitization have taken place.  Pyrite have been observed in all the stage.

# CHAPTER-9

# CONCLUSION

- Geologically the area is affected by two stage of faulting, first stage faulting (NE-SW) brought up Banganapalle quartzite above the Narji limestone which have provided the channel ways for mineralizing solution and second stage faulting (NW-SE) displaces the earlier fault and ore body. Presence of these faults also substantiated by geophysical studies.
- The mineralization occurs in the vicinity of NE-SW fault and following the trend of fault.
- Mineralization is along the unconformity contact and hosted by basement granite, basic dyke (intruded into basement prior to sedimentation) and lower part of Banganapalle quartzite (represented by conglomerate, pebbly-gritty quartzite and subfeldspathic arenite). Unconformity has provided physico-chemical gradient for mineralizing solution.
- Geochemically, mineralized Banganapalle quartzite is mostly classified as arkose to subarkose while non mineralized quartzites as subarkose to quartz arenite. Provenance studies indicates, these sediments are derived from granite to alkali granite source and deposited in passive margin tectonic settings under semi-arid to semi-humid climatic conditions.
- The basement granite showing signature of S-type granite, is fertile in nature and had acted as source for uranium mineralization.
- Sericitization and chloritization are dominant alteration features present mainly near the unconformity surface and transgressing the lithological boundary signifies hydrothermal activity. Two stage of sericitization identified one is pre-ore stage and second is post- ore stage.

- Uraninite and coffinite are the dominant uranium phases present and are closely associated with chlorite and pyrite.
- Chloritization took place at $245^0$C temperature. Chlorite along with some pyrite aided uranium precipitation by reducing it from solution.
- On the basis of textural relationship mineral paragenetic sequence has been established. Mineralization took place during syn- to post- chloritization.

# REFRENCES

Anand, M., Gibson, S.A., Subbarao, K.V., Kelley, S.P. and Dickin, A.P., 2003. Early Proterozoic melt generation processes beneath the intra-cratonic Cuddapah Basin, southern India. Journal of Petrology, 44(12), pp.2139-2171.

Babu, E.V.S.S.K., Griffin, W.L., Mukherjee, A., O'Reilly, S.Y. and Belousova, E.A., 2008, October. Combined U-Pb and Lu-Hf analysis of megacrystic zircons from the Kalyandurg-4 kimberlite pipe, S. India: Implications for the emplacement age and Hf isotopic composition of the cratonic mantle. In International Kimberlite Conference: Extended Abstracts, vol. 9.

Banerjee, D.C., 2005. Uranium exploration in the Proterozoic basins in India – Present status and future strategy, India. IAEA–TECDOC–1425, pp. 81–94.

Bhatia, M.R., 1983. Plate tectonics and geochemical composition of sandstones. The Journal of Geology, 91(6), pp.611-627.

Bisht, B.S., Rajasekaran, P. and Sinha, R.M., 2001. Fluid inclusion characteristics of unconformity-related uranium mineralisation, Lambapur-Peddagattu area, Andhra Pradesh. Journal of the Geological Society of India, vol.58(1), pp.45-51.

Boynton, W.V., 1984. Cosmochemistry of the rare earth elements: meteorite studies. In Developments in geochemistry, Vol. 2, pp. 63-114.

Caritat, P.D., Hutcheon, I and Walshe, J.L., 1993. Chlorite Geothermometry: A review. Clay and clay minerals, vol. 41, pp. 219-239.

Cathelineau, M., 1988. Cation site occupancy in chlorite sand illites as function of temperature. Clay Minerals, vol.23, pp.471–485.

Chakraborti, S. and Saha, D., 2009. Tectonic stresses and thin-skinned tectonics in a Proterozoic fold-and-thrust belt read from calcite mylonites in the Cuddapah basin, south India. Indian Journal of Geology, vol.78, pp.37-54.

Chalapathi Rao, N. V.,Miller, J. A., Gibson, S. A., Pyle, D. M. and Madhavan, V. 1999. Precise 40Ar/39Ar dating of Kotakonda kimberlite and Chelima lamproite, India: implication to the timing of mafic dyke swarm activity in the Eastern Dhawar craton. Journal of the Geological Society of India, vol. 53, pp. 425–32.

Chalapathi Rao, N.V., Wu, F.-Y., Mitchell, R.H., Li, Q.-L. and Lehmann, B. 2013. Mesoproterozoic U–Pb ages, trace element and Sr–Nd isotopic composition of perovskite from kimberlites of the Eastern Dharwar craton, southern India: distinct mantle sources and a widespread 1.1 Ga tectonomagmatic event. Chemical Geology, vol. 353, pp. 48–64.

Chappell B.W., White A.J.R. and Wyborn D. 1987. The importance of residual source material (restite) in granite petrogenesis [J]. Journal of Petrology, vol. 28, pp. 1111–1138.

Chappell, B.W. and White, A.J.R., 1992. I-and S-type granites in the Lachlan Fold Belt. Transactions of the Royal Society of Edinburgh. Earth Sciences, vol. 83(1-2), pp.1-26.

Chetty, T.R.K. and Murthy, D.S.N., 1994. Collision tectonics in the late Precambrian Eastern Ghats mobile belt: mesoscopic to satellite scale observations. Terra Nova, vol. 6, pp. 72-81.

Clarke, D. B., 1981. The mineralogy of peraluminous granites; a review. The Canadian Mineralogist, 19(1), pp.3-17.

Clarke, F.W., 1924. The data of geochemistry (5th Ed.). USGS Bulletin, No. 770, pp. 841.

Coulson, A.L., 1933. KALVA (Calwa) "Wall" In the Kurnool district of Madras Presidency an example of monoclonal folding accompanied by faulting along an old line of weakness. Records of the Geological Society of India, vol.66 (4), pp. 438-48.

Crook, K.A., 1974. Lithogenesis and geotectonics: the significance of compositional variation in flysch arenites (graywackes).

Cuney, M. and Friedrich, M., 1987. Physicochemical and crystal-chemical controls on accessory mineral paragenesis in granitoids: implications for uranium metallogenesis. Bulletin de mineralogie, vol. 110(2), pp. 235-247.

Cuney, M., 2009. The extreme diversity of uranium deposits. Mineralium Deposita, vol. 44, pp. 3-9.

Dahlkamp, F. J., 1993. Uranium ore deposits. Springer, Berlin, pp. 460 & 51–56.

Dickinson, W.R. and Suczek, C.A., 1979. Plate tectonics and sandstone compositions. Aapg Bulletin, vol. 63(12), pp. 2164-2182.

Dutt, N.V.B.S., 1962. Geology of the Kurnool System of rocks in Cuddapah and the southern part of Kurnool district. Records of the Geological Survey of India, vol.87(3), pp.549-604.

Dwivedy, K.K., 1995. Economic aspects of the Cuddapah Basin with special reference to uranium – an overview. Proc. Sem. On Cuddapah Basin, Geological Society of India, pp. 116–138.

El Bouseily, A. M., and A. A. El Sokkary., 1975. "The relation between Rb, Ba and Sr in granitic rocks. Chemical Geology 16, vol. 3, pp.207-219.

El-Sharkawy, M.F., 2000. Talc mineralization of ultramafic affinity in the Eastern Desert of Egypt. Mineralium. Deposita, vol. 35, pp. 346–363.

Ewing, R.C., Meldrum, A., Wang, L., Weber, W.J. and Corrales, L.R., 2003. Radiation effects in zircon. Reviews in Mineralogy and geochemistry, vol. 53(1), pp.387-425.

Floyd, P.A., Winchester, J.A. and Park, R.G., 1989. Geochemistry and tectonic setting of Lewisian clastic metasediments from the Early Proterozoic Loch Maree Group of Gairloch, NW Scotland. Precambrian Research, vol. 45(1-3), pp.203-214.

Foster, M.D., 1962. Interpretation and a classification of the chlorite. US Geological Survey Professional Paper, vol. 414, pp.1-33.

Fritsche, R. and Dahlkamp, F.J., 2001. Contribution to characteristics of uranium oxides (No. IAEA-TECDOC--1258).

Frost, B. R., Barnes, C. G., Collins, W. J., Arculus, R. J., Ellis, D. J., and Frost, C. D. (2001). A geochemical classification for granitic rocks. Journal of petrology, vol. 42(11), pp. 2033-2048.

Guo, X., Szenknect, S., Mesbah, A., Labs, S., Clavier, N., Poinssot, C., Ushakov, S.V., Curtius, H., Bosbach, D., Ewing, R.C., Burns, P.C., Dacheux, N., and Navrotsky, A., 2015. Thermodynamics of formation of coffinite, USiO4. Proceedings of the National Academy of Sciences, vol.112, pp.21.

Harker, A., 1909. The natural history of igneous rocks. Macmillan, New york, pp. 384.

Hayashi, K.I., Fujisawa, H., Holland, H.D. and Ohmoto, H., 1997. Geochemistry of ~ 1.9 Ga sedimentary rocks from northeastern Labrador, Canada. Geochimica et Cosmochimica Acta, vol. 61(19), pp.4115-4137.

Herron, M. M., 1988. Geochemical classification of terrigenous sands and shales from core or log data. Journal of Sedimentary Research, vol. 58(5), pp. 820-829.

Hey, M.H., 1954. A new review of the chlorites. Mineral. Mag. vol. 30, pp. 277–292.

Jakobsen, U.H., 1990. A hydrated barium silicate in unmetamorphosed sedimentary rocks of central North Greenland. Mineralogical Magazine, vol. 54, pp. 81-89.

Janeczek, J. and Ewing, R.C., 1992. Dissolution and alteration of uraninite under reducing conditions. Journal of Nuclear Materials, 190, pp.157-173.

Jeyagopal, A.V., Kumar, P. and Sinha, R.M., 1996. Uranium mineralization in the Palnad Sub-basin, Cuddapah Basin, Andhra Pradesh, India. Current Science, vol. 71(2), pp.957–959.

Korzhinskiy, D.S., 1980. “Equations of metasomatic reactions”. International Geology Review, vol. 22(11), pp. 1257-1258.

Krogh, T.E. and Davis, G.L., 1975. Alteration in zircons and differential dissolution of altered and metamict zircon. Carnegie Inst. Wash. Year B, vol. 74, pp. 619–623.

Kumar, A., Gopalan, K., Rao, K. R. P. and Nayak, S.S. 2001. Rb-Sr age of kimberlites and lamproites from Eastern Dharwar Craton, South India. Journal of the Geological Society of India vol. 58, pp. 135–41.

Kumar, A., Heaman, L.M. and Manikeyamba, C. 2007. Mesoproterozoic kimberlites in south India: a possible link to ∼1.1 Ga global magmatism. Precambrian Research vol. 154, pp. 192–204.

Kumar, A., Padma Kumari, V. M., Dayal, A.M.,Murthy, D. S. N. and Gopalan, K. 1993. Rb-Sr ages for Proterozoic kimberlites of India: evidence for contemporaneous emplacement. Precambrian Research, vol. 62, pp. 227–37.

Macnae, J., 2016. Fitting superparamagnetic and distributed Cole-Cole parameters to airborne electromagnetic data: A case history from Quebec. Geophysics., vol. 81, pp. B211-B220.

Maniar, P.D. and Piccoli, P.M., 1989. Tectonic discrimination of granitoids. Geological society of America bulletin, vol. 101(5), pp.635-643.

Matin, A. and Guha, J. 1996. Structural geometry of the rocks of the southern part of the Nallamalai Fold Belt, Cuddapah Basin, Andhra Pradesh. Journal of the Geological Society of India, vol.47, pp.535–545.

Matsubara, S., 1985. The mineralogical implication of barium and strontium silicates. Bulletin of the National Science Museum, Series C, vol. 11(2), pp.37-95.

Mclennan, S.M., 1989. Rare earth elements in sedimentary rocks: influence of provenance and sedimentary processes. Geochemistry and mineralogy of rare earth elements, reviews in mineralogy, vol. 21, pp.169-200.

Meijerink, A.M.J., Rao, D.P. and Rupke, J., 1984. Stratigraphic and structural development of the Precambrian Cuddapah Basin, SE India. Precambrian Research, vol.26(1), pp.57-104.

Middlemost, E. A., 1994. Naming materials in the magma/igneous rock system. Earth-Science Reviews, vol.37(3-4), pp. 215-224.

Min, M., Fang, C. and Fayek, M., 2005. Petrography and genetic history of coffinite and uraninite from the Liueryiqi granite-hosted uranium deposit, SE China. Ore Geology Reviews, vol. 26(3-4), pp. 187–197.

Moro, M. C., Cembranos, M. L., and Fernandez, A., 2001. Celsian, (Ba, K)-feldspar and cymrite from sedex barite deposits of Zamora, Spain. The Canadian Mineralogist, vol. 39(4), pp.1039-1051.

Mukherjee, M.K., 2001. Structural pattern and kinematic framework of deformation in the southern Nallamalai fold–fault belt, Cuddapah district, Andhra Pradesh, Southern India. Journal of Asian Earth Sciences, vol.19(1-2), pp.1-15.

Nagaraja Rao, B.K., Rajurkar, S.T., Ramalingaswamy, G. and Ravindra Babu, B., 1987. Stratigraphy, structure and evolution of the Cuddapah basin. Geological Society of India, vol.6, pp.33-86.

Narayanaswami, S., 1966. Tectonics of the Cuddapah basin. Geological Society of India, vol.7, pp.33-50.

Neiva, A.M.R., 1992. Geochemistry and evolution of Jales granitic system, Northern Portugal [J]. Chem. Erde., vol. 52, pp. 225–241.

OECD / NEA Red Book & IAEA, 2000. Uranium 1999: Resources, Production and Demand. OECD Nuclear Energy Agency and International Atomic Energy Agency, Paris.

Pandey, B.K., Prasad, R.N., Sastry, D.V.L.N., Kumar, B.R.M, Suryanarayana Rao, S., Gupta, J.N., 1988. Rb-Sr whole rock ages for the granites from parts of Andhra Pradesh and Karnataka, In: Fourth national symposium on mass spectrometry, Indian Institute of Science, Bangalore, India. EPS- 3/1.

Passchier, C. W. and Trouw, R. A., 2005. Microtectonics. Springer Science and Business Media, vol.1 pp. 306.

Patranabis-Deb, S., Saha, D. and Tripathy, V., 2012. Basin stratigraphy, sea-level fluctuations and their global tectonic connections— evidence from the Proterozoic Cuddapah Basin. Geological Journal, Published online in Wiley Online Library (wileyonlinelibrary.com). DOI: 10.1002/gj.1347.

Pearce, J. A., Harris, N. B., and Tindle, A. G., 1984. Trace element discrimination diagrams for the tectonic interpretation of granitic rocks. Journal of petrology, 25(4), pp. 956-983.

Pirajno, F. 1992. “Hydrothermal mineral deposits: principles and fundamental concepts for the exploration geologist”. Springer Science & Business Media. pp.460.

Plissart, G., Féménias, O., Mãruntiu, M., Diot, H., Demaiffe, D., 2009. Mineralogy and geothermometry of gabbro-derived listvenites in the Tisovita- Iutiophiolite southwestern Romania. Can. Mineral. Vol. 47, pp. 81–105.

Singh, R.V., Gupta, S., Verma, M.B., Deshpande, M.S.M., Jeyagopal, A.V., Umamaheswai, K. and Maithani, P.B., 2013. Peraluminous granites: Potential source for uranium mineralisation in Koppunuru area, Guntur district, Andhra Pradesh. Journal of Applied Geochemistry, vol.15(2), pp.124.

Ramam, P.K. and Murty, V.N., 1997. Geology of Andhra Pradesh: Geological Society of India. Text Book Series, (4), pp.1-245.

Ramesh Babu, P.V., Banerjee, R. and Achar, K.K., 2012. Srisailam and Palnad sub-basins: potential geological domains for unconformity-related uranium mineralisation in India. Exploration and Research for Atomic Minerals, vol. 22, pp. 21-42.

Ramesh Babu, V., Patra, I., Tripathi, S., Muthyala, S. and Chaturvedi, A. K., 2017. Case History: Inductive induced polarization effect in heliborne time-domain electromagnetic data for uranium exploration, northern part of Cuddapah Basin, India. Geophysics., vol. 82, pp. B109-B120.

Ravikant, V. 2010. Palaeoproterozoic (~1.9Ga) extension and breakup along the eastern margin of the eastern Dharwar craton, SE India: new Sm–Nd isochron age constraints from anorogenic mafic magmatism in the Neoarchaean Nellore greenstone belt. Journal of Asian Earth Sciences, vol. 37, pp. 67 –81.

Richards, P.W., Jhanwar, M.L., Rajurkar, S.T., and Phadterre, P.N., 1968. Stratigraphy of the lower part of the Kurnool Group in west central Cuddapah Basin, A.P. Geological survey of India open file report no.2.

Rose, A.W. and Burt, D.M., 1979. "Hydrothermal alteration", In: H.L. Barnes {Editor), Geochemistry of Hydrothermal Ore Deposits, 2nd edition. John Wiley and Sons, New York, NY, pp. 173-235.

Roser, B.P. and Korsch, R.J., 1986. Determination of tectonic setting of sandstone-mudstone suites using SiO2 content and K2O/Na2O ratio. The Journal of Geology, vol. 94(5), pp.635-650.

Saha, D. 1994. Fold–Fault structures of the Nallamalai range, Diguvametta–Nandi Ka Nama Pass, Prakasam district, Andhra Pradesh, South India. Indian Journal of Geology, vol.66, pp. 203–213.

Saha, D. and Tripathy, V., 2012. Palaeoproterozoic sedimentation in the Cuddapah Basin, south India and regional tectonics: a review. Geological Society, London, Special Publications, vol.365(1), pp.161-184.

Saha, D., 2002. Multi-stage deformation in the Nallamalai Fold Belt, Cuddapah basin, South India-Implications for Mesoproterozoic tectonism along southeastern margin of India. Gondwana Research, vol.5(3), pp.701-719.

Saha, D., 2004. Structural asymmetry and Plate tectonic set-up for a Proterozoic Fold and Thrust Belt: Nallamalai fold belt and Adjoining Terrane, South India. Geological. Survey of India, Special Publications, vol.84, pp.101-119.

Saha, D., Chakraborti, S. and Tripathy, V., 2010. Intracontinental thrusts and inclined transpression along eastern margin of the East Dharwar Craton, India. Journal of the Geological Society of India, vol.75(1), pp.323-337.

Schieber, J., 1992. A combined petrographical–geochemical provenance study of the Newland Formation, Mid-Proterozoic of Montana. Geological Magazine, vol.129(2), pp.223-237.

Shand, S. J. (1943). Eruptive rocks: their genesis, composition, classification, and their relation to ore deposits with a chapter on meteorites. John Wiley and Sons. New York, pp. 444.

Siever, R., 1979. Plate-tectonic controls on diagenesis. The Journal of Geology, vol.87(2), pp.127-155.

Singh, R.V., Banerjee Rahul, and Verma, M.B., 2017. Geochemistry of basement granitoids, Chenchu Colony Area, Guntur District, Andhra Pradesh. Journal of Applied Geochemistry, vol. 19(1), pp. 96-110.

Sinha, R.M., Parthasarathy, T.N. and Dwivedy, K.K., 1996. On the possibility of identifying low cost, medium grade uranium deposits close to the Proterozoic unconformity in the Cuddapah basin, Andhra Pradesh, India. IAEA–TECDOC–868, pp. 35–55.

Suttner, L.J. and Dutta, P.K., 1986. Alluvial sandstone composition and paleoclimate; I, Framework mineralogy. Journal of Sedimentary Research, vol.56(3), pp.329-345.

Syamala Rao, A, Sood, N.K., Basu, P.C., Rajendran, N. and Venkata Dasu, S.P., 1987. Phosphorite in the Cuddapah Basin, Andhra Pradesh. In Purana Basin of Penninsular India, Middle to Late Proterozoic. Mem. Geol. Soc. Inida, vol..6, pp.511–518.

Thomas, P.K., Thomas, T., Thomas, J., Pandian, M.S., Banerjee, R., Ramesh Babu, P.V., Gupta, S. and Vimal, R., 2014. Role of hydrothermal activity in uranium mineralisation in Palnad Sub-basin, Cuddapah Basin, India. Journal of Asian Earth Sciences, vol. 91, pp. 280–288.

Turekian, K.K. and Wedepohl, K.H., 1961. Distribution of elements in some major units of the earth's crust. Bull. Geological Society of America., vol. 72, pp. 175-192.

Umamaheswar, K., Achar, K. K. and Maithani, P.B., 2009. Proterozoic Unconformity related Uranium Mineralisation in the Srisailam and Palnad Sub- Basins of Cuddapah Basin, Andhra Pradesh, India. IAEA-CN-175/28, p. 93.

Valloni, R. and Maynard, J.B., 1981. Detrital modes of recent deep-sea sands and their relation to tectonic setting: a first approximation. Sedimentology, vol.28(1), pp.75-83.

Venkatakrishnan, R. & Dotiwala, F. E., 1987. The Cuddapah salient: a tectonic model for the Cuddapah basin, India, based on Landsat image interpretation. Tectonophysics, vol.136, pp.237–253.

Vijaya Kumar, K. & Leelanandam, C. 2008. Evolution of the Eastern Ghats belt, India: a plate tectonic perspective. Journal of the Geological Society of India, vol.72, pp.720–749.

Vimal Rajiv, Banerjee Rahul., Gupta Shekhar., Krishna Veena, Achar K.K., Rameshbabu P.V., Parihar P.S., and Maithani P.B., 2012. Geochemistry and Sr and Pb Isotope systematics of basement granitoids from north and west of Palnad sub-basin, Guntur and Nalgonda District, Andhra Pradesh. Journal of Applied Geochemistry, vol. 14(3), pp. 295-315.

Wang, Y., Xu, H., 1999. Coffinitization of Uraninite: SEM/AEM Investigation and Geochemical Modeling. ICEM '99; Nagoya (Japan), pp. 1-7.

Wu, D., Pan, J., Xia, F., Huang, G. and Lai, J., 2019. The Mineral Chemistry of Chlorites and Its Relationship with Uranium Mineralization from Huangsha Uranium Mining Area in the Middle Nanling Range. SE China. Minerals, vol. 9(3), pp. 199.

Xie, X., Byerly, G.R. and Ferrell Jr, R.E., 1997. IIb trioctahedral chlorite from the Barberton greenstone belt: crystal structure and rock composition constraints with implications to geothermometry. Contributions to Mineralogy and Petrology, 126(3), pp.275-291.

Yavuz, F., Kumral, M., Karakaya, N., Karakaya, M. Ç. and Yıldırım, D. K., 2015. A Windows program for chlorite calculation and classification. Computers & Geosciences, vol. 81, pp. 101–113.

Yerino, L.N. and Maynard, J.B., 1984. Petrography of modern marine sands from the Peru-Chile Trench and adjacent areas. Sedimentology, vol.31(1), pp.83-89.

Yuan, F., Jiang, S.-Y., Liu, J., Zhang, S., Xiao, Z., Liu, G. and Hu, X., 2019. Geochronology and Geochemistry of Uraninite and Coffinite: Insights into Ore-Forming Process in the Pegmatite- Hosted Uraniferous Province, North Qinling, Central China. Minerals, vol. 9, pp. 552.

Zane, A. and Weiss, Z., 1998. A procedure for classifying rock-forming chlorites based on microprobe data. Rendiconti Lincei, vol.9(1), pp.51-56.

Zang, W., Fyfe, W.S., 1995. Chloritization of the hydrothermally altered bedrock at the Igarapé Bahia gold deposit, Carajás, Brazil. Mineralium Deposita, vol.30, pp.30–38.

Zou, S., Zou, F., Ning, J., Deng, T., Yu, D., Ye, T. and Wang, Z., 2018. A stand-alone Co mineral deposit in northeastern Hunan Province, South China: Its timing, origin of ore fluids and metal Co, and geodynamic setting. Ore Geology Reviews, vol. 92, pp. 42–60.